

# A Survey Of Photonuclear Reactions on $^{12}\text{C}$

Thesis

submitted by

Daniel Watts

for the degree of

Doctor of Philosophy

Department of Physics and Astronomy,

University of Glasgow,

1997.

©D.Watts, 1997.

ProQuest Number: 13818614

All rights reserved

INFORMATION TO ALL USERS

The quality of this reproduction is dependent upon the quality of the copy submitted.

In the unlikely event that the author did not send a complete manuscript and there are missing pages, these will be noted. Also, if material had to be removed, a note will indicate the deletion.



ProQuest 13818614

Published by ProQuest LLC (2018). Copyright of the Dissertation is held by the Author.

All rights reserved.

This work is protected against unauthorized copying under Title 17, United States Code  
Microform Edition © ProQuest LLC.

ProQuest LLC.  
789 East Eisenhower Parkway  
P.O. Box 1346  
Ann Arbor, MI 48106 – 1346

GLASGOW UNIVERSITY  
LIBRARY  
11172 (copy 1)



## Abstract

This thesis describes an experimental study of the  $C^{12}(\gamma, 2N)$  and  $C^{12}(\gamma, 3N)$  reactions using tagged photons of energies 150-700 MeV.

The photon beam was produced using the MAMI-B electron accelerator at the Institut für Kernphysik at Mainz. Bremsstrahlung photons were produced by the electron beam impinging on a thin nickel foil radiator. The photon energies were determined with a resolution of  $\sim 2$  MeV by analysis of the residual electrons in the Glasgow tagging spectrometer. Reaction products were detected in two detector systems PiP, TOF. The PiP detector is a large solid angle ( $\sim 1$  sr) plastic scintillator hodoscope used to detect protons. The TOF detector system comprised a versatile array of plastic scintillators which determined both proton and neutron energies from time of flight information. The detector system had a combined missing energy resolution of  $\sim 8$  MeV.

The particle detectors were positioned to cover kinematics both in and away from the back-to-back kinematics of previous measurements. The more unusual detector geometry gave more sensitivity to multiparticle/FSI processes and also allowed the study of direct 2 nucleon emission in regions of high initial pair momenta.

The results were compared with a model developed by the Valencia group, which accounts for all the main photon absorption processes and therefore gives predictions of the cross section for all missing energy  $E_m$ . The predictions of the Valencia model (VM) give reasonable agreement with the shape of the measured  $E_m$  distributions for both  $^{12}C(\gamma, pn)$  and  $^{12}C(\gamma, pp)$  reactions up to 700 MeV, even in the more unusual kinematics. The magnitude of the cross section for the  $^{12}C(\gamma, pp)$  was however overestimated by a photon energy and angular dependant factor of  $\sim 3.5$ . A smaller overestimation of the strength of the cross section

was also observed in the  $^{12}\text{C}(\gamma, pn)$  reaction for photon energies around the  $\Delta$  resonance.

The comparison of the low missing energy data with a model of direct 2N emission from a spectating nucleus (2N model) showed the dominance of the 2N process in the  $^{12}\text{C}(\gamma, pn)$  reaction for  $E_m \leq 70$  MeV and photon energies up to 600 MeV, even with the detectors positioned to be sensitive to more complex mechanisms. The  $^{12}\text{C}(\gamma, pp)$  reaction was shown to be reasonably well described by direct emission of  $(1p)^2$  proton pairs for  $E_m \leq 40$  MeV and  $E_\gamma \leq 500$  MeV, although the agreement with the 2N model was not as good as observed for the  $(\gamma, pn)$  data. A large contribution of FSI/multiparticle events was observed for this reaction in the  $E_m=40-70$  MeV region although some evidence for the existence of photon absorption on  $(1s)(1p)$  proton pairs was found.

The  $(\gamma, 3N)$  measurements allowed a more kinematically complete study of multiparticle/FSI processes and gave valuable information on the mechanisms involved. The first measurement of the  $^{12}\text{C}(\gamma, ppn)$  and  $^{12}\text{C}(\gamma, pnn)$  final states showed cross sections of similar magnitude and shape. The  $^{12}\text{C}(\gamma, ppp)$  cross section was found to be  $\leq \sim 8\%$  of the ppn or pnn.

The Valencia model predicted that the dominant mechanism for all the 3N final states was the reabsorption of photoproduced pions by nucleon pairs, with lesser contributions from 2N/3N+FSI processes. Although giving predictions in good agreement with the data for the ppn and pnn final states, the VM overestimated the ppp final state by an energy dependent factor of  $\sim 5$  which was attributed to the calculation of either the magnitude or angular distribution of the charge exchange FSI processes.

## Declaration

The data presented in this thesis were obtained by the Experimental Nuclear Physics group at the University of Glasgow in collaboration with colleagues from the Nuclear Physics groups at the Universities of Edinburgh, Tübingen and Mainz. The experiment was performed at the Institut für Kernphysik at the University of Mainz. I participated fully in the execution of the experiment. The analysis and interpretation of the experimental data is entirely my own work. This thesis was composed by myself.

## Acknowledgements

I would like to thank all the members of the Nuclear Structure group at Glasgow University for their help and encouragement throughout my Phd. In particular Dr. Douglas MacGregor, Dr. Cameron McGeorge and Dr. Peter Harty who were in the forward line for the painful detector calibration years and therefore had to put up with the greatest volume of questions.

A big thank you must also go to Prof. Bob Owens for invaluable physics discussions in which all my questions were answered with worrying ease. My cap is also doffed to Dr. John Annand for his development of the data acquisition software and to Dr Ian Anthony and Andy Sibbald who kept the cogs and wheels well oiled on the computers throughout. I also wish to thank my fellow students. In particular many interesting discussions with Stephen McAllister about nothing in particular were of a great help.

I would also like to show appreciation to the staff and students of Tübingen and Edinburgh universities who played a big part in the development and running of the experiment. The Tübingen collaborators also gave a big input into the data analysis codes and techniques. Other deserving people are the staff and students of the Institut für Kernphysik at Mainz for providing a smoothly operating electron beam throughout the experiment. My thanks must also go to the Engineering and Physical Sciences Research Council for financial support and travel expenses during my time as a student.

Finally I would like to thank my family for their constant encouragement and would like to dedicate this thesis to my brother, Tony.

# Contents

<b>1</b>	<b>Introduction</b>	<b>1</b>
1.1	Introduction . . . . .	2
1.1.1	Outline . . . . .	2
1.1.2	Photoabsorption . . . . .	3
1.2	Review Of Previous Experiments . . . . .	8
1.2.1	$(\gamma, 2N)$ measurements . . . . .	8
1.2.2	Review of experimental studies of multiparticle mechanisms	10
1.3	Review of Theoretical Progress . . . . .	12
1.3.1	$(\gamma, 2N)$ reactions . . . . .	12
1.3.2	The 2N photon absorption model . . . . .	17
1.4	Review of multiparticle theories . . . . .	18
1.4.1	The Valencia model . . . . .	19
1.5	Summary and Aims of Present Experiment . . . . .	21
<b>2</b>	<b>Experimental Apparatus</b>	<b>23</b>
2.1	Experimental Apparatus . . . . .	24
2.2	The Mainz Electron Microtron . . . . .	24
2.3	Photon Production . . . . .	26
2.3.1	The Glasgow Tagging Spectrometer . . . . .	27
2.3.2	Collimation and Tagging Efficiency . . . . .	29

2.4	Targets . . . . .	30
2.4.1	The $\Delta E$ Detector Rings . . . . .	31
2.4.2	The PiP Detector . . . . .	32
2.4.3	TOF detectors . . . . .	33
2.4.4	Experimental Setup . . . . .	35
2.5	Data Acquisition . . . . .	35
2.5.1	Information from events . . . . .	35
2.5.2	Trigger Logic . . . . .	37
2.5.3	First Level . . . . .	38
2.5.4	Second Level . . . . .	40
2.5.5	Data Acquisition . . . . .	42
<b>3</b>	<b>Detector Calibrations</b>	<b>44</b>
3.1	General Concepts . . . . .	45
3.1.1	QDC Properties . . . . .	45
3.1.2	TDC properties . . . . .	46
3.1.3	Walk correcting the TDCs . . . . .	47
3.2	General Detector Properties . . . . .	48
3.2.1	Light Output . . . . .	48
3.2.2	Position . . . . .	49
3.2.3	Scintillator Response And Electron Equivalent Energy Units	49
3.2.4	Energy Loss Corrections . . . . .	50
3.3	Start Detector . . . . .	51
3.4	Tagger . . . . .	52
3.5	The PiP Detector . . . . .	53
3.5.1	Walk Correction . . . . .	53
3.5.2	Position Calibration . . . . .	53

3.5.3	Gain Matching and Droop . . . . .	54
3.5.4	Energy Calibration . . . . .	56
3.6	The TOF Detectors . . . . .	57
3.6.1	Walk Correction . . . . .	57
3.6.2	Position Calibration . . . . .	57
3.7	Energy calibration . . . . .	58
3.7.1	Gain Matching . . . . .	60
3.7.2	Replacement QDC Values . . . . .	60
3.7.3	TOF Pulse Height Thresholds . . . . .	62
3.8	Detector Performance . . . . .	64
3.8.1	Separating Deuterium Events . . . . .	64
3.8.2	Measured Detector Resolution . . . . .	65
3.8.3	Intrinsic Detector Resolution . . . . .	66
<b>4</b>	<b>Data Analysis</b>	<b>69</b>
4.1	Proton Selection in PiP . . . . .	70
4.2	Relevant $\Delta E_{TOF}$ Selection . . . . .	72
4.3	The Effect of Double TOF stands . . . . .	73
4.3.1	Corrections for dead TOF bars . . . . .	74
4.4	Neutron selection in TOF . . . . .	74
4.4.1	Proton selection in TOF . . . . .	76
4.4.2	Proton Energy loss corrections . . . . .	77
4.5	The subtraction of random events . . . . .	77
4.5.1	Tagger randoms . . . . .	77
4.5.2	TOF randoms subtraction for uncharged events . . . . .	79
4.5.3	TOF randoms subtraction for charged events . . . . .	80
4.6	Detector efficiencies . . . . .	80

4.6.1	Tagging Efficiency . . . . .	80
4.6.2	Proton efficiency in PiP . . . . .	81
4.6.3	Neutron efficiency . . . . .	81
4.7	Multiple Hits . . . . .	84
4.8	Background Subtractions . . . . .	86
4.9	Derivation Of The Cross Section . . . . .	86
4.10	Statistical Uncertainties . . . . .	87
4.11	Systematic Uncertainties . . . . .	87
<b>5</b>	<b>Results and Discussion</b>	<b>91</b>
5.1	The $(\gamma, 2N)$ Reactions . . . . .	92
5.2	Comparisons with the Valencia model . . . . .	94
5.2.1	The $(\gamma, pn)$ reaction . . . . .	95
5.2.2	The $(\gamma, pp)$ reaction . . . . .	99
5.3	Comparisons of the low $E_m$ regions with the 2N model . . . . .	103
5.3.1	The $(\gamma, pn)$ reaction . . . . .	104
5.3.2	The $(\gamma, pp)$ reaction . . . . .	116
5.4	The $(\gamma, 3N)$ reactions . . . . .	125
5.5	Comparisons with the Valencia model . . . . .	126
5.5.1	The $(\gamma, ppn)$ reaction . . . . .	126
5.5.2	The $(\gamma, ppp)$ reaction . . . . .	130
5.5.3	The $(\gamma, pnn)$ reaction . . . . .	135
<b>6</b>	<b>Summary, Conclusions and Outlook</b>	<b>139</b>
6.1	Summary and Conclusions . . . . .	140
6.2	Outlook . . . . .	143
<b>A</b>	<b>Corrections For Dead Tof Bars</b>	<b>146</b>

# List of Figures

1.1	Total photon absorption cross section per nucleon . . . . .	4
1.2	Absorption terms considered for the $(\gamma, pn)$ emission . . . . .	15
1.3	Comparison of unfactorised and factorised cross section predictions for the $^{16}\text{O}(\gamma, pn)$ reaction . . . . .	16
1.4	A Typical Photon Self Energy Diagram . . . . .	20
2.1	Schematic diagram of a racetrack microtron . . . . .	25
2.2	The Mainz electron microtron (MAMI-B) . . . . .	26
2.3	Schematic of the tagging spectrometer . . . . .	28
2.4	A schematic of the $\Delta E$ Detector rings . . . . .	31
2.5	A schematic diagram of PiP . . . . .	33
2.6	A schematic diagram of a TOF stand . . . . .	34
2.7	The experimental layout . . . . .	36
2.8	The 1 <sup>st</sup> Level, Fast Trigger . . . . .	38
2.9	The 2nd Level Trigger . . . . .	40
2.10	$\Delta E_{PiP}$ vs E plot for particle identification . . . . .	41
3.1	Pedestal and discriminator threshold . . . . .	46
3.2	The effect of ‘Walk’ . . . . .	47
3.3	Scintillator response to protons and electrons . . . . .	50
3.4	Application of the start correction to the $\Delta E_{start}$ . . . . .	53

3.5	Tagger time spectrum . . . . .	54
3.6	PiP Gain Monitoring and Droop . . . . .	55
3.7	Calculated proton energy ( $\text{MeV}_{ee}$ ) vs Measured proton energy ( $\text{MeV}_{ee}$ ) for PiP . . . . .	57
3.8	TOF position calibration . . . . .	58
3.9	Determining the tzero from the gamma flash . . . . .	59
3.10	Sail plot for single TOF bar . . . . .	61
3.11	Determining the parameters needed for the reconstruction of miss- ing QDC's . . . . .	63
3.12	Missing energy spectrum for $\text{CD}_2$ . . . . .	65
3.13	Energy resolution for PiP and TOF . . . . .	66
3.14	Angular resolution of PiP . . . . .	67
4.1	Proton selection in PiP . . . . .	71
4.2	$TDC_{mean}$ for a TOF bar . . . . .	75
4.3	Proton selection in TOF . . . . .	76
4.4	Tagger randoms subtraction . . . . .	78
4.5	Tagging Efficiency as a function of Photon energy . . . . .	81
4.6	Proton Efficiency as a function of Proton energy . . . . .	82
4.7	Neutron Efficiency as a function of Neutron energy . . . . .	83
4.8	TOF randoms contamination for $^{12}\text{C}(\gamma, 3N)$ analysis . . . . .	88
5.1	Colour coding for the Valencia model predictions . . . . .	95
5.2	$^{12}\text{C}(\gamma, pn)$ $E_m$ distributions compared with the predictions of the Valencia model in QD kinematics. . . . .	96
5.3	$^{12}\text{C}(\gamma, pn)$ $E_m$ distributions compared with the predictions of the Valencia model in NQD kinematics. . . . .	97

5.4	$^{12}C(\gamma, pp)$ $E_m$ distributions compared with the predictions of the Valencia model in QD kinematics. . . . .	100
5.5	$^{12}C(\gamma, pp)$ $E_m$ distributions compared with the predictions of the Valencia model in NQD kinematics. . . . .	101
5.6	$^{12}C(\gamma, pn)$ $E_m$ distributions compared with the predictions of the 2N model for QD/NQD kinematics. . . . .	105
5.7	$^{12}C(\gamma, pn)$ $P_m$ distributions compared with the predictions of the 2N model for QD kinematics . . . . .	109
5.8	$^{12}C(\gamma, pn)$ $P_m$ distributions compared with the predictions of the 2N model for NQD kinematics . . . . .	110
5.9	$^{12}C(\gamma, pn)$ $\theta_{rec}$ distributions compared with the predictions of the 2N model for QD kinematics . . . . .	114
5.10	$^{12}C(\gamma, pn)$ $\theta_{rec}$ distributions compared with the predictions of the 2N model for NQD kinematics . . . . .	115
5.11	$^{12}C(\gamma, pp)$ $E_m$ distributions compared with the predictions of the 2N model for QD/NQD kinematics. . . . .	117
5.12	$^{12}C(\gamma, pp)$ $P_m$ distributions compared with the predictions of the 2N model for QD kinematics . . . . .	118
5.13	$^{12}C(\gamma, pp)$ $P_m$ distributions compared with the predictions of the 2N model for NQD kinematics . . . . .	119
5.14	$^{12}C(\gamma, pp)$ $\theta_{rec}$ distributions compared with the predictions of the 2N model for QD kinematics. . . . .	123
5.15	$^{12}C(\gamma, pp)$ $\theta_{rec}$ distributions compared with the predictions of the 2N model for QD kinematics. . . . .	124
5.16	$^{12}C(\gamma, ppn)$ $E_m^{3N}$ and particle energy distribution for $E_\gamma=150-400$ MeV compared with the predictions of the Valencia model . . . .	127

5.17	$^{12}\text{C}(\gamma, ppn) E_m^{3N}$ and particle energy distribution for $E_\gamma=400-700$ MeV compared with the predictions of the Valencia model . . . .	128
5.18	$^{12}\text{C}(\gamma, ppp) E_m^{3N}$ and particle energy distributions for $E_\gamma=150-400$ MeV compared with the predictions of the Valencia model. . . .	131
5.19	$^{12}\text{C}(\gamma, ppp) E_m^{3N}$ and particle energy distributions for $E_\gamma=400-700$ MeV compared with the predictions of the Valencia model. . . .	132
5.20	$^{12}\text{C}(\gamma, pnn) E_m^{3N}$ and particle energy distributions for $E_\gamma=150-400$ MeV compared with the predictions of the Valencia model. . . .	137
5.21	$^{12}\text{C}(\gamma, pnn) E_m^{3N}$ and particle energy distributions for $E_\gamma=400-700$ MeV compared with the predictions of the Valencia model. . . .	138

# List of Tables

2.1	The targets. . . . .	30
2.2	Dimensions of the PIP E blocks . . . . .	32
3.1	Summary of detector performance . . . . .	68
5.1	Valencia model $N\pi+ABS$ components for $^{12}C(\gamma, ppn)$ . . . . .	130
5.2	Valencia model $N\pi+ABS$ components for $^{12}C(\gamma, ppp)$ . . . . .	134
5.3	Valencia model $N\pi+ABS$ components for $^{12}C(\gamma, pnn)$ . . . . .	136
A.1	Correction factors for dead TOF bars. . . . .	148

# **Chapter 1**

## **Introduction**

## 1.1 Introduction

This work presents the results of a study of the  $^{12}\text{C}(\gamma, 2N)$  and  $^{12}\text{C}(\gamma, 3N)$  reactions carried out with a large phase space acceptance which predominantly covered the relatively more extreme (non- $2N$ ) kinematics.

### 1.1.1 Outline

Photonuclear physics has progressed greatly in recent years due mainly to improved technology allowing high quality, high duty factor photon beams to be produced. This has allowed good quality data from the inherently small photonuclear cross sections to be obtained. In turn the availability of accurate  $(\gamma, 2N)$  cross sections has spurred a great deal of theoretical interest in recent years. The exploration of higher particle multiplicity channels like  $(\gamma, 3N)$  has also become feasible, which in partnership with the  $2N$  channels are providing an opportunity to obtain a wider and more fundamental physical understanding of nuclear processes and interactions.

Early theoretical studies of the nucleus avoided dealing explicitly with the fundamental details of the nucleon-nucleon interaction. The nuclear shell model (SM) approximated the sum of all the interactions between the nucleons using a central mean field potential in which the nucleons were assumed to move independently. Although at first sight appearing to be a rather naive model it was successful in explaining many experimental results, in particular the excitation level schemes of a wide range of nuclei. The approximations included in the the model still allowed a good description of the nucleus due to the limited range of the NN interaction and the restriction of NN scattering by Pauli blocking.

These approximations however mean that the SM theory is insensitive to the details of the NN interaction, especially at short range. The underestimation of

the occupation probabilities of valence shells in nuclei by the model [1] is taken as evidence of repulsive NN scattering in the nucleus, which is not accounted for in the independent particle approximation.

In the 1950's the discovery of strong emission of correlated pairs from the  $(\gamma, pn)$  reaction [2] seemed a promising tool to explore the short range nature of the NN interaction. Modern theories, supported by recent data, indicate that the reaction is dominated by absorption on medium range meson exchange currents (MEC) which tend to mask the effects of short range correlations (SRC). A thorough understanding of the  $(\gamma, pn)$  reaction over a wide range of photon energies and kinematics is a pre-requisite for extracting information about SRC and MEC in this channel.

The  $(\gamma, pp)$  reaction has attracted a great deal of interest due to the suppression of MEC between the T=1 pair. Although the measured cross sections are smaller the reaction shows increased sensitivity to different absorption mechanisms such as SRC or intermediate  $\Delta$  excitation.

In parallel with understanding the short range nature of the NN interaction recent work has begun to study the contribution of three body forces in nuclei. The main evidence for the need of a three body component in the nucleon interaction lies in the failure of microscopic theories based on 2 body forces to explain the binding energy of  $A = 3$  nuclei [3].

### 1.1.2 Photoabsorption

The photon is well suited to the study of nuclear structure as its relatively weak electromagnetic interaction with the constituent nucleons allows it to penetrate the entire volume of the nucleus. This gives it a distinct advantage over strongly interacting probes where surface absorption is dominant and the incoming probe suffers substantial perturbations by the target nucleus (Initial State Interaction).

As the photon is an electromagnetic probe it views the nuclear medium as a collection of charges, currents and magnetisation densities to which it can couple. The total photoabsorption cross section per nucleon ( $\sigma^{ABS}/A$ ), representing the probability of a photon interacting with the target and being removed from the beam flux, is shown as figure 1.1.

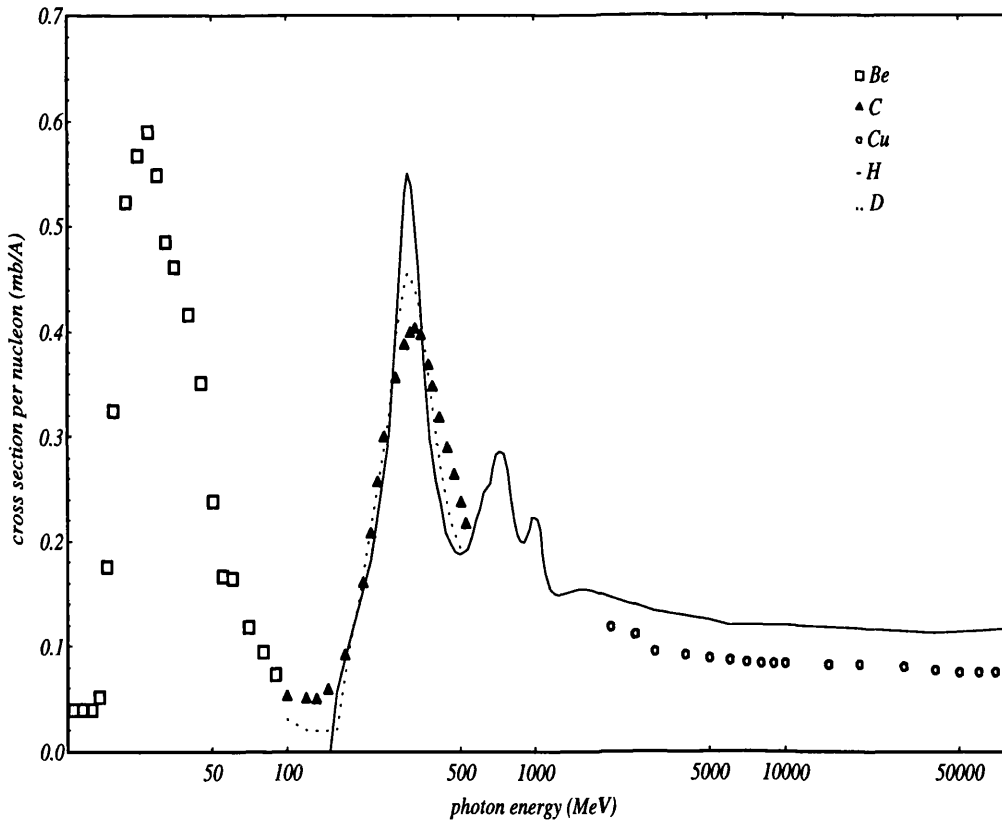


Figure 1.1: *Total photon absorption cross section per nucleon*

The structures to which the photon couples are seen to be dependent on the energy, and therefore wavelength of the incident photon. The value of the total photon absorption cross section at any given photon energy represents the coherent sum of the different contributing photoabsorption reaction mechanisms. Discussed below are the competing reaction channels for different photon energy regions and a discussion of their contribution to the  $(\gamma, 2N)$  and  $(\gamma, 3N)$  cross

sections.

- **Dipole Resonance**

The broad structure centred around  $E_\gamma \sim 30$  MeV corresponds to a photon wavelength of the order of a nuclear radius. In this region the photon couples to the whole nucleus which is viewed (to first order) as an electric dipole, produced by the relative motion of the neutrons and protons. The nucleus thus absorbs the energy of the photon and forms an excited state which decays with the emission of nucleon(s). In medium and heavy nuclei neutrons are preferentially emitted, as they are uncharged and therefore do not have to overcome the Coulomb barrier to leave the nucleus.

- **Delta Resonance**

The second structure at around 300 MeV is due to the  $P_{33}(1232)$  ( $\Delta$ ) nucleon resonance, occurring when the wavelength of the photon is comparable with the size of a nucleon. The  $\Delta$  resonance is thought to be broader for a nucleus than a single nucleon due to medium modification effects ie. Fermi motion, Pauli blocking, and the propagation/interaction of the  $\Delta$  in the nuclear medium. This is supported by the fact that the mass and the width of the  $\Delta$  resonance in nuclei is seen to increase almost linearly with the nuclear density [4].

The  $\Delta$  is unstable and rapidly decays to a nucleon and a pion. The produced pions have a large probability of interacting with the residual nucleus through subsequent  $(\pi, \pi')$  or  $(\pi, 2N)$  reactions. Therefore at photon energies around the resonance the contribution of these multistep processes to the emission of 2 or more nucleons will be substantial.

- **2N Absorption**

Between the  $\Delta$  and giant dipole resonances the photon interacts with the nucleus at a scale comparable with that of the inter-nucleon spacing. As the single nucleon knockout strength is strongly suppressed at these photon energies, due to momentum conservation requirements, the region is dominated by absorption on nucleon pairs ( $2N$ ). The photon is primarily absorbed by  $T=0$  ( $pn$ ) pairs with the cross section for absorption on  $T=1$  pairs ( $pp, nn$ ) an order of magnitude less due to the suppression of meson exchange currents (MEC).

Although for energies above this region the total photoabsorption cross section is dominated by pion production the weaker  $2N$  absorption process still contributes. The study of the direct  $2N$  process at higher photon energies up to and beyond the  $\Delta$  resonance is an important source of information for a full understanding of the mechanism(s) involved.

- **3N Absorption**

This channel is of particular interest as the direct reaction ( $3N_{direct}$ ) where no real pions are involved in the mechanism, may be related to the elusive three body force in nuclei. This  $3N_{direct}$  channel will be weaker than that of  $2N$  due to the lower probability of finding three nucleons in the nucleus at a close enough range to interact. Although the  $3N_{direct}$  process contributes to the measured  $(\gamma, 2N)$  strength the  $(\gamma, 3N)$  cross section should be more sensitive to this process.

Photon absorption leading to the emission of three nucleons does not however have to originate from a direct process. Multistep processes such as initial quasi-free pion production in the nucleus followed by pion absorption on a nucleon pair will also produce three nucleons in the final state ( $N\pi+ABS$ ). The  $(\gamma, 3N)$  cross section may also have contributions from

initial  $2N$  processes followed by a final state interaction ( $2N+FSI$ ) which results in an additional nucleon escaping the nucleus.

- **Higher Resonances**

The structures evident above 500 MeV on the total photoabsorption cross section from the proton are attributed to the higher nucleon resonances ( $N^*$  and  $\Delta^*$ ). These structures however are not observed in experiments on heavier nuclei. Recently Bianchi *et al* [4] attributed the effect to a strong hadronic interaction with the nuclear medium in the propagation of the produced resonances which tends to smear their contribution to the absorption cross section. These higher resonances are presently an active area of research.

- **Shadowing Region**

At energies above  $\sim 2\text{GeV}$  the cross section is generally flat and relatively small. It is attributed to reactions dominantly involving the hadronic components of the photon. The onset of reactions of this type is not particularly well studied with some theories [5] predicting significant interactions through low mass hadronic components for energies as low as 1 GeV.

The present study covers photon energies from 150-700MeV and so a detailed understanding of the observed photo-nuclear reactions relies on the identification of events originating from the different mechanisms occurring in this region.

## 1.2 Review Of Previous Experiments

### 1.2.1 $(\gamma, 2N)$ measurements

Early  $(\gamma, 2N)$  photonuclear experiments [6, 7, 8, 9] were limited due to the use of continuous bremsstrahlung techniques which did not accurately determine the photon energy. These experiments not only gave relatively poor statistics but also had to make assumptions about the excitation of the residual nucleus. Although limited in scope these experiments suggested ‘quasi-deuteron’ (QD) behaviour of the emitted pairs in  $(\gamma, pn)$  reactions on several light nuclei ( ${}^4\text{He}$ ,  ${}^6\text{Li}$ ,  ${}^{12}\text{C}$ ,  ${}^{16}\text{O}$ ). For a fixed proton energy the centre of mass opening angle formed by the correlated neutrons was found to be around that of the deuteron, although smeared out because of the Fermi motion of the pair before the interaction.

The more recent development of monoenergetic tagged photon beams and detectors with better resolution has produced much higher quality data. Measurements for photon energies of  $\sim 200\text{-}450$  MeV at Bonn by Arends *et al* [10] and at Tokyo [11, 12, 13] studied the proton momentum spectra for events with a correlated nucleon on the opposite side of the beam. The results gave more evidence for the QD like angular correlation in the  $(\gamma, pn)$  and  $(\gamma, pp)$  channels. The interpretation of the data was however still limited by the relatively poor resolutions of the detector systems.

A systematic survey of the  $(\gamma, 2N)$  reactions was undertaken by the Glasgow group in collaboration with Edinburgh, Mainz and Tübingen universities [14, 15, 16, 17, 18] at photon energies up to  $\sim 150$  MeV. The experimental resolution of these experiments ( $\sim 7$  MeV) was sufficient to distinguish the shells from which the nucleons were emitted, allowing more meaningful tests of the contribution of direct 2N reactions as well as giving some assessments of FSI contributions.

Early investigations of the  $(\gamma, 2N)$  reaction in  ${}^{16}\text{O}$  [15] and  ${}^{12}\text{C}$  [16], for  $E_\gamma=80\text{-}$

131 MeV and 80-157 MeV respectively, showed a peak in the  $(\gamma, pn)$  missing energy ( $E_m$ ) distribution corresponding to leaving the residual  $(A-2)$  system in or near its ground state. The shape of the missing energy distribution could be fitted well by the folding of two single nucleon missing energy distributions, obtained from electron scattering  $(e, e'p)$  data. The relative contributing strengths of the  $(1p)^2$ ,  $(1s)(1p)$  and  $(1s)^2$  pairs were derived from the nucleon numbers in each shell. The  $(\gamma, pp)$  reaction, although possessing strength at low  $E_m$ , did not have the same characteristic peak near to threshold and the shape of the distribution was not well produced by folding single nucleon distributions.

For regions of low excitation of the residual nucleus ( $E_m \leq 40$  MeV) the missing momentum distributions in the  $(\gamma, pn)$  channel were entirely described by the process of photon absorption on a  $(1p)^2$  proton-neutron pair, with the residual nucleus acting as a spectator to the reaction. The same region in the  $(\gamma, pp)$  channel surprisingly also gave reasonable agreement with a model based on the absorption on  $(1p)^2$  proton pairs. The interpretation of data with higher excitation energies was limited due to large detector threshold effects and small phase space coverage.

The upgrade of the electron microtron and photon tagger at Mainz allowed the study to continue into photon energies around the  $\Delta$  resonance. Results for  $E_\gamma=150-400$  MeV [19] confirmed the dominance of photon absorption on  $(1p)^2$  pairs for  $E_m \leq 40$  MeV. A higher  $E_m$  region covering 40-70 MeV showed dominant absorption on  $(1s)(1p)$  pairs, although indications of FSI contributions were also found in this region. The  $(\gamma, pp)$  channel again indicated some form of 2N interaction was involved although the influence of FSI processes in the higher  $E_m$  region was found to be significant.

Subsequent work extended the study [20] and explored the angular distribution of the  $(\gamma, pn)$  and  $(\gamma, pp)$  reactions. The detectors were positioned to cover

the back-to-back kinematics of a direct 2N emission process. Three consecutive measurements with the back-to-back detector setup rotated around the target allowed the angular distribution of the 2N process to be investigated over a wide range of proton angles ( $\theta_p=20^\circ-130^\circ$ ).

For the  $(\gamma, pn)$  reaction the angular distribution for  $E_\gamma=140$  MeV and  $E_m \leq 70$  MeV showed a broad maximum at around  $80^\circ$ , attributed from the theory of Ryckebush et al [21, 22] to the interference between the heavier  $\rho$  meson exchange and pion exchange currents between the pn pair. The  $(\gamma, pp)$  angular distribution showed a large dissimilarity to the  $(\gamma, pn)$  for the low  $E_m \leq 40$  MeV region, inferring a different underlying photon absorption mechanism. For  $E_m=40-70$  MeV the two channels showed more similar characteristics which may be taken as an indication of the stronger contribution of charge exchange FSI events, transferring strength from the  $(\gamma, pn)$  to the  $(\gamma, pp)$  channel at higher  $E_m$ .

### 1.2.2 Review of experimental studies of multiparticle mechanisms

Most experimental data investigating the role of multinucleon absorption has come from  $\pi$  beam experiments [23] where this mode is well established. The relative strength of the multinucleon mode compared with the 2N mechanism was shown to be significant across the  $\Delta$  resonance and to increase with nuclear mass and incident pion energy. The interpretation of the results from  $\pi$  experiments was complicated by the possible contribution from initial state interaction (ISI) processes preceding 2N absorption, although this alone could not account for the observed multinucleon yield.

Most attempts to assess the 3 nucleon absorption in photon experiments have concentrated on light nuclei, mainly  $^3\text{He}$ , where the detection of two nucleons

allows the momentum of the third (undetected) nucleon to be deduced from the kinematics. Following the suggestion of Laget [24] the  $(\gamma, pp)n$  reaction has been extensively studied, to investigate 3-body mechanisms in the favourable situation where the 2-body strength is suppressed.

Audit *et al* [25] measured the  ${}^3\text{He}(\gamma, pp)n$  reaction for 5 photon energies in the range 231-414 MeV, for low neutron recoil momentum. Even with the detectors in the more usual quasi-free 2N kinematics the observed cross sections showed an excess over the 1N/2N(+FSI) predictions of Laget. As the excess occurred away from the quasi-free 2N peak in the proton momenta distributions the results were taken as an indication of contributing 3N mechanisms. The inclusion of 3N processes in the Laget calculation reproduced the general shape of the data although with an underestimation of the cross section magnitude for lower photon energies.

Further work for  $E_\gamma=90$ -250 MeV at Saskatchewan was carried out by Sarty *et al* [26]. The detectors were positioned away from the 2N kinematics in a region of phase space predicted by the Laget calculations to maximise the contribution of  $3N_{\text{direct}}$  absorption mechanisms. The differential cross section, plotted as a function of the (undetected) neutron momentum, again demonstrated that 1N/2N(+FSI) photoabsorption mechanisms alone could not describe the data. For higher neutron momenta the measurement was a factor 5-9 greater than the Laget prediction. However the inclusion of 3N processes allowed an adequate prediction of the measured cross section.

3N absorption contributions were also evident in the  $E_\gamma=200$ -500 MeV data from the TAGX collaboration [27] which had a larger solid angle coverage than previous measurements ( $\sim 3$  sr). The shape of the  ${}^3\text{He}(\gamma, pp)n$  neutron momentum distributions could only be reproduced from both 2N and 3N model distributions, with the 3N contribution shown to dominate for higher photon

energies.

A recent study of the  ${}^3\text{He}(\gamma, pp)n$  reaction for  $E_\gamma=200\text{-}800$  MeV with the large acceptance detector Daphne [28] estimated the 3N absorption strength in the  $\Delta$  region to constitute  $\sim 36\%$  of the 2N strength. From invariant mass studies the mechanism was found to be dominated by the 2 step process involving the intermediate production of a real pion ( $N\pi+\text{ABS}$ ), although for photon energies above 500 MeV the signature of this mechanism was not clear.

Relatively little data is available for heavier nuclei. Recent work on  ${}^{12}\text{C}$  by Harty *et al* [29] at Mainz investigated the contribution of  $(\gamma, ppp)$  reactions to the observed  $(\gamma, pp)$  cross sections in 2N kinematics. Comparisons with the Valencia model [40] again attributed most of the observed  $(\gamma, ppp)$  strength to the  $N\pi+\text{ABS}$  process.

This work improves upon the previous  ${}^{12}\text{C}$  measurement due to a better detector coverage, more suited to the kinematics of multiparticle mechanisms. The improved detector segmentation will also enable the contribution of different final charge states to be investigated.

## 1.3 Review of Theoretical Progress

### 1.3.1 $(\gamma, 2N)$ reactions

Early compound nucleus models of photoreactions assumed a two step process where the photon is absorbed, leading to an intermediate excited state which decays to stability by emitting nucleons. The theory predicted that neutron emission was a factor  $\sim 10^3 - 10^5$  more likely than the emission of protons, due to the influence of the Coulomb barrier, and that the angular distribution of the emitted particles would be isotropic. Although this model was in reasonable agreement for low (giant dipole resonance) photon energies, at higher energies

the proton distribution obtained was larger, more forward peaked and contained many more high energy protons than the compound model predicted. This led to the conclusion that the photon was being absorbed on a subset of the nucleus rather than the entire nucleus itself. Levinger [31] proposed that the photon was being absorbed on a nucleon pair, with the residual nucleus acting as a spectator to the reaction. As this theory assumes absorption on a T=0 pn pair (due to its dipole nature) the theory became known as the ‘quasi-deuteron’ model. The deuterium cross section is effectively mapped into the nucleus through the relation:

$$\sigma_{QD} = L \frac{NZ}{A} \sigma_D \quad (1.1)$$

The factor  $\frac{NZ}{A}$  represents the number of deuteron pairs in the nucleus and  $L$  is the Levinger constant. The Levinger constant is interpreted as the ratio of the probability of the proton-neutron pair being close enough to interact in a complex nucleus to that in the deuteron.

The theory is in many respects a somewhat naive model with no accounting for Pauli blocking, Fermi motion or FSI effects. However many aspects of the NN interaction are included in a phenomenological way through the inclusion of the deuteron cross section ( $\sigma_D$ ).

An improved theory was proposed by by Gottfried [32] who factorised the cross section for the emission of proton-neutron pairs from a spectating residual nucleus after absorption of a photon of momentum  $\omega$  as:

$$d\sigma = \frac{1}{(2\pi)^4} F(P) S_{fi} \delta(\epsilon - \bar{\epsilon}) d^3k_1 d^3k_2 \quad (1.2)$$

With  $k_1$  and  $k_2$  the momenta of the two nucleons and  $F(P)$  the probability of finding two nucleons of zero separation and momentum  $P = |k_1 + k_2 - \omega|$ . The  $F(P)$  term is proportional to the nucleon pair momentum distribution in

the initial state and depends only on the long range (shell model) properties of the nucleon wavefunctions. The  $S_{fi}$  term is a transition matrix which embodies the dynamics of the reaction beyond the independent particle shell model and thus includes shorter range aspects of the two nucleon correlation function not accounted for by the (shell model) mean field.

A more microscopic approach to the problem was taken by Boato and Giannini [33] who calculated the  $(\gamma, pn)$  cross section including one and two body terms. Following previous theoretical work only the dominant seagull absorption term, depicted on figure 1.2, was included in the calculation. The nucleons were assumed to be at zero separation at the time of the absorption and suffer no subsequent interaction (FSI) with the residual nucleus. Even with the first order MEC currents included in the calculation the cross section was shown to still be factorisable into the pair momentum distribution and a second term which depends on short range components. For  $(\gamma, pn)$  the short range components were predicted to be dominated by isovector MEC terms.

A subsequent paper [34] incorporated the effects of FSI using an optical potential. The factorisation of the cross section was again employed with the FSI effects included in the  $F(P)$  and  $S_{fi}$  terms separately. Although the inclusion of the FSI process produced a reduction in the magnitude of the predicted cross section, the shape of the angular distribution was not significantly altered.

The  $(\gamma, pp)$  channel was investigated by Giusti et al [35]. As well as the 'seagull' MEC intermediate  $\Delta$  configurations were included which were expected to be an important mechanism in the  $(\gamma, pp)$  channel. The theory employed an unfactorised framework, using realistic SRC functions and accounted for FSI using a distorted wave approximation for the outgoing nucleons. The contribution of one body currents was found to be highly dependent on the choice of correlation function.

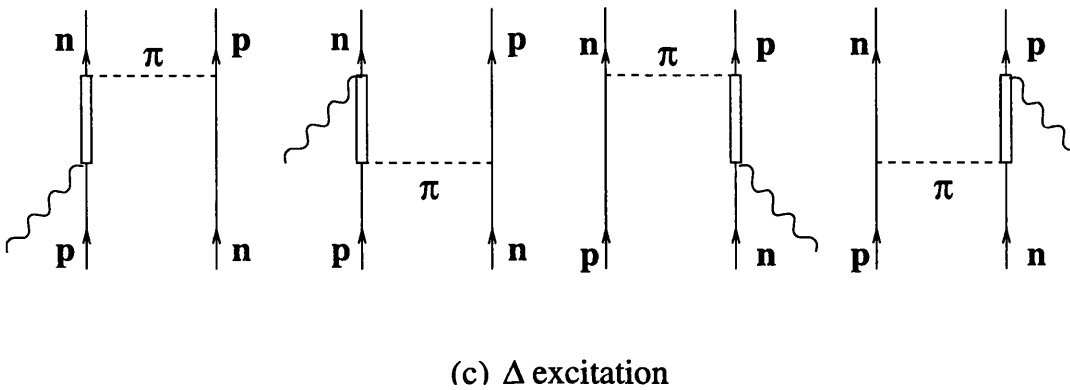
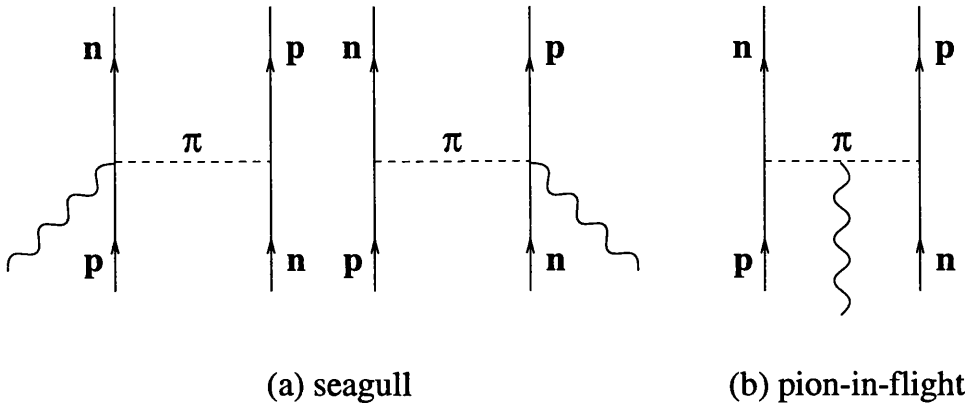


Figure 1.2: Absorption terms considered for the  $(\gamma, pn)$  emission

This treatment was applied to the  $(\gamma, pn)$  channel by Boffi *et al*, whose theory predicted dominant absorption on  $^3S_1$  pn pairs (quasi-deuteron) for low photon energies ( $\sim 80$  MeV). The seagull term, although shown to be dominant for lower photon energies, was predicted to decrease in importance for increasing photon energy with the contribution of 1-body and  $\Delta$  currents predicted to rise.

The Gent group has recently undertaken a very thorough study of the  $(\gamma, NN)$  reactions [21]. The calculations include higher order terms in the pion propagator such as the pion in flight contribution (see figure 1.2) and the exchange of heavier ( $\sigma, \omega, \rho$ ) mesons. At  $E_\gamma \sim 140$  MeV the pion in flight term was found to destructively interfere with the dominant seagull current, resulting in a consid-

erable reduction and change of shape of the angular cross section. Although the  $\sigma$  and  $\omega$  currents were found to have a negligible effect on the cross section the  $\rho$  meson was predicted to also produce visible interference effects in the angular distribution of the emitted particles.

The Gent group's predictions for  $^{16}\text{O}$  within an unfactorised framework [36] assessed the validity of Gottfried's zero range and quasi-deuteron assumptions. The unfactorised calculation employed harmonic oscillator wave functions to describe the 2 hole states after the photon interaction, with the contribution of FSI and absorption on one-body currents (SRC) neglected. The factorisation of the cross section was shown to result in a larger predicted cross section than the more exact unfactorised approach for the lower photon energies (see figure 1.3). This

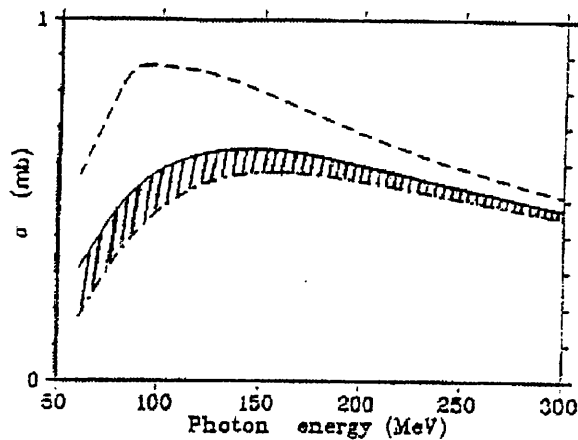


Figure 1.3: Comparison of unfactorised and factorised approach in calculating the  $^{16}\text{O}(\gamma, pn)$  cross section. The dashed line shows the cross section calculated with Gottfried's factorised approach. The dot-dashed line was obtained with the unfactorised approach and restricting the sum over the relative S waves only. The solid line shows the results for an unfactorised calculation but with no restriction on the relative pn waves.

was understood to be due to the low momentum photons coupling to longer range MEC, leading to a breakdown of the Gottfried zero range assumption. For  $E_\gamma \sim 60$  MeV the contribution of pn pairs in relative P waves can be seen to account for

half the total cross section and so the quasi-deuteron approximation, where only  $^3S_1$  states contribute, also breaks down. The results however show the validity of the factorised approach for photon energies approaching the  $\Delta$  resonance.

### 1.3.2 The 2N photon absorption model

In order to allow the contribution of the 2N photon absorption mechanism to be assessed, a Monte Carlo code to simulate the 2N absorption reaction was developed (2N model). This 2N model can be used to predict the distribution of the variables which were deduced from the data assuming a direct (no FSI) 2N emission process in a spectating nucleus. Although the calculation does not involve any assumptions about the microscopic absorption mechanisms, its ability to account for the observed features of the experimental data gives an indication of the importance of direct 2N emission processes to the measured yield.

The momentum distribution of the nucleon pair ( $F(P)$ ) was reconstructed from the folding of individual simple harmonic oscillator (SHO) wavefunctions, with the parameter  $\beta$  ( $=0.359 \text{ fm}^{-1}$ ) chosen to give the correct RMS radius [37] of  $^{12}\text{C}$ . The functions obtained for different initial shell combinations are shown below.

$$\mathbf{F}_{1p1p}(\mathbf{P}) = \frac{8}{15\sqrt{2\beta^3\pi}} \left( 3 - \frac{\mathbf{P}^2}{\beta} + \frac{\mathbf{P}^4}{4\beta^2} \right) \exp\left(-\frac{\mathbf{P}^2}{2\beta}\right) \quad (1.3)$$

$$\mathbf{F}_{1p1s}(\mathbf{P}) = \frac{2}{3\sqrt{2\beta^3\pi}} \left( \frac{\mathbf{P}^2}{\beta} \right) \exp\left(-\frac{\mathbf{P}^2}{2\beta}\right) \quad (1.4)$$

$$\mathbf{F}_{1s1s}(\mathbf{P}) = \frac{2}{2\sqrt{2\beta^3\pi}} \exp\left(-\frac{\mathbf{P}^2}{2\beta}\right) \quad (1.5)$$

The magnitude of the initial momentum of the interacting nucleon pair was selected from the corresponding  $P^2F(P)$  distributions, with the direction of  $\mathbf{P}$  chosen

isotropically.

The excitation of the residual nucleus ( $E_x$ ) was taken from a distribution, chosen in an iterative procedure so that the shape of the predicted missing energy cut on detector acceptances matched that of the observed data. The energy of the initial pair before the interaction could then be calculated, assuming a spectating residual nucleus, according to the formula  $M_t - (M_r + T_r + E_x)$  [15] where the subscripts t and r correspond to target and recoil respectively. The momenta of the outgoing nucleons were obtained in the centre of mass frame of the incoming photon and the nucleon pair. The directions of the nucleons were chosen either from the  $D(\gamma, pn)$  angular distribution in the case of  $(\gamma, pn)$  or from an isotropic distribution for  $(\gamma, pp)$ .

By applying experimental detector geometry and threshold conditions the predictions of the 2N model can be compared directly with experiment.

## 1.4 Review of multiparticle theories

Only in recent years have theories been developed which include the contribution of multiparticle photon absorption channels. The microscopic models of Laget [24, 38] for the  ${}^3\text{He}(\gamma, pp)n$  reaction calculated the total 3N cross sections from the basic Feynman diagrams explicitly including both real and virtual pion processes. Along with the 1N/2N(+FSI) contributions the theory gives reasonable descriptions of the available data.

The Laget theories are however only tractable in light nuclei and therefore cannot be used in a direct comparison with the present work. The most comprehensive theory currently available for photoreactions in heavier nuclei is the Valencia model [40] developed by Carrasco and Oset.

### 1.4.1 The Valencia model

The approach taken by the Valencia group was to create a microscopic model of all known and important reaction processes that can occur in nuclear photon absorption and then to track the products of these reactions through the nuclear medium, using a semi-classical approach to account for any further interactions in the nucleus. The model uses a nuclear matter approximation which although compromising the structure of real nuclei allows plane waves to be used for the particle states.

The initial photon absorption mechanisms are calculated in a microscopic many-body quantum mechanical framework, explicitly accounting for both pion production and nucleon absorption. The interactions between photons, pions, nucleons and  $\Delta$ 's are expressed in terms of the relevant coupling constants, form factors and propagators. The photon, of energy ( $\omega$ ), upon entering the nuclear medium is assigned a complex self-energy  $\Pi(\omega, \rho)$  where  $\rho$  is the nuclear matter density. The self-energy accounts for the photon's possible interactions with the nuclear medium. Figure 1.4 shows the photon creating two particle-hole (ph) excitations, which form one component of the self-energy. Further diagrams come from including different numbers of ph excitations or from the effects of long range correlations or medium polarisation. The latter two are included in the self energy diagrams using a random phase approximation to describe additional ph or  $\Delta$ h propagation in the medium.

The constructed self energy allows the total cross section for each possible process to be calculated. The scattering probability per unit volume ( $= -\frac{1}{\omega} \text{Im} \Pi(\omega, \rho)$ ) is related to that of the nuclear volume ( $\sigma$ ) by use of a local density approximation ( $\rho \rightarrow \rho(r)$ ).

$$\sigma = -\frac{1}{\omega} \int d^3r \operatorname{Im} \Pi(\omega, \rho(r)) \quad (1.6)$$

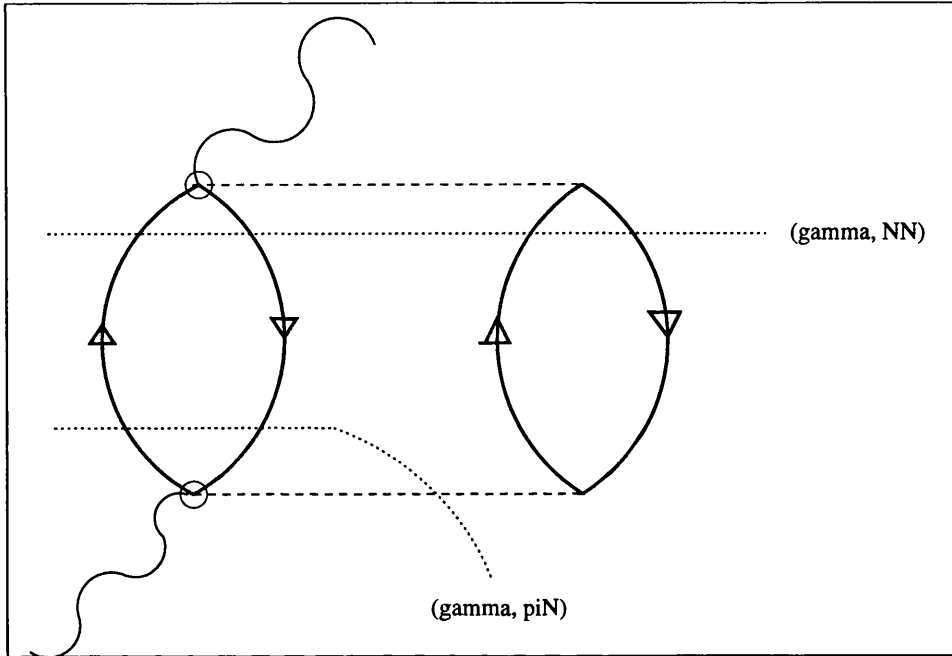


Figure 1.4: A typical photon self energy diagram corresponding to a 2p2h excitation. The upper cut corresponds to  $(\gamma, 2N)$  (ie 2 particles and two holes placed on shell) whilst the lower corresponds to  $(\gamma, N\pi)$

The imaginary parts of the photon self energy are obtained by applying Cutkosky rules to each component diagram, with each cut representing a separate interaction mechanism. Two such cuts are illustrated on figure 1.4 with the upper cut contributing to the  $(\gamma, NN)$  process and the lower to  $\pi$  production. For each line intersected by the cut the relevant propagator is replaced with its imaginary part, forcing the particles present to appear on shell.

The interaction of the produced on-shell particles with the nuclear medium is accounted for by a semi-classical Monte Carlo treatment. The particles are moved classically through the medium in small steps, with the Monte Carlo procedure selecting whether the particle undergoes an interaction on the basis of the

calculated mean free path. For nucleons the interaction is limited to NN scattering processes which were modelled using the available nucleon-nucleus optical potentials [41] modified to account for nuclear medium effects. Pions could be either scattered ( $\pi, \pi'$ ) or absorbed ( $\pi, 2N$ ), ( $\pi, 3N$ ). The probabilities for each pion reaction were obtained from many body quantum mechanical calculations [42], which include the effects of single and double charge exchange as well as medium effects.

The Valencia model was devised to predict photo-reactions for photon energies up to 500 MeV. The  $2\pi$  production channel, which does not give a significant contribution in this range, is not included. Any interpretation of the model predictions above 500 MeV should take this omission into consideration. An indication of the importance of these processes is indicated in ref [43] where the  $2\pi$  production channel was seen to be negligible at around 500 MeV but contributes  $\sim 50\%$  of the single  $\pi$  production cross section at 700 MeV.

## 1.5 Summary and Aims of Present Experiment

Previous studies of photonuclear nucleon emission reactions have concentrated on kinematics suited to the back-to-back emission of two nucleons. In contrast the present work will sample the  $(\gamma, 2N)$  cross sections in more extreme kinematics to complement this previous work and allow an assessment of the importance of other processes away from the usual kinematics. In particular the phase space covered will give a good indication of the importance of FSI processes, information which is difficult to extract from a  $(\gamma, 2N)$  measurement in the back-to-back kinematics. More sensitivity to multinucleon mechanisms such as  $3N_{direct}$  absorption or the  $N\pi+ABS$  process is expected.

The detector geometry will also allow the direct  $2N$  emission reactions to

be studied in previously inaccessible, but interesting, regions of high initial pair momenta which only gave small contributions to the yield observed in previous experiments. This work will therefore allow a more stringent test of our understanding of these reactions.

The measurements of the  $(\gamma, 3N)$  reaction will give a good indication of the role of multiparticle mechanisms to the photon absorption process. This work will improve on the previous  $^{12}\text{C}$  measurement [29] which was taken with a detector coverage less sensitive to  $3N$  kinematics and was limited to the study of only one final charge state (ppp). The first detailed measurements of the ppn and pnn final states for an  $A > 3$  nucleus in this work will therefore give valuable information on the multiparticle mechanisms involved in photon absorption.

## **Chapter 2**

# **Experimental Apparatus**

## 2.1 Experimental Apparatus

The experiment forming this thesis was carried out in collaboration with Edinburgh, Mainz and Tübingen Universities using the 855 MeV electron microtron (MAMI-B) at the Institut für Kernphysik at Mainz. The high quality electron beam is used to produce a flux of collimated Bremsstrahlung photons. The photon energies are determined by analysis of the associated residual electrons in the Glasgow Tagging Spectrometer. Two main detector systems (PiP, TOF) are employed to detect products from resulting photonuclear reactions. PiP is a plastic scintillator hodoscope designed to detect protons and positive pions and TOF is a versatile array of scintillators capable of detecting uncharged and charged particles. Segmented rings of thin  $\Delta E$  transmission detectors positioned around the target provide timing and triggering information on the reaction products and also allow a distinction between charged and uncharged particles to be made.

## 2.2 The Mainz Electron Microtron

The MAINZ electron microtron (MAMI-B) comprises three race track microtron stages which result in a high quality 850 MeV electron beam with  $\sim 100\%$  duty factor. The beam is highly stable and can be operated at currents up to  $100\mu\text{A}$ . For the production of tagged photon beams a lower current of  $\sim 20\text{nA}$  is used due to count rate restrictions in the tagging spectrometer.

Figure 2.1 shows a schematic diagram of a typical microtron stage, consisting of two bending magnets and a series of linear accelerators (LINACs). The Linacs consist of waveguides along which the electrons are accelerated by radio frequency (RF) electric fields. The RF power is provided by klystron oscillators.

The bending magnets recirculate electrons back through a series of return pipes to be accelerated further by the Linacs. The radius of the electron orbit

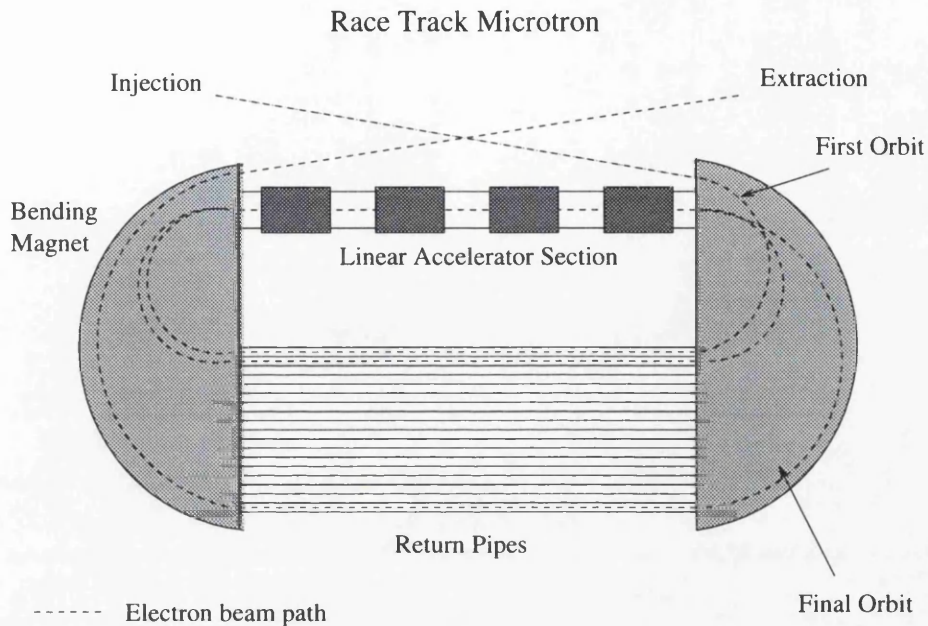


Figure 2.1: *Schematic diagram of a racetrack microtron*

in the magnets increases with increasing electron energy, with the energy boost of the electrons at each pass fixed such that the electrons always arrive in phase with the accelerating field.

As the beam is recirculated many times before extraction the electrons only need to be given a series of relatively small energy boosts to attain the desired beam energy. This allows the accelerating klystrons to be operated in the continuous wave mode to give an essentially continuous beam. (The beam does possess some RF microstructure but the high frequency (2.45GHz) means the beam can be considered continuous for practical purposes.)

A schematic of the MAMI-B accelerator is shown in figure 2.2. The electrons, produced by a 100 keV electron gun, are fed into a linac which accelerates them to an energy of 3.5 MeV. The resultant beam is fed into the first 18 turn microtron (RTM1) which increases the beam energy to 14 MeV. The second 51 turn microtron (RTM2) increases the beam energy to 180 MeV before injection into the

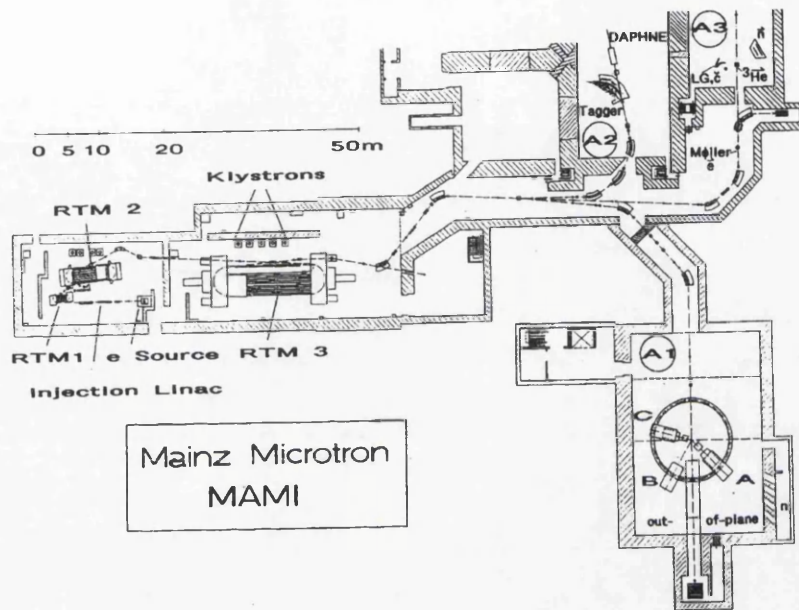


Figure 2.2: Schematic diagram of the Mainz electron microtron (MAMI-B).

final microtron (RTM3) which has 90 turns and produces the final beam energy of 855 MeV. The produced beam has a resolution of 60keV and emittance of less than  $0.14\pi$ .mm.mrad.

The beam can be transported into any of the experimental halls by a series of dipole and quadrupole magnets.

## 2.3 Photon Production

The electron beam from the MAMI accelerator is focussed onto a thin ( $4\ \mu\text{m}$ ) Ni foil. Bremsstrahlung radiation ( $e, e'\gamma$ ) is produced from the deceleration of the electrons in the fields of the Ni nuclei. The produced Bremsstrahlung photons form a forward directed cone which is collimated to form a small spot on the

target downstream. The energy of a photon can be deduced from the incident ( $E_e$ ) and residual ( $E'_e$ ) electron energies.

$$E_\gamma = E_e - E'_e \quad (2.1)$$

The energy distribution of photons produced by this process can be approximated by a  $1/E_\gamma$  distribution except near the end point energy ( $E_\gamma = E_e$ ).

### 2.3.1 The Glasgow Tagging Spectrometer

The photon energy is determined by analysing the residual electrons in the Glasgow Tagging Spectrometer (Tagger) [44, 45]. A schematic diagram of the Tagger is shown in figure 2.3.1. It consists of a large dipole magnet producing a homogeneous field which focuses the electrons onto a 4.5 m focal plane with an intrinsic electron energy resolution of  $\sim 100$  keV. The electrons can also be focussed in the vertical direction by an additional quadrupole magnet positioned downstream from the radiator.

The focal plane [46] is fitted with an array of 352 plastic scintillator elements which give an average energy bite of  $\sim 2$  MeV. Each element is viewed by a separate PM tube, the output of which is fed to a dual threshold discriminator giving a timing resolution  $\leq 1$  ns. The resultant discriminator output pulses are fed to TDCs which provide timing information for each hit. The TDCs are gated by the main detector system to include coincidence events whilst limiting the number of random events recorded.

The scintillators are placed at an angle perpendicular to the electron trajectory with an overlap that ensures a real electron event will fire two elements. Insisting on this double hit coincidence removes signals generated by noise in the PM tubes and also greatly reduces the contribution from background electrons, neutrons

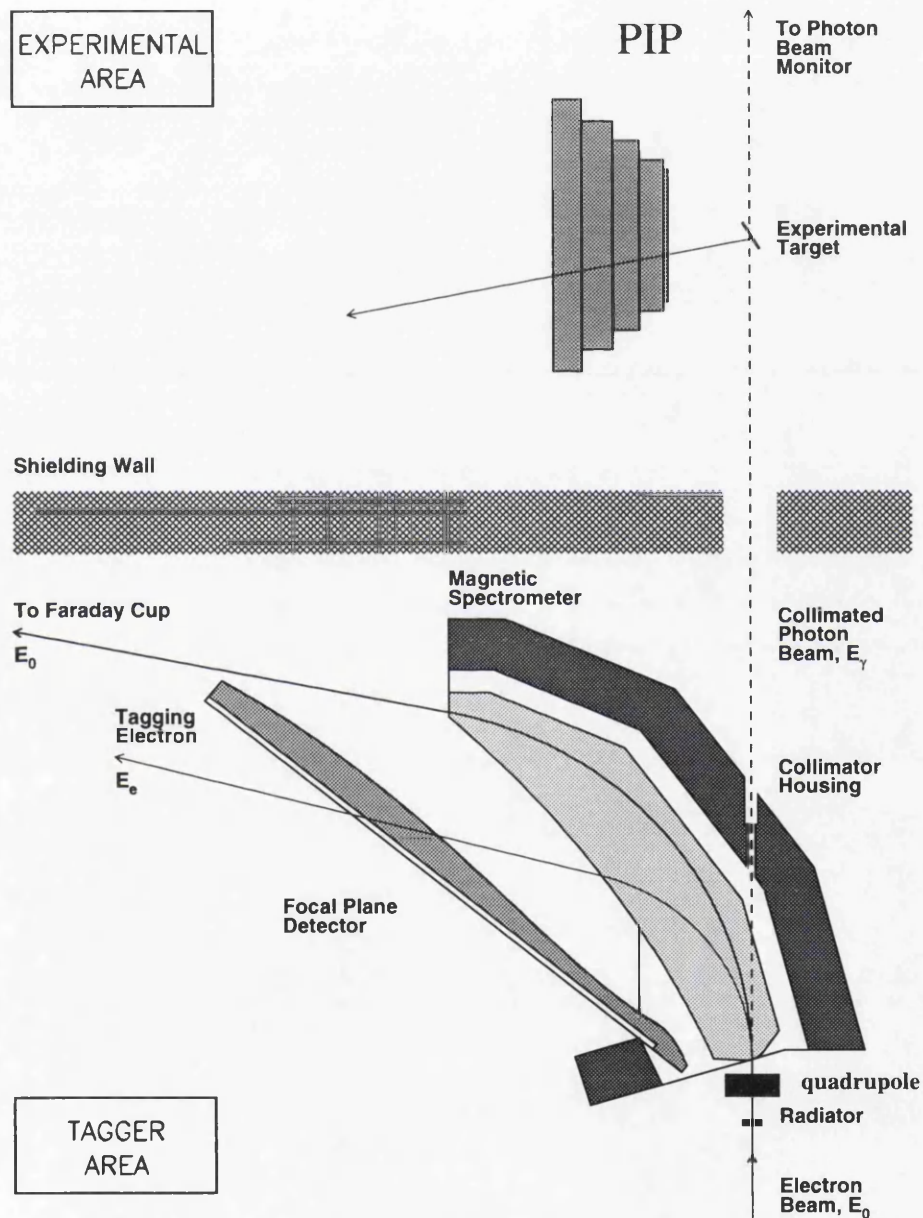


Figure 2.3: Schematic of the tagging spectrometer

and  $\gamma$ 's.

The number of electron events for each element is counted, using FASTBUS scalers, to allow a determination of the photon flux. No scaler dead time correction is required as the scalers are disabled whilst potentially useful events are read out by the data acquisition system.

### 2.3.2 Collimation and Tagging Efficiency

The photon flux leaving the spectrometer is collimated to provide a smaller and more definite beam spot size at the target. This necessarily removes photons from the flux and so the number of electron counts in the focal plane detectors ( $N_e$ ) is not equal to the number of photons incident at the target ( $N_\gamma$ ). To account for this effect the 'tagging efficiency' ( $\epsilon_{tag}$ ) for the experimental setup is obtained, defined as:

$$\epsilon_{tag} = \frac{N_\gamma}{N_e} \quad (2.2)$$

To determine the tagging efficiency a Pb glass detector of thickness equivalent to 30 radiation lengths ( $\sim 100\%$  efficiency) is placed downstream of the collimator in the path of the photon beam. A sufficiently low electron beam current ( $\sim 0.5$  pA) is used to avoid deadtime problems in the Pb glass detector and to ensure that the number of random hits in the tagger focal plane is negligible. A photon hit in the Pb glass detector is used as a trigger to readout the Tagger TDCs, allowing the tagging efficiency for each focal plane element to be simply extracted from the data.

$$\epsilon_{tag} = \frac{TDC_{counts}}{SCALER_{counts}} \quad (2.3)$$

Where  $TDC_{counts}$  is the number of electron hits occurring in coincidence with a

Pb glass photon hit and  $SCALER_{counts}$  represents the total number of electron hits.

Tagging efficiency measurements were made on three separate occasions during the experimental run period and were shown to be stable.

## 2.4 Targets

target	$A$	thickness(mm)	$\rho_s(mg/cm^2)$	$n_{target}(cm^{-2})$
$CD_2$	16.02	2	216.0	$1.623 \times 10^{22}$
$^{12}C$	12.00	4	685.3	$3.439 \times 10^{22}$

Table 2.1: *The targets.*

Two targets were used in the experiment. Detector calibration runs used a deuterated polythene ( $CD_2$ ) target while the main experimental runs were carried out with a graphite ( $^{12}C$ ) target. The characteristics of both targets are listed in Table 2.1

When choosing the target thicknesses several factors must be taken into consideration. A thick target will have more nuclei/ $cm^2$  and so increase the probability of photo-absorption, giving results with improved statistics. This is an important consideration for this experiment as the cross sections for some of the proposed measurements are small. A thick target however also worsens the energy resolution for the emitted (charged) particles as more target material must be traversed to reach the detector, causing the energy loss from ionisation to become more uncertain. The target thicknesses chosen thus represent a compromise between resolution and yield.

The targets were placed at an angle ( $45^\circ$ ) to the photon beam. This increased the effective thickness of the target whilst reducing the amount of target traversed

by those particles detected in PiP.

### 2.4.1 The $\Delta E$ Detector Rings

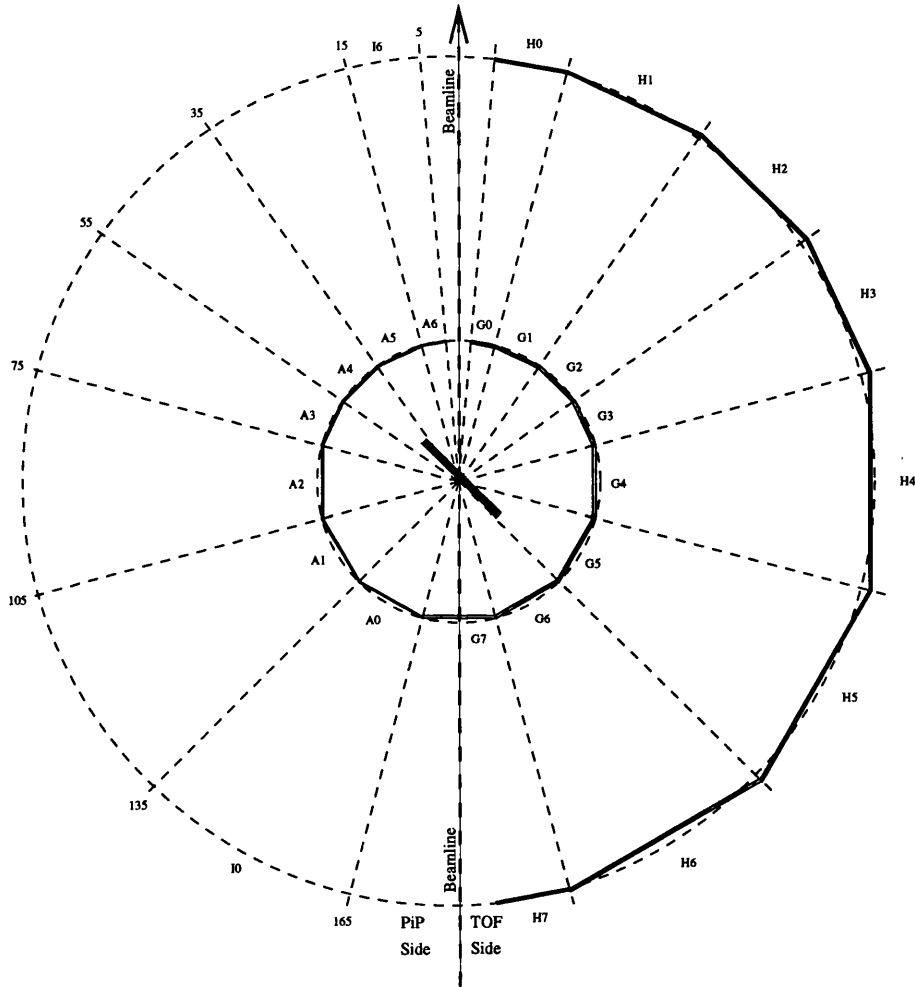


Figure 2.4: A schematic of the  $\Delta E$  Detector rings

The  $\Delta E$  rings (figure 2.4) are a series of thin plastic scintillators surrounding the target. The width of each element is chosen to produce counting rates of similar magnitude in each element and is therefore more highly segmented at forward angles where the flux of reaction products is higher.

The PiP side of the experiment is covered by a single ring which is centred on the target at a radius of  $\sim 11$  cm and comprises 7 elements (A0-A6 in figure 2.4).

These  $\Delta E_{start}$  detectors are used along with a coincident hit in PiP to identify events originating from the target. The proximity of  $\Delta E_{start}$  to the target means the timing information obtained for the detected particle is closely related to the time of the photoabsorption. The hit in a  $\Delta E_{start}$  element is thus used as a start signal for all the TDCs in the experimental system, giving a reference time from which correlated particles can be selected or flight times in the TOF system can be calculated.

The TOF side of the experiment is covered by two rings,  $\Delta E_{TOF1}$  and  $\Delta E_{TOF2}$  of radii  $\sim 11$  cm and  $\sim 30$  cm respectively. These are used for charge determination of detected TOF particles during subsequent offline analysis.

## 2.4.2 The PiP Detector

The PiP detector [47], shown schematically on figure 2.5, is a large solid angle ( $\sim 1$  sr) charged particle hodoscope, designed for the detection of protons or pions. For this work the detector is operated in proton mode. The detector comprises a segmented transmission layer ( $\Delta E_{PiP}$ ) in front of four E layers (E1-E4). The component elements are all manufactured from NE110 organic scintillator.

E layer	no of blocks	block L×D×H (cm)
E1	4	100 × 11.0 × 13.5
E2	4	130 × 17.5 × 17.5
E3	5	160 × 17.5 × 17.5
E4	6	190 × 17.5 × 17.5

Table 2.2: *Dimensions of the PiP E blocks*

The  $\Delta E_{PiP}$  layer is formed from four vertically mounted elements, each 2mm thick × 20cm wide × 42cm high which define the acceptance of the PiP detector. The scintillator bars in the E layers (table 2.2) have successively larger horizontal

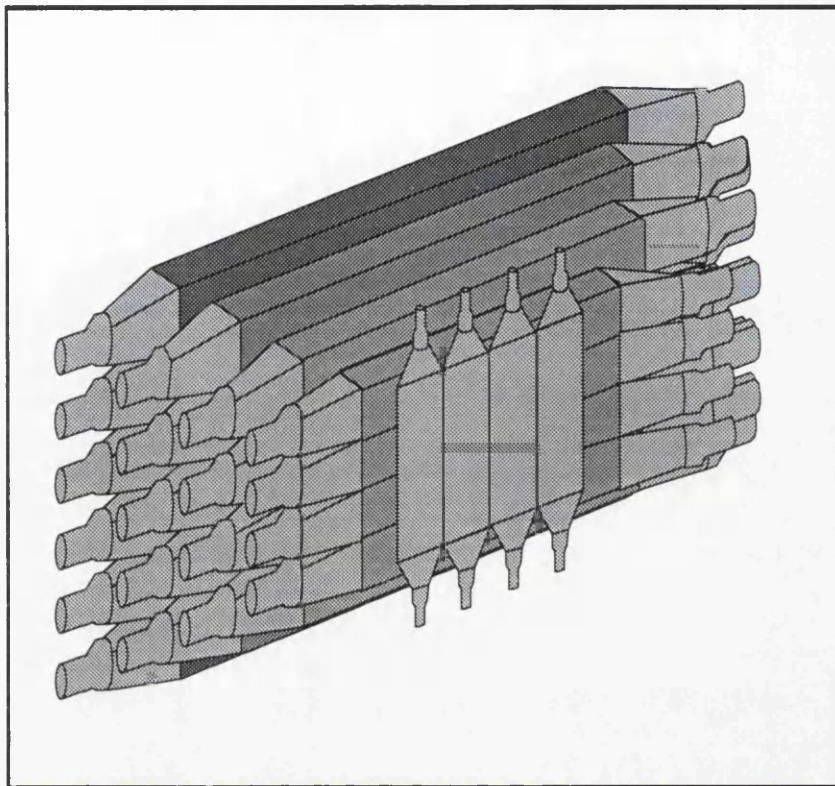


Figure 2.5: A schematic diagram of PiP

and vertical dimensions, to ensure that protons detected in the  $\Delta E_{PiP}$  layer do not subsequently leave through the edges of the detector. Photomultiplier (PM) tubes, of the EMI 9954KB type, are connected to both ends of each PiP scintillator element via light guides.

The whole PiP assembly is enclosed in a 5mm steel plate box which screens the scintillators from external light and temperature variations.

### 2.4.3 TOF detectors

The TOF detectors provide the opposite arm of the experiment and can be used for the detection of neutrons or protons. A schematic diagram of a TOF stand is shown as Fig 2.6.

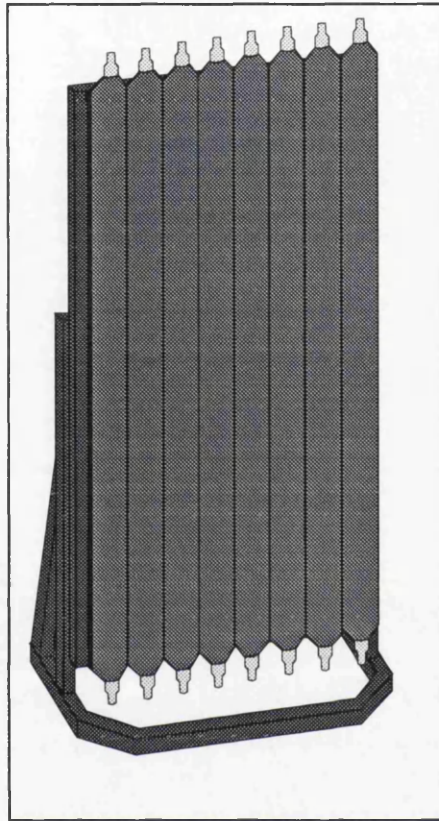


Figure 2.6: A schematic diagram of a TOF stand

Each of the bars making up a TOF stand are manufactured from NE110 scintillator of dimensions  $300 \times 20 \times 5 \text{ cm}^3$ . The bar thickness is chosen primarily to achieve the required neutron resolution. As the neutrons can interact at any depth in the scintillator the bars must be relatively thin to define an accurate neutron flight path. Each bar is viewed by Phillips XP 2312B PM tubes which are connected to each end via light guides. The timing of the PM signals from each end of the bar provides time of flight and vertical position information.

The entire TOF system comprises twelve stands of the type in figure 2.6. The stands can be positioned independently around the target to cover the required

kinematic regions. For this experiment the stands are positioned two deep to increase the efficiency for the detection of neutrons ( $\sim 5\%$  per TOF layer) without compromising the neutron resolution.

#### 2.4.4 Experimental Setup

The positioning of the detectors in the A2 hall at Mainz for this experiment is shown as figure 2.7. The PiP detector is placed in a backward angle position covering the polar angular range  $78^\circ$ - $158^\circ$ .

The TOF stands are positioned to sample a wide angular range of  $36.7^\circ$ - $142.0^\circ$ , with most detectors (G-L) positioned away from the back-to-back kinematics of a 2N process. The setup will therefore show more sensitivity to other processes and allow studies of the 2N process in extreme kinematics. The stands C-F do however sample the back-to-back kinematics and allow a direct comparison of cross sections outwith the 2N kinematics with the strength of the 2N process.

## 2.5 Data Acquisition

### 2.5.1 Information from events

Each scintillator element in the experimental setup provides both the pulse height and timing information of detected particles. The light deposited in a scintillator element is 'viewed' by two photomultiplier tubes which connect, via light guides, to each end. The electrical signal produced from each PM tube is fed to a fan-out module which splits the signal into two. One signal is fed to a Charge to Digital convertor (QDC) where the analogue pulse is converted to a digital signal. The second signal is fed to a leading edge discriminator which produces a logic pulse if the signal exceeds a preset threshold. The logic pulses are used to stop or start

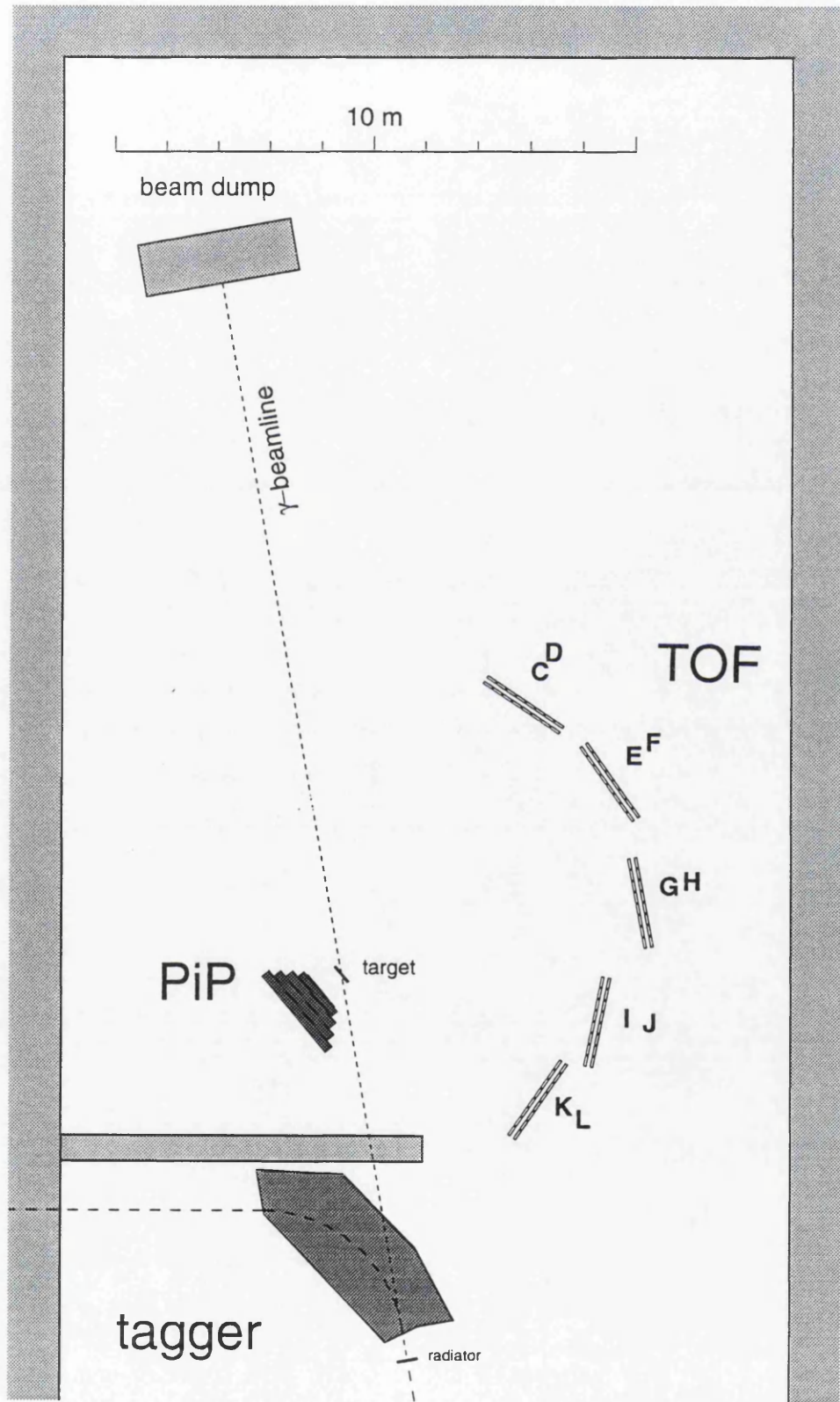


Figure 2.7: *The experimental layout*

a time to digital convertor (TDC) to record the timing information of the pulse. Both pieces of information are therefore converted to a digital format which can be read by the data acquisition system.

To cope with the large number of scintillators in the setup the QDCs are of the Phillips FASTBUS 10c2 type which are available in high density modules (32 channels), with read out threshold and fast clear capabilities. The TDCs are of the Phillips FASTBUS 10c6 type.

### 2.5.2 Trigger Logic

Many of the signals in the detectors are irrelevant to the measurement of the  $^{12}\text{C}(\gamma, 2N)$  or  $^{12}\text{C}(\gamma, 3N)$  cross sections. For the PiP detector these unwanted events comprise the detection of electrons from Compton scattering/pair production or protons without a coincident hit in TOF. The background of these events is large and so would take a large amount of CPU time to process and record. It is therefore important to have the means to quickly reject these background events during the experiment, to devote more CPU time to the proposed measurement.

For this purpose a trigger is set up to identify the events of interest for either the measurement or calibration purposes. These events comprise:

- Proton detected in PiP with corresponding particle(s) detected in TOF
- Cosmic ray event detected in PiP
- Photon in Pb glass detector

The cosmic events are used to calibrate and monitor the gain of the PiP detector and so are recorded throughout the experimental measurement. The Pb glass detector is only used on experimental runs to determine the tagging efficiency. During normal runs this detector is removed and its trigger deactivated.

The logic conditions to select each event type are entered into programmable CAMAC modules. The trigger logic is handled by Lecroy 4508 PLUs which can perform logic operations on any mixture of up to 8 inputs from various parts of the experimental setup. The trigger decision is split into two levels. These comprise a fast simple first level and a second level which comes later to enable inclusion of TOF/TAGGER information and make a more complex decision about the particle detected in PiP. At either of the stages the QDCs and TDCs can be cleared from the experiment and the detectors reset for the next event. The different trigger stages involved are discussed below.

### 2.5.3 First Level

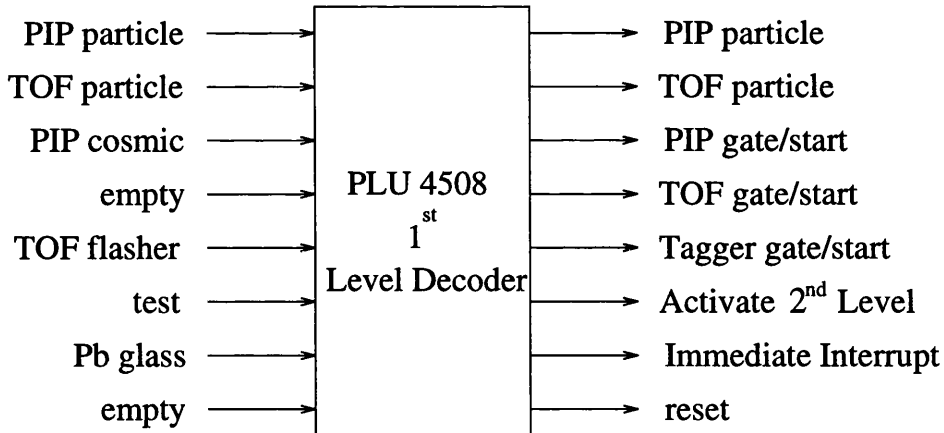


Figure 2.8: *The 1<sup>st</sup> Level, Fast Trigger*

The input/output arrangements of the first level trigger are illustrated in figure 2.8. When a signal is presented to any of the inputs of the decoder the PLU is latched so as not to receive any more signals while the decision is being made. The relevant triggers used in the data acquisition for this work are described below.

- **PiP Particle**

The PiP particle trigger is derived from a coincidence between the  $\Delta E_{start}$  and the  $\Delta E_{PiP}$  and E1 layers. This therefore represents the detection of a charged particle in PiP which has originated from the target. The particle could be any of proton, pion or electron.

The PiP particle trigger causes QDC gates and TDC start pulses to be generated but an interrupt is not sent to the acquisition computer at this stage. The second level trigger is activated which will use pulse height information to make a decision about the particle type before the event is stored.

- **PiP cosmic**

The cosmic trigger input is derived from a separate PLU which identifies a cosmic ray event in PiP by insisting that both the top and bottom block of a PiP E1, E2 or E3 layer fires. This selects events which pass near to the vertical through PiP, therefore making it unlikely that the event has originated from the target.

If a cosmic trigger is made then the PiP detector is provided with QDC and TDC gates and the acquisition computer is interrupted so that the event read out and recorded. The QDCs and TDCs are then cleared ready for the next event.

- **Pb glass**

A signal in the Pb glass input will result in the readout of its QDC and the Tagger focal plane being provided with TDC start pulses and gates. The event is then recorded by the acquisition computer before a QDC/TDC clear takes place.

### 2.5.4 Second Level

The input/output structure of the second level trigger is shown as figure 2.9. The second level trigger makes a more complex decision about the the particle detected in PiP and also checks for a corresponding TOF hit. The logic of the different 2nd level triggers are discussed below.

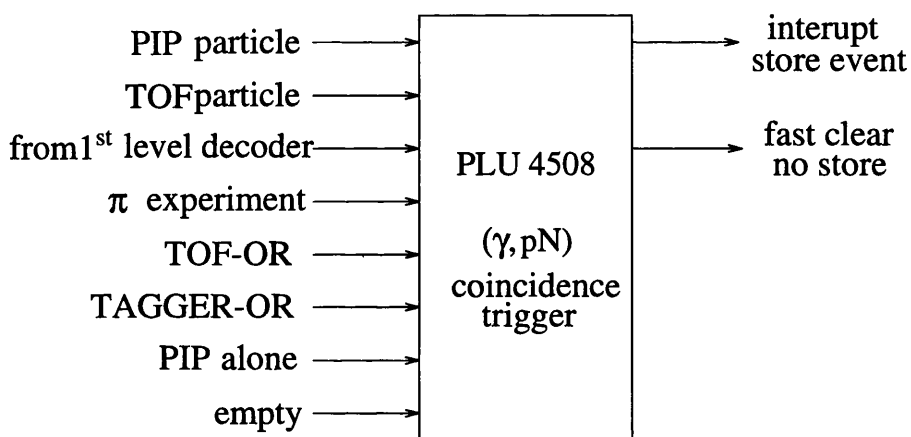


Figure 2.9: *The 2nd Level Trigger.*

- **Electron Reject**

It is particularly important not to record the large background of electrons detected in PiP. This is implemented using cuts on 2-Dimensional plots of the analogue sum of the pulse heights present in two consecutive PiP layers. Figure 2.10 shows a typical  $\Delta E$ -E plot for the pulse height in the  $\Delta E_{PiP}$  layer versus the sum of the pulse heights in the PiP E layers. The two ridges in the plot originate from the detection of protons and pions. Electrons leave small pulse heights in both layers and so would occupy the lower left corner of the plot. The electrons have been removed by the online cut which is implemented by insisting that the weighted analogue sum from

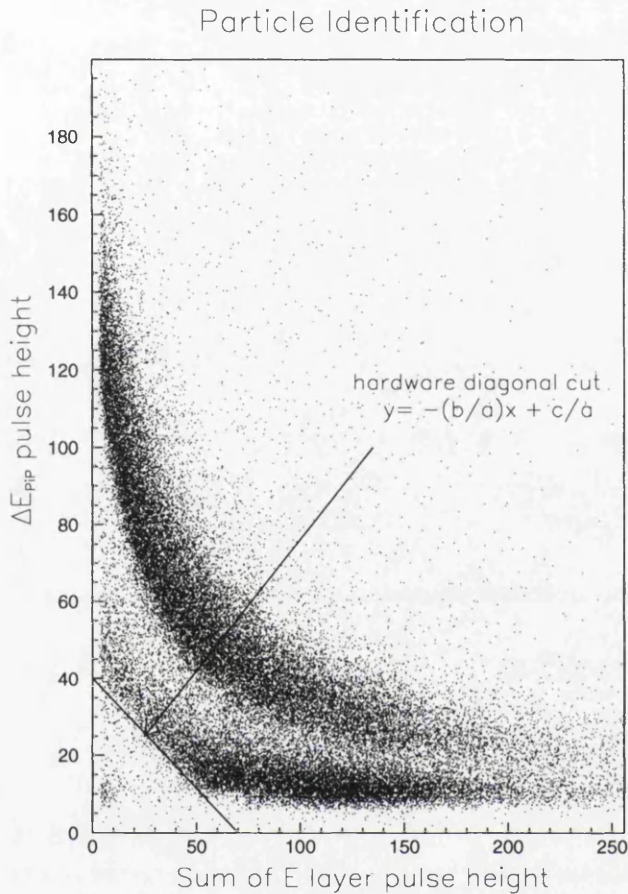


Figure 2.10: A plot  $\Delta E_{PiP}$  vs  $E$  plot indicating the particle identification.

the pulses in two chosen detector layers must exceed a fixed discriminator threshold of value  $c$ . This forms a diagonal cut on the plot with gradient  $-b/a$  where  $b$  and  $a$  are the weights (set by attenuators) applied to the analogue sum of each detector layer. The procedure is implemented for 3 layer combinations in total viz.  $\Delta E_{start}$  vs.  $E1$ ,  $\Delta E_{PiP}$  vs.  $E1$  and  $E1$  vs.  $E2$ . If an event makes the condition in any of the combinations the event is retained and no electron reject trigger is made. If a particle reaches the  $E3$  layer the results of the diagonal cuts are disregarded and the event is automatically retained to avoid the possibility of these high energy protons occurring below the cuts in previous layers due to foldback in the  $dE/E$  characteristics. The electron reject trigger is fed to the level 2 PLU which

clears the event if the particle did not meet the requirements.

- **TOF-OR**

This trigger brings in the TOF hit requirement by insisting on having at least one signal in a gated OR of all the 96 TOF bars. This trigger removes a large portion ( $\sim 90\%$ ) of events and therefore reduces the dead time considerably. The event in TOF must occur within  $\sim 400\text{ns}$  of the initial PiP trigger.

- **TAGGER-OR** The input to this trigger is fed from a gated OR of all 352 tagger elements. At least one electron must be detected in the focal plane within the PiP-TAGGER coincidence window ( $\sim 80\text{ns}$ ).

The remaining second level trigger inputs are used for either test purposes or for the use of the PiP detector in pion detection mode.

If both the TOF/TAGGER OR triggers are made and the electron reject trigger is not activated an interrupt signal is sent to the data acquisition computer and the event is stored. The setup is then cleared ready for the next event. If the electron reject is activated or one of the triggers is missing then the event is rejected and all QDCs and TDCs are fast cleared.

### 2.5.5 Data Acquisition

The acquisition system (ACQU) [48] runs on an Eltec E7 single board computer. The Eltec board is based on a Motorola 68040 chip which runs an OS9 operating system. The acquisition software controls the collection and data transfer of the event information from the FASTBUS and CAMAC modules. Upon receiving a trigger signal the digitised event is transferred using a shared I/O memory space for the E7 and the CAMAC/FASTBUS crate modules.

The acquisition process is controlled by a VAXstation situated outside the experimental hall. This is linked to the E7 computer via an ethernet TCP/ICP connection which allows the transfer of event information for storage and online analysis. Adjustments of the thresholds, PLU trigger conditions or target can all be done by remotely logging on to the E7 over the ethernet.

## **Chapter 3**

# **Detector Calibrations**

## 3.1 General Concepts

All the detectors in the PiP-TOF-TAGGER setup operate using a similar method. A charged particle passing through the detectors' constituent plastic scintillator ionises and excites molecules on or near its path. A fraction of this imparted energy will be released as light due to subsequent molecular de-excitation processes. Photo-multiplier (PM) tubes 'view' the light produced and convert this information into an amplified electrical pulse. The charge contained in the pulse is proportional to the number of incident photons at the face of the PM tube. Uncharged particles can be detected from scattering processes which result in secondary charged particles being produced in the scintillator.

A digital measurement of the charge contained in the output pulse from the PM tubes is obtained from charge-to-digital convertors (QDCs) which integrate the signal current. Time-to-digital convertors (TDCs) provide timing information which allows the differences in arrival times for particles at each detector to be determined. This raw timing and charge information is converted into meaningful physical variables using calibrations described in this chapter.

The common characteristics of the component QDCs, TDCs and scintillator material are initially discussed in general terms, with the specific calibrations for each detector described in detail in the later sections.

### 3.1.1 QDC Properties

The signal fed to the QDC from the photomultiplier tube contains an electrical charge  $Q$ . The QDC integrates this pulse over a period determined by the 'gate width', (which is set to be longer than the analogue pulse) and gives an output equal to  $Q$  plus an offset. The offset is referred to as the pedestal and arises as some DC leakage current is always present in the input signal. This must

therefore be subtracted to determine the true charge present in the input pulse, ie.

$$Q = QDC - pedestal \quad (3.1)$$

During normal data acquisition a software window is applied to avoid reading out QDCs with no signal above the pedestal. However the position of the pedestals can be obtained and monitored periodically from calibration runs in which the QDC readout window is removed.

### 3.1.2 TDC properties

The TDC is started (or stopped) once the the rising edge of the incoming signal exceeds the threshold set by a leading edge discriminator. The value of the threshold is chosen to eliminate the effects of electronic noise and can be determined from a plot of QDC spectra subject to the condition that the associated TDC fires (figure 3.1). The plot also shows the position of the pedestal (obtained from a different experimental run) relative to the threshold. For normal runs the QDC readout window is set at a value between the pedestal and threshold.

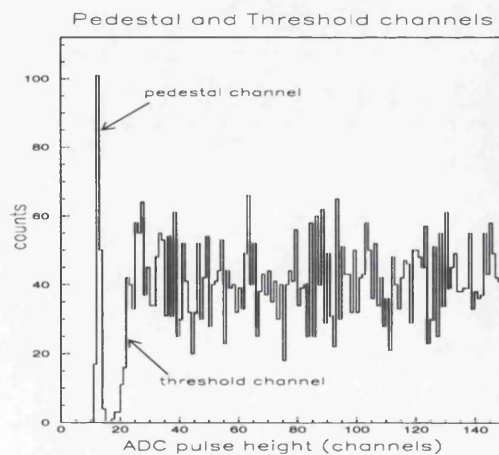


Figure 3.1: *Pedestal channel and discriminator threshold.*

### 3.1.3 Walk correcting the TDCs

As the discriminator is not fired immediately at the start of the pulse a small timing correction is needed to accommodate for the fact that a large pulse will reach the discriminator threshold slightly faster than a small pulse (figure 3.2). This effect is referred to as walk and can be corrected for using a parameterisation based on the work of Braunschweig [49].

$$T' = T + r - r\sqrt{\frac{a_0}{a}} \tag{3.2}$$

$T'$  and  $T$  are the corrected and uncorrected time values respectively, in TDC channels. The threshold,  $a_0$ , is obtained from the data as described previously. The rise time  $r$  is then chosen so that the corrected time ( $T'$ ) is independent of pulse height ( $a$ ).

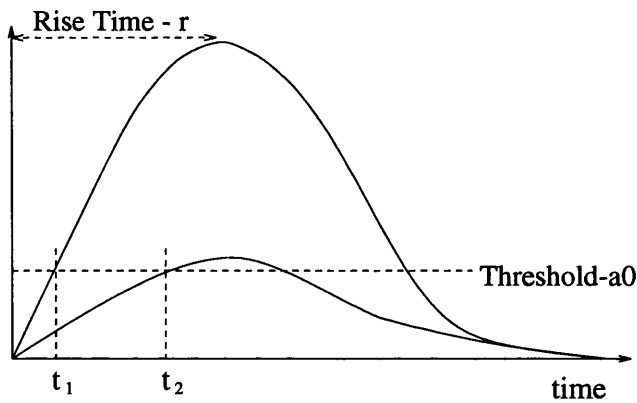


Figure 3.2: *The effect of 'Walk'*

## 3.2 General Detector Properties

### 3.2.1 Light Output

A particle incident on a scintillator bar in the detector system creates light which will propagate through the scintillator to be viewed by the PM tubes at either end. The light however is attenuated by the scintillator medium so the amount of light the PM tubes at each end of the bar receive depends on the position of entry of the particle.

Assuming an exponential attenuation of the light with decay constant  $K$  then for a particle entering the bar at a distance  $x$  from one end:

$$L_1 = \frac{L_{dep}}{2} e^{-\left(\frac{x}{K}\right)} \quad (3.3)$$

$$L_2 = \frac{L_{dep}}{2} e^{-\left(\frac{L-x}{K}\right)} \quad (3.4)$$

Where  $L_{dep}$  is that part of light generated in the scintillator which is captured into an internal reflection mode in the bar and  $L_1$ ,  $L_2$  is the amount of light received at each end of a bar of length  $L$ .

Taking the geometric mean of  $L_1$  and  $L_2$  produces a position independent quantity proportional to the amount of light initially deposited in the bar. ie

$$\sqrt{L_1 L_2} = \sqrt{e^{-\left(\frac{L}{K}\right)}} \frac{L_{dep}}{2} = const \times L_{dep} \quad (3.5)$$

Therefore the geometric mean of the charge contained in the PM tube signals at each end of a bar should also be position independent and proportional to the amount of light deposited in the scintillator:

$$QDC_{mean} = \sqrt{Q_1 Q_2} = const \times L_{dep} \quad (3.6)$$

where  $Q_1$  and  $Q_2$  are the charges present in the PM signals at each end of the bar.

However, experimentally the attenuation of the light in scintillator medium does not have the exact exponential characteristic assumed above and so the geometric mean retains a small residual position dependence, referred to as droop. This is corrected using a parabolic function of position, the parameters of which can be extracted from the experimental data.

### 3.2.2 Position

The hit position of the particle is determined from the difference in the arrival times of the light at each end of the detector bar ( $t_{diff}$ ).

$$t_{diff} = (T_2 - T_1) + k_{offset} \quad (3.7)$$

Where  $T_2$  and  $T_1$  are the walk corrected times from the TDCs at each end of the bar and  $k_{offset}$  reflects the cable delays in the system.

A linear calibration from  $t_{diff}$  (ns) to *position* (m) is obtained by comparison of the extremes of the  $t_{diff}$  spectra with the known scintillator dimensions.

$$position = k_1 + k_2 t_{diff} \quad (3.8)$$

### 3.2.3 Scintillator Response And Electron Equivalent Energy Units

The scintillation light created when a particle enters an organic scintillator does not have a completely linear relationship to the particle energy,  $E$ . This is because low energy particles tend to dissipate a larger fraction of their energy in the form of lattice vibrations and heat than those with higher energies [50].

The magnitude of this effect is seen in Fig 3.3 which shows the light output of NE102A scintillator as a function of particle energy for protons and electrons [51]. The response to protons is seen to deviate from a linear behaviour for energies below  $\sim 50$  MeV. The electron response however is effectively linear at this scale as it only deviates significantly for electron energies below  $\sim 0.1$  MeV.

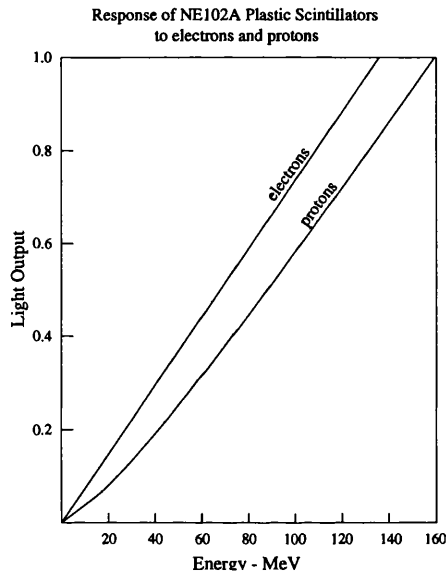


Figure 3.3: *Scintillator response to protons and electrons*

The response of the scintillator to protons can be linearised by expressing the proton energy in electron equivalent energy units ie. the electron energy which would produce the same amount of light in the scintillator as the proton.

These unit conversions are done using the parameterisations of the response functions by Madey et al [52].

### 3.2.4 Energy Loss Corrections

As the detectors are not positioned directly at the target then the energy losses incurred before a charged particle arrives at a detector must be corrected for. The air, scintillator wrappings and even the target itself will reduce the energy

of the detected particle.

To calculate each of the energy losses the range method was used. The particle range ( $R$ ) in a given medium can be parameterised by the expression:

$$R = aE^k \quad (3.9)$$

where the parameters  $a$  and  $k$  are both medium and particle dependent [54]. The difference in range for a particle of with energies  $E_1$  and  $E_2$  and corresponding ranges  $R_1$  and  $R_2$  is given by:

$$x = R_1 - R_2 \quad (3.10)$$

Rearranging the above two equations yields:

$$E_2 = \left[ E_1^k - \frac{x}{a} \right]^{\frac{1}{k}} \quad (3.11)$$

where  $E_1$  is the initial energy of the particle and  $E_2$  is the energy of the particle after passing through a medium of width  $x$ .

### 3.3 Start Detector

The start detector ( $\Delta E_{start}$ ) is part of a segmented ring of scintillator positioned around and close to the target. The  $\Delta E_{start}$  generates TDC start signals and gates for the PiP/TOF/Tagger system and so is central to the experimental setup. Timing signals derived from the  $\Delta E_{start}$  do not however give the precise timing of the photon interaction at the target. The small corrections necessary to account for this effect are discussed below.

As the start detector is not situated at the reaction vertex any timing derived from the  $\Delta E_{start}$  signal must be corrected for the flight time of the particle from the target ( $\Delta t_{flight}$ ). Corrections for the different cable lengths from each start

element to the TDC and also small variations in the physical distance of each element from the target must also be accounted for. Corrections for these effects are obtained from a TDC spectrum of one tagger element, made subject to the condition that a particular  $\Delta E_{start}$  element fired ( $\Delta t_{align}$ ). Finally the effect of walk at the discriminator of each TDC is removed ( $\Delta t_{walk}$ ) before calculating the total correction to the timing for the event ( $\Delta t_{start}$ ).

$$\Delta t_{start} = \Delta t_{flight} + \Delta t_{walk} + \Delta t_{align} \quad (3.12)$$

Application of this correction to the timing of the pulse in the  $\Delta E_{start}$ , allows the timing of the photo absorption to be calculated:

$$t_{reaction} = t_{start} - \Delta t_{start} \quad (3.13)$$

Plots of time from a tagger element TDC versus start detector pulse height both before and after correction are shown as Fig 3.4.

### 3.4 Tagger

The tagger provides energy and timing information on the residual electrons from the bremsstrahlung process. The energy is obtained from the position of the hit tagger element in the calibrated [55] focal plane. Each position corresponds to a certain energy bite ( $\sim 2$  MeV) of the residual electron.

Electron hits in the tagger which are correlated with signals in the reaction detectors form a well defined peak in each focal plane TDC. The resolution of this peak can be improved by applying the  $\Delta t_{start}$  correction to each tagger TDC event. Figure 3.5 shows this corrected coincidence spectra summed over all 352 aligned tagger elements. The flat background is due to electron hits which are uncorrelated with photons which caused the triggers.

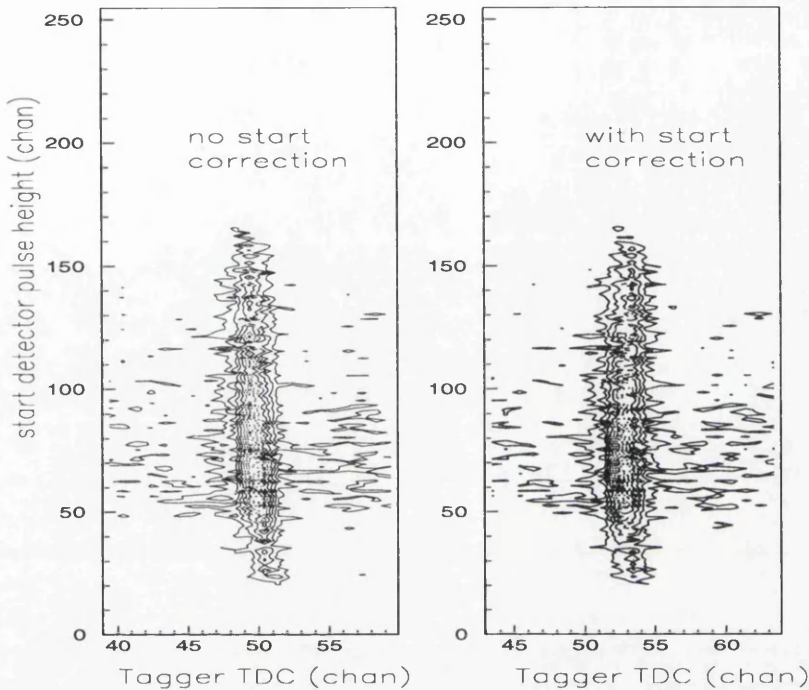


Figure 3.4: Application of the start correction to the  $\Delta E_{start}$

## 3.5 The PiP Detector

### 3.5.1 Walk Correction

The walk correction parameters (equation 3.2) for the PiP TDCs were taken from an experiment which ran immediately preceding this measurement [56].

### 3.5.2 Position Calibration

The position calibration for the E1, E2 and E3 layers is obtained from observing their  $t_{diff}$  spectra whilst noting which of the four  $\Delta E_{PiP}$  layer elements fire [15]. The intersection points of these four plots correspond to the position of the joins between the  $\Delta E_{PiP}$  elements. These occur in front of known positions on each E bar and thus the calibration coefficients of equation 3.8 can be found.

A procedure similar to the above is employed for the calibration of the  $\Delta E_{PiP}$

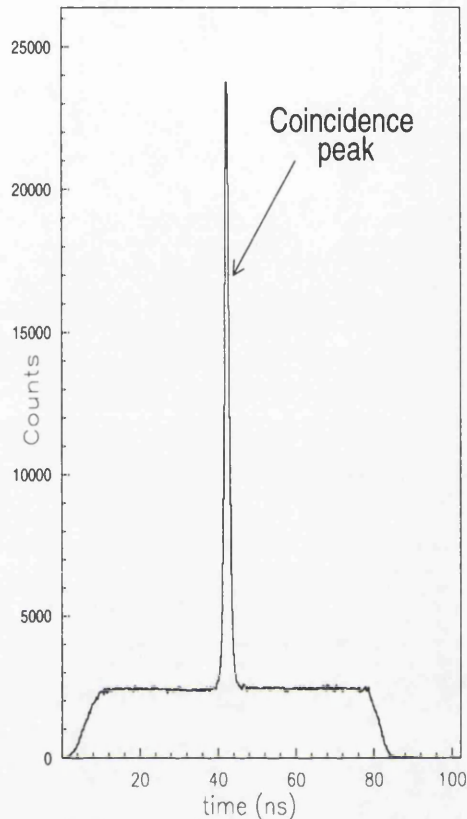


Figure 3.5: *Tagger time spectrum*

layer except the  $t_{diff}$  spectra for each  $\Delta E_{PiP}$  element are observed whilst noting which of the four E1 bars fire.

### 3.5.3 Gain Matching and Droop

The energy distribution of cosmic muons forms a Landau distribution, the centroid of which can be used to provide a standard energy reference for calibration purposes. To improve the resolution during the calibration the obtained  $QDC_{mean}$  is corrected to remove the effect of varying path lengths through a PiP bar for muons incident at different angles. The cosmic muon events are used to extract the parameters of the droop function [53] by observing the behaviour of the muon

centroid in the (path length corrected)  $QDC_{mean}$  spectra for successive 10mm segments along each PiP bar. This is illustrated on Figure 3.6 where the plot on the left shows the droop function obtained for a E2 layer block. The effect of droop can be seen to be  $\leq \sim 3\%$ .

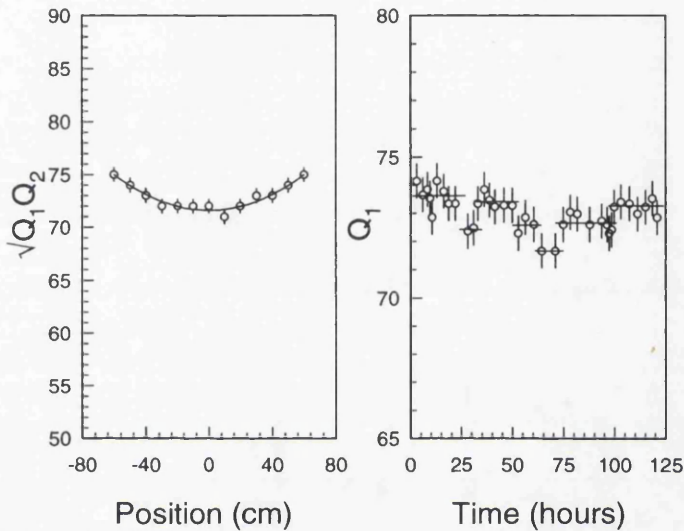


Figure 3.6: *Calibrating PiP using cosmic muons. The left figure shows the effect of droop whilst the right figure indicates the stability of a PiP PM tube gain with time.*

The PM tube gains are matched by observing the muon centroid position in the (path length and droop corrected)  $QDC_{mean}$  spectra for each PiP bar [57]. The PiP gain stability is illustrated on the right figure where the mean of the Landau distribution for a single E1 layer PM tube is plotted against time. The maximum variation in the gain of a PiP PM tube over the duration of the experiment was found to be  $\sim 5\%$ . Therefore for each PM tube the average gain over the experimental period was used in the analysis.

### 3.5.4 Energy Calibration

The total amount of light deposited by a proton in the PiP detector has a linear relation to the proton energy in electron equivalent energy units. The amount of light deposited is in turn proportional to the sum of the (gain matched and droop corrected)  $QDC_{mean}$  signals in PiP so therefore:

$$T_{p_{ee}} = constant \times Light = constant \times QDC_{mean} \quad (3.14)$$

where  $T_{p_{ee}}$  is the initial energy of the proton in electron equivalent energy units.

The calibration constant is obtained using data from experimental runs using a deuterated polythene target,  $CD_2$ . The kinematics of the two body  $D(\gamma,p)n$  reaction can be entirely determined from the photon energy and the angle of the detected proton. These two variables therefore allow determination of the energy of the proton at the target for each event. Energy losses are then calculated to find the corresponding energy (in electron equivalent units) at the front of PiP. A plot of the kinematically determined proton energy,  $T_p^{calc}$  ( $MeV_{ee}$ ), versus the sum of corrected  $QDC_{mean}$  in PiP gives a ridge from which the calibration constant in equation 3.14 can be obtained. Once found the constant allows the measured energy,  $T_p^{meas}$  ( $MeV_{ee}$ ), of each proton to be calculated.

Fig (3.7) shows a plot of  $T_p^{calc}$  versus  $T_p^{meas}$  after the calibration has been completed. Background carbon events have been removed as described in section 3.8.1.

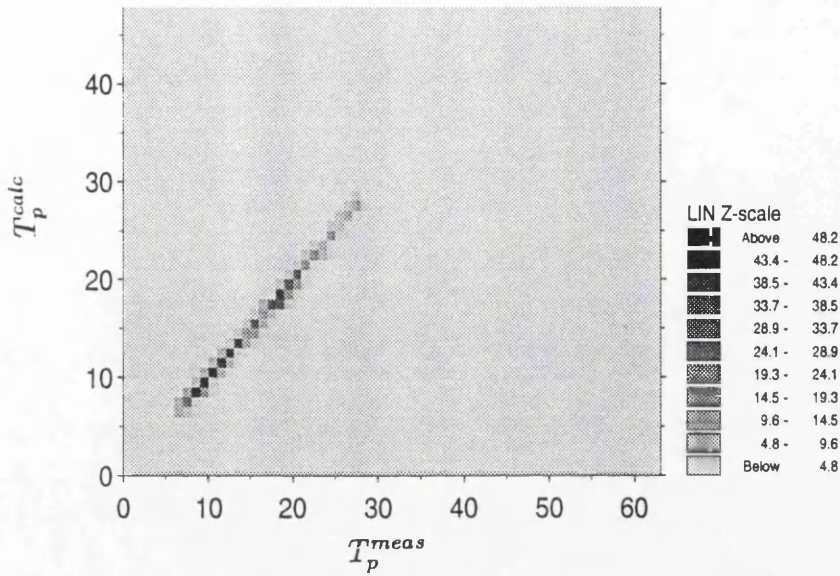


Figure 3.7: Calculated proton energy ( $MeV_{ee}$ ) vs Measured proton energy ( $MeV_{ee}$ ) for  $PiP$ .

## 3.6 The TOF Detectors

### 3.6.1 Walk Correction

The walk parameters for each TOF bar were obtained from a separate calibration run which employed the TOF flasher units [58]. A variable intensity light pulse from an LED was fed, via optical fibres, into each PM tube while simultaneously producing a TDC start trigger. The walk parameters for each bar were obtained by examining the variation of the TDC stop time as a function of the initial light intensity [59].

### 3.6.2 Position Calibration

The vertical position calibration is obtained from the (walk corrected)  $t_{diff}$  spectrum for each TOF bar, assuming the extremes of the distribution correspond to the ends of each bar (Fig 3.8). As each TOF bar is of known length (3m) the coefficients of equation 3.8 can be calculated.

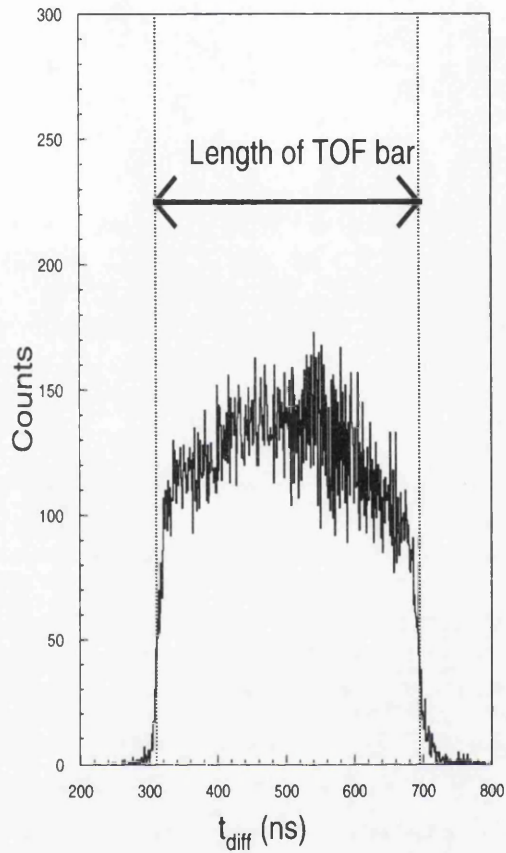


Figure 3.8: *TOF vertical position calibration*

The physical position of each TOF bar with reference to the target is determined accurately using an ultrasound measuring device. These measurements in conjunction with the vertical calibration allow the flight path and angular information of each detected particle to be extracted.

### 3.7 Energy calibration

A determination of the time of flight for the particle to travel from the target to TOF is necessary to obtain each particle's energy. The TOF timing is obtained from the walk and start (section 3.3) corrected  $TDC_{mean}$ . The corrected  $TDC_{mean}$  is equal to the particles' true time of flight,  $T_{tof}$ , within a constant. ie.

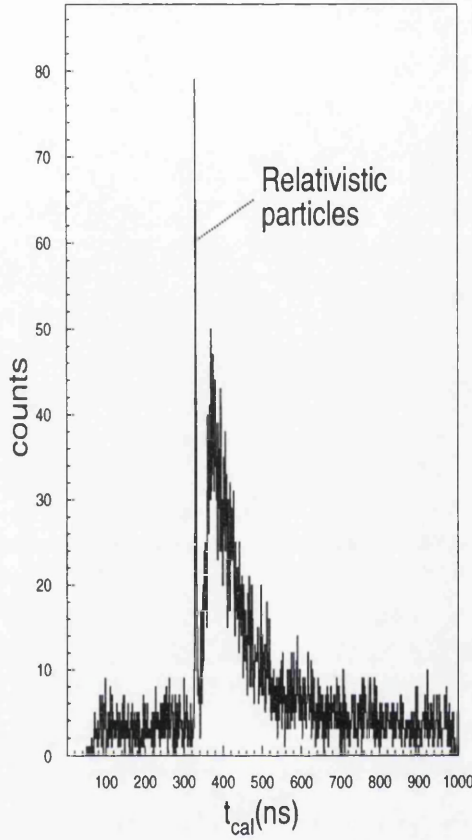


Figure 3.9: Determination of the  $t_{zero}$  from the gamma flash

$$T_{tof} = TDC_{mean} - t_{zero} \tag{3.15}$$

The constant is referred to as the  $t_{zero}$ . The  $t_{zero}$  offset arises from the delay between a particle entering a TOF bar and the subsequent firing of the TDCs. This is mainly due to the physical lengths of cable the pulses from the PM tubes must travel to reach the electronics and is different for each bar.

Relativistic particles have a known flight path and velocity ( $\sim c$ ) so a plot of  $t_{cal}$  given by:

$$t_{cal} = TDC_{mean} - \frac{flightpath}{c} \tag{3.16}$$

will have a ‘gamma flash’ peak occurring at the value of the  $t_{zero}$  constant. This is shown in Figure 3.9.

Once the time of flight of the particle is known then the energy can be calculated using the expression

$$T = m \left( \frac{1}{\sqrt{1 - \beta^2}} - 1 \right) MeV \quad (3.17)$$

where  $m$  is the rest mass of the particle and  $\beta = v/c$ ,  $v$  being calculated from the time of flight of the particle.

### 3.7.1 Gain Matching

TOF gains are matched to allow uniform application of energy thresholds and particle selection cuts to all the TOF bars in the setup.

The gains of all 96 TOF bars are matched by observing the ‘punch through’ energy for protons. This is the minimum amount of energy needed for the protons to go through and leave the back of a TOF bar ( $\sim 66 \text{ MeV}_{ee}$ ). The punch through point can be obtained from the position of the proton foldback on a plot of flight time per metre versus (droop corrected)  $QDC_{mean}$  (figure 3.10).

The gains are matched by ensuring that the foldback occurs at the same point in the 2-D spectrum for each TOF bar.

### 3.7.2 Replacement QDC Values

The TOF detectors have a large gain to optimise detection of neutrons. Neutrons are detected indirectly from the release of charged particles in the scintillator following neutron scattering reactions. These indirect events can leave relatively small pulses in the detector.

A proton event in TOF produces light more directly and therefore leaves a

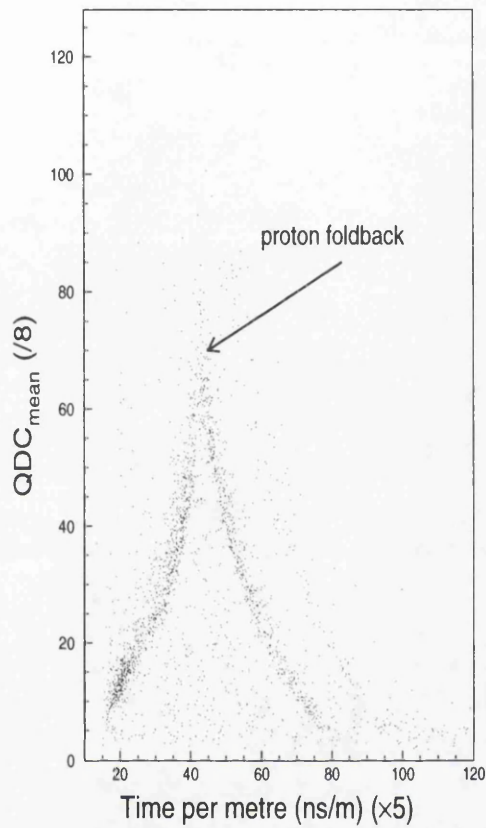


Figure 3.10: *Sail plot for a single TOF bar illustrating the position of the proton foldback at 66 MeV<sub>ee</sub>.*

larger signal. It is possible, for some proton events, to produce a signal which overflows one of the TOF QDC's. In this situation the QDC simply outputs a zero value, causing the corresponding  $QDC_{mean}$  value to be less than expected for a proton of that energy. As particles are distinguished in TOF using both time of flight and  $QDC_{mean}$  information the overflowed QDC value must be estimated or the event may be misidentified.

From equations 3.3, 3.4 the QDC signals at each end of a TOF bar can be estimated by:

$$a_1 = G_1 \frac{L_{dep}}{2} e^{-\left(\frac{x}{K}\right)} \quad (3.18)$$

$$a_2 = G_2 \frac{L_{dep}}{2} e^{-\left(\frac{x-l}{K}\right)} \quad (3.19)$$

where  $G_1$  and  $G_2$  are the gains of the two PM tubes. Assuming the gains are matched then the ratio of the two pulse heights can be expressed as:

$$\frac{a_1}{a_2} = e^{-\left(\frac{\frac{l}{2}-x}{\frac{l}{2}}\right)} \quad (3.20)$$

Taking logarithms and rearranging gives:

$$x = \left(\frac{-k}{2}\right) \log\left(\frac{a_1}{a_2}\right) + \frac{l}{2} \quad (3.21)$$

$$= \log\left(\frac{a_1}{a_2}\right) Ph0 + Ph1 \quad (3.22)$$

where  $Ph0 = \frac{-k}{2}$  and  $Ph1 = \frac{l}{2}$  are constants.

These constants can be extracted using events where both  $a_1$  and  $a_2$  are present in the data. For each good event the position,  $x$ , predicted by equation 3.22 can be compared with the position value obtained using the (walk corrected) TDC time difference ( $pos_{tdiff}$ ). The constants can then be adjusted until the values predicted by the two methods are consistent.

Plots of  $(x - pos_{tdiff})$  versus  $pos_{tdiff}$  for a typical TOF bar are shown both before and after calibration in figure 3.11. The distribution is centred about zero by altering  $Ph0$  and the gradient is adjusted to be horizontal by varying  $Ph1$ .

After calibration the constants obtained can be used in equation 3.20 to predict the signals that should have been present in the overflowed QDC's.

### 3.7.3 TOF Pulse Height Thresholds

A minimum  $QDC_{mean}$  software threshold is applied to each TOF event in the data. This is to both reduce the contribution of randoms, which predominantly leave low pulse heights in the detectors, and to remove any possible differences

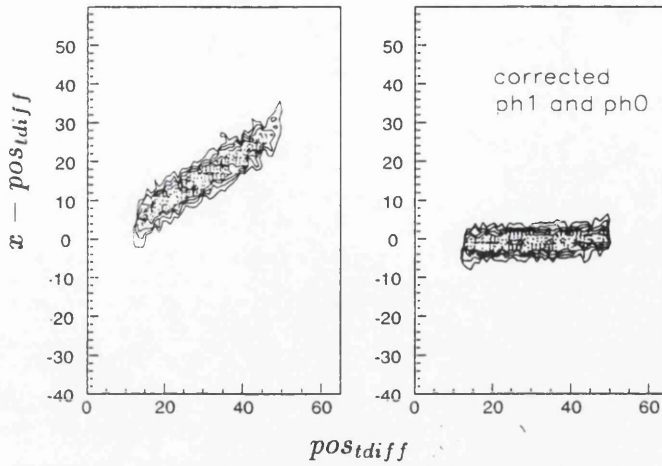


Figure 3.11: *Determining the parameters needed for the reconstruction of missing QDC's*

in the threshold for different bars in the TOF array. The value of the threshold in  $\text{MeV}_{ee}$  is required to allow a determination of the neutron detection efficiency to be made (section 4.6.3).

The applied  $QDC_{mean}$  threshold (channels) is related to energy ( $\text{MeV}_{ee}$ ) using two standard calibration points. The first is provided from data taken with an Am-Be source placed (sequentially) in front of each TOF stand. The source provides photons of known energy ( $4.2 \text{ MeV}_{ee}$ ) and so the observed (gain matched)  $QDC_{mean}$  can be related directly to energy. The second calibration point is obtained from the data using the  $QDC_{mean}$  value from the proton foldback position, occurring at  $66 \text{ MeV}_{ee}$  (section 3.7.1), where the proton leaves the back of a TOF bar.

From a linear plot using these two points and the origin the applied  $QDC_{mean}$  threshold was found to correspond to a particle energy (at the TOF bar) of  $9 \text{ MeV}_{ee}$ .

## 3.8 Detector Performance

The performance and calibration of the detectors in the PiP-TOF system is checked using the  $D(\gamma, pn)$  reaction. The kinematics of the two body reaction are fully determined, with only the photon energy and one of the particle angles needed to entirely define the final state. Comparison of measured and predicted values allows the energy and angular resolutions for the system to be evaluated.

### 3.8.1 Separating Deuterium Events

As a deuterated polythene target  $CD_2$  was used for these calibration runs some carbon background will always be evident in the data along with the deuterium events. To separate the two types of event the ‘Missing Energy’ can be calculated which in general is defined as:

$$E_{miss} = E_\gamma - T_p^{PiP} - T_n^{TOF} - T_{rec} = S_{NN} + E_x \quad (3.23)$$

where  $E_\gamma$  is the photon energy,  $T_p^{PiP}$  and  $T_n^{TOF}$  are the proton and neutron kinetic energies and  $T_{rec}$  is the kinetic energy of the recoiling system.  $S_{NN}$  is the separation energy of the 2 nucleons, which reflects the Q value for the reaction ( $S_{NN}=-Q$ ). As this is constant for a given reaction the missing energy gives a measure of the excitation energy of the residual system,  $E_x$ .

For the Deuterium events  $T_{rec}$  and  $E_x$  are equal to zero as the  $D(\gamma, pn)$  reaction has no recoiling system. Deuterium events will therefore form a peak in the missing energy distribution at 2.2 MeV ( $=-Q$ ). Figure 3.12 shows a missing energy plot (calculated assuming  $T_{rec} = 0$ ) for a  $CD_2$  target. Deuterium events can be clearly selected from this plot.

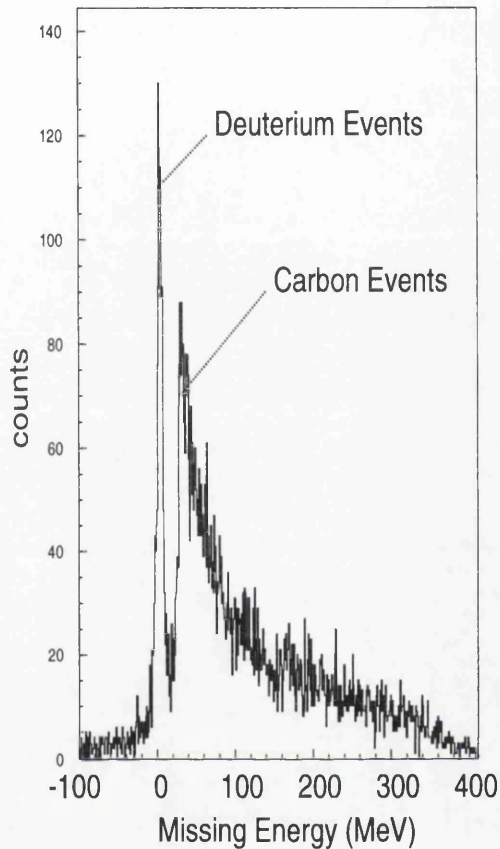


Figure 3.12: *Missing energy spectrum for  $CD_2(\gamma, pn)$ .*

### 3.8.2 Measured Detector Resolution

The detector resolutions are determined from a comparison of the predicted and measured values for the relevant variables. Predictions of the energy of both particles coming from a deuterium event can be obtained from the photon energy and the angular direction of one of the particles. The neutron angle is known to the greatest accuracy, so this variable is used with the photon energy to determine the entire kinematics of each event.

The average measured energy resolution for both PiP and TOF was found to be 5.5 MeV for  $E_\gamma=150-700$  MeV (fig 3.13). The average polar angular resolution of PiP was found to be  $4.5^\circ$  (fig 3.14).

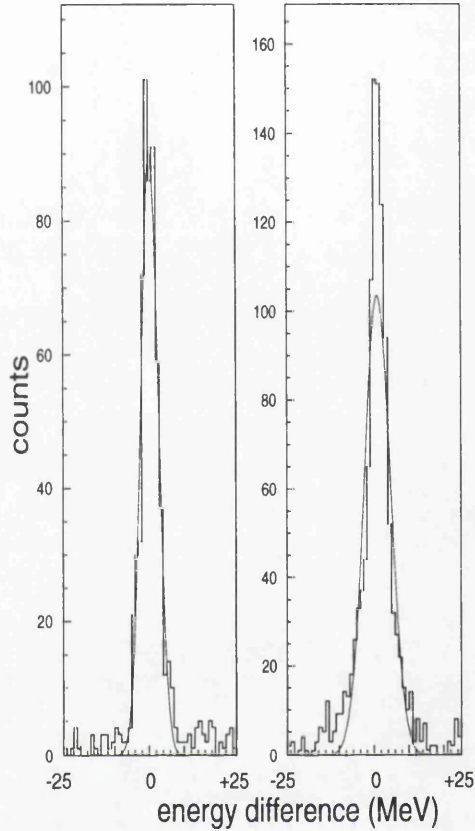


Figure 3.13: Average energy resolution for PiP (left) and TOF (right) for photon energies of 110MeV-700 MeV. The Gaussian fits give  $\sigma_{measured} (T_p) = 5.5 \text{ MeV}$  and  $\sigma_{measured} (T_n) = 5.5 \text{ MeV}$ .

### 3.8.3 Intrinsic Detector Resolution

The variables  $E_\gamma$  and  $\theta_n$  also have an associated error which consequently produces an uncertainty in all predicted values. This effect of this is unfolded to obtain the intrinsic resolution of a variable,  $\sigma_{intrinsic}$ , ie.

$$\sigma_{intrinsic} = \sqrt{\sigma_{measured}^2 - \sigma_{predicted}^2} \tag{3.24}$$

where  $\sigma_{measured}$  is the resolution of the variable when compared to the predicted value and  $\sigma_{predicted}$  is the error present in the predicted value itself.

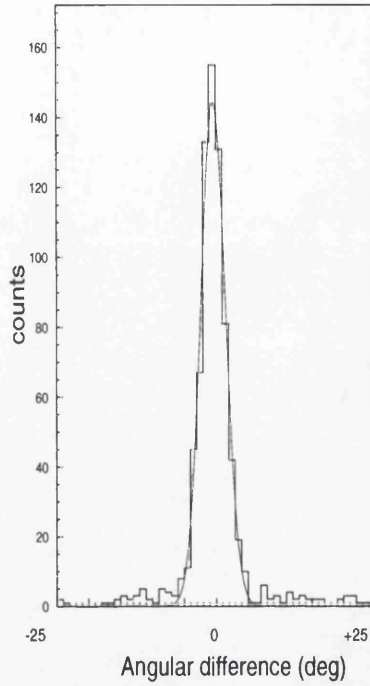


Figure 3.14: Average PIP angular resolution for photon energies of 110MeV-700MeV. The Gaussian fit gives  $\sigma_{measured}(\theta_p) = 4.5^\circ$

The error in  $E_\gamma$  is 2 MeV, determined from the width of each tagger element in the focal plane. The error in  $\theta_n$  is defined by the 20cm width of each TOF bar which, over an average flight path of 5m, corresponds to a resolution of  $\sim 2^\circ$ . The propagation of these errors onto the prediction of a variable  $x$  is given by:

$$\sigma_{predicted}^2(x) = \left[ \left( \frac{\partial x}{\partial E_\gamma} \right) \Delta E_\gamma \right]^2 + \left[ \left( \frac{\partial x}{\partial \theta_n} \right) \Delta \theta_n \right]^2 \quad (3.25)$$

This is used with the measured resolution in equation 3.24 to calculate the intrinsic resolution of the variable.

The overall resolution for the whole detector system is obtained from the width of the deuterium peak in the  $CD_2(\gamma, pn)$  missing energy spectrum. This was found to be 8 MeV (FWHM). The intrinsic energy and angle resolutions are summarised in table 3.1.

Detector	Particle	Quantity	Acceptance	Resolution(FWHM)
Tagger	$\gamma$	$E_\gamma$	110 MeV $\rightarrow$ 700 MeV	2 MeV
PIP	proton	$E_p$	31 MeV $\rightarrow$ 290 MeV	5.2 MeV
		$\theta_p$	78° $\rightarrow$ 153°	4.3°
TOF	neutron	$E_n$	$\geq 19.0$ MeV	5.2 MeV
		$\phi_n$	146.0° $\rightarrow$ 206.0°(max)	$\sim 1^\circ$
		$\theta_n$	36.7° $\rightarrow$ 142.0°	$\sim 2.0^\circ$
Combined		$E_{miss}$	-	8 MeV

Table 3.1: Summary of detector performance over the photon energy range 110 MeV-700 MeV.

# Chapter 4

## Data Analysis

Photons incident on a nucleus have an energy dependent probability of being removed from the flux, given by the total photoabsorption cross section  $\sigma^{ABS}(E_\gamma)$ . This cross section is a measure of the probability of a photoreaction occurring with any possible reaction mechanism producing any corresponding particles in the final state.

Analysis of reaction data involves separating this total cross section into different final state channels according to what is visible in the detectors. The present work concentrates on the  $(\gamma, 2N)$  and  $(\gamma, 3N)$  reaction channels which require methods of selecting both protons and neutrons in the final state.

Each measurement must be corrected for the effects of particle detector efficiencies and the contribution of random and background events to calculate the true yield. This, along with knowledge of the photon flux from the tagger, allows the visible cross sections to be calculated.

## 4.1 Proton Selection in PiP

The conventional method of selecting protons from a  $\Delta E$  vs  $E$  plot (figure 2.10) is not ideal as the positioning of the cut around the curved locus of protons is somewhat subjective. It is also difficult to distinguish and remove particles which have undergone inelastic reactions with the scintillator medium.

A more systematic approach using a range method of particle separation is employed for this work. For each proton or pion event the energy of the particle at the reaction vertex is determined in two ways.

- **Measured Energy**

The energy of the particle at the front of PiP is calculated from the total light produced (including corrections for energy lost in the dead layers).

The corresponding energy of the particle at the reaction vertex is then

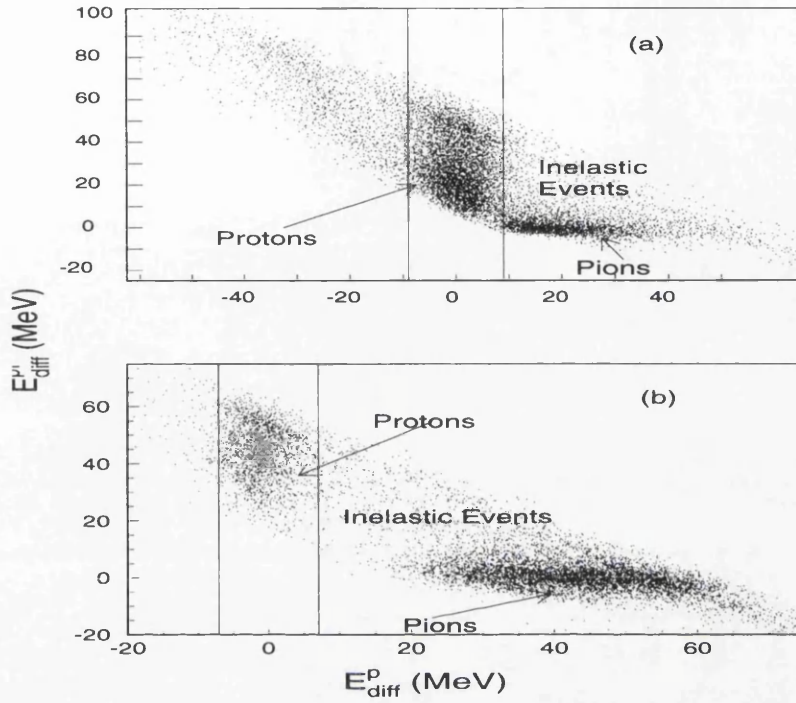


Figure 4.1: Plots of  $E_{diff}^{prot}$  versus  $-E_{diff}^{pi}$  for protons stopping in PiP layers E1 (top figure) and E2 (bottom figure)

calculated using the range method to take account of energy loss in the air,  $\Delta E$  detectors and the target. This gives  $E_{meas}$ .

- **Calculated Energy**

The calculated energy is obtained using only the light produced in the layer where the particle stopped. The vertex energy is then obtained by simply using the range method alone to calculate the energy losses of the particle back to the target. This gives  $E_{calc}$ .

The difference between the two quantities,  $E_{diff}$ , is calculated for each particle type, ie.

$$E_{diff}^p = E_{calc}^p - E_{meas}^p \quad (4.1)$$

$$E_{diff}^{pi} = E_{calc}^{pi} - E_{meas}^{pi} \quad (4.2)$$

Plots of  $E_{diff}^p$  versus  $-E_{diff}^{pi}$  are shown in Fig 4.1. Figure 4.1a show events where the proton stops in the E1 layer and fig 4.1b shows events where the proton stops in the E2 layer.

Protons can be seen to centre around  $E_{diff}^p \sim 0$  and pions around  $E_{diff}^{pi} \sim 0$ . The region containing events which have undergone inelastic reactions in the scintillator is also indicated on the plot. Simple vertical and horizontal cuts can be applied (figure 4.1) to separate unambiguously the protons used in the analysis from pions and events where protons have suffered inelastic losses.

## 4.2 Relevant $\Delta E_{TOF}$ Selection

The segmentation of the rings of TOF side scintillation detectors ( $\Delta E_{TOF1}$  and  $\Delta E_{TOF2}$ ) (figure 2.4) for this experiment allows the determination of the charge of each particle in TOF to be made on an event by event basis. This offers the advantage that multiparticle events in TOF can be separated and analysed according to their charge.

The charged/uncharged distinction of an individual TOF hit is determined from whether the appropriate  $\Delta E_{TOF}$  elements, lying on the path of the particle from the target, have fired. The relevant scintillator elements for each TOF bar are not found uniquely from considering the experimental geometry. The finite beam spot size at the target and also scattering of particles by the elements themselves can lead to particles firing TOF bars which are not on the straight line path from the target centre through a  $\Delta E_{TOF}$ .

The selection is therefore obtained from the data, using events having only one particle hit in the entire TOF array. The pattern of hits observed in the inner

$\Delta E_{TOF1}$  and outer  $\Delta E_{TOF2}$  rings for a hit in each individual TOF bar is used to extract the relevant elements on the path to the TOF bar. Each TOF bar was usually found to be fed by one  $\Delta E_{TOF1}$  (and corresponding  $\Delta E_{TOF2}$ ) element. However, TOF bars which covered polar angles near to the joins in the  $\Delta E_{TOF}$  ring required the inclusion of more elements.

For an event to be assigned as uncharged no ADC signal must be present in the relevant element(s) of the inner or outer  $\Delta E_{TOF}$  rings. Charged events are identified using the same information but requiring at least one TDC signal (ie at least one ADC signal above the TDC threshold) present in the relevant element(s) of both rings.

### 4.3 The Effect of Double TOF stands

The TOF stands used in this experiment are positioned in groups of two, placed directly behind each other (figure 2.7). This increases the efficiency for the detection of neutrons but also results in other effects which need to be accounted for.

- **Charged Particle Tracking Following Neutron Detection**

Neutrons incident on a TOF stand are detected when they release charged particles, mainly protons, in the scintillator. If this interaction takes place in a front stand there is a  $\sim 20\%$  chance that the scattered particle will go on to fire another TOF element in the second layer. Events of this type are identified by noting each uncharged hit in a front layer of TOF. A subsequent hit in the second layer in a bar either directly behind or immediately to the left or right of the front hit is assumed to come from a subsequent scattered particle. This hit in the second layer is then removed from the analysis.

- **Proton Detection**

Protons with sufficient energy can punch through the first layer of TOF detectors and leave a large enough signal to also fire an element of the second layer. If uncorrected this would cause double counting of high energy TOF events. Each charged hit in a front layer of TOF is therefore noted. A subsequent hit in the second layer, in a bar either immediately behind or to the left or right of the front hit, is assumed to originate from the same proton. The second layer timing information is ignored but the extra information available from the pulse height is retained. This is added to the front TOF bar to provide improved pulse height resolution and to optimise the proton/pion separation in the particle selection.

The energy of the proton is calculated from the time of flight obtained from the front layer hit.

### 4.3.1 Corrections for dead TOF bars

Four of the TOF bars used in the experiment were faulty and so are removed from the analysis completely. This causes different complications according to whether the dead bar is in a front or back layer and whether the particle is charged or uncharged. These corrections are discussed in Appendix A.

## 4.4 Neutron selection in TOF

Fig 4.2 shows a TOF bar  $TDC_{mean}$  spectrum for particles identified as being uncharged. The sharp peak is produced from the 'gamma flash' of electrons and photons produced in atomic scattering in the target. These events do not deposit enough energy to fire an ADC in the  $\Delta E_{TOF}$  layers and so are assumed

to be uncharged. These events are irrelevant to the present measurement and are rejected by the minimum prompt  $TDC_{mean}$  limit.

The maximum prompt  $TDC_{mean}$  limit is taken at a point where the number of counts does not exceed that of the random background. This cut can be quite loose as the effect of random events included in the 'prompt' region will be subtracted at a later stage.

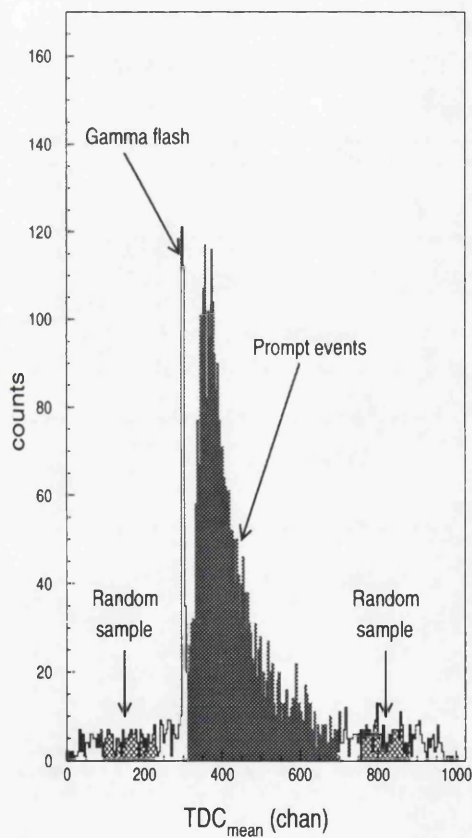


Figure 4.2: *Single TOF bar  $TDC_{mean}$  spectra for particles identified as being uncharged.*

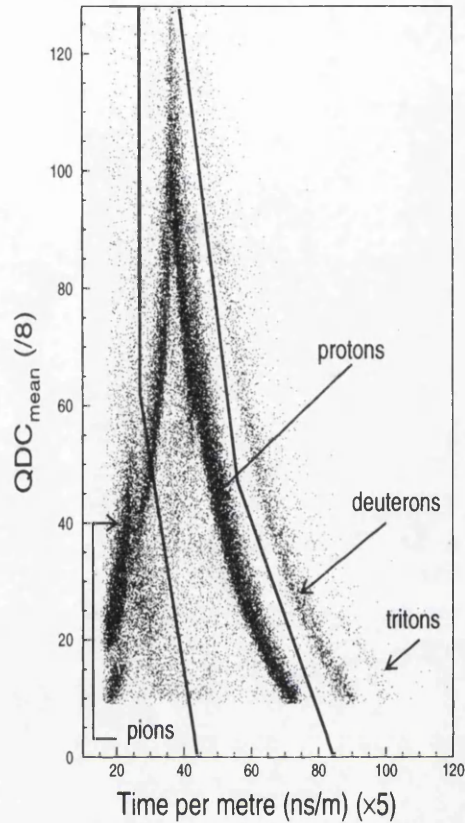


Figure 4.3: *Proton selection in TOF*

#### 4.4.1 Proton selection in TOF

A plot of flight time per metre versus total  $QDC_{mean}$  in TOF for charged particles is shown as Fig 4.3. The plot includes the  $QDC_{mean}$  addition for particles which fire both layers (section 4.3).

Protons, deuterons and pions give characteristic 'sail' loci on this plot. Heavier particles have a smaller velocity for the same energy so the loci occur from left to right in order of increasing particle mass. Pions deposit relatively small amounts of energy in the scintillator due to the effect of their relativistic velocities. The faint proton foldback (starting at  $QDC_{mean} \sim 60$ ) originates from protons which pass through (and are detected) in the front TOF layer without leaving a signal in

the back layer. The events constitute a small fraction ( $\leq 4\%$ ) of the total proton yield and are primarily due to the slightly larger solid angle coverage of the front TOF layers.

Protons are selected on an event by event basis using the software cuts indicated by the solid lines on the plot.

#### 4.4.2 Proton Energy loss corrections

The measured energy of the proton at TOF is basically a measure of the average energy of the particle over the flight path from the target to the detector. To obtain the kinetic energy of the proton at the target the energy losses in the target, air and scintillators are calculated using the range method [60].

### 4.5 The subtraction of random events

Random events are hits in any of the PIP, TOF or TAGGER scintillators which are not associated with the event which caused the trigger. As they are not correlated in time with the reaction the randoms form a flat continuous background on the TDC spectra.

The TDC readout gate is wide enough to record a sample of randoms away from the prompt correlated region. These events are analysed in the same way as the prompt events but are incremented in the final spectra with an appropriate negative weight factor. This removes the effect of random events occurring in the selected prompt region.

#### 4.5.1 Tagger randoms

Figure 4.4 is a (walk and start corrected) tagger timing spectrum showing the selection of prompt and random regions. An event which occurs in the (shaded)

prompt region is assigned a weight value of 1. Events occurring in the random regions are also analysed but with a negative weight factor which is scaled to account for the different widths of the prompt and random regions, ie.

$$\omega_{region}^{\gamma} = +1.0 \quad \text{PROMPT} \quad (4.3)$$

$$\omega_{region}^{\gamma} = \frac{-1.0 \times \Delta T_{prompt}}{\Delta T_{R1} + \Delta T_{R2} + \Delta T_{R3}} \quad \text{RANDOM} \quad (4.4)$$

where  $\Delta T_{prompt}$  is the width of the prompt region and  $\Delta T_{R1}$ ,  $\Delta T_{R2}$ ,  $\Delta T_{R3}$  are the respective widths of each of the three random regions.

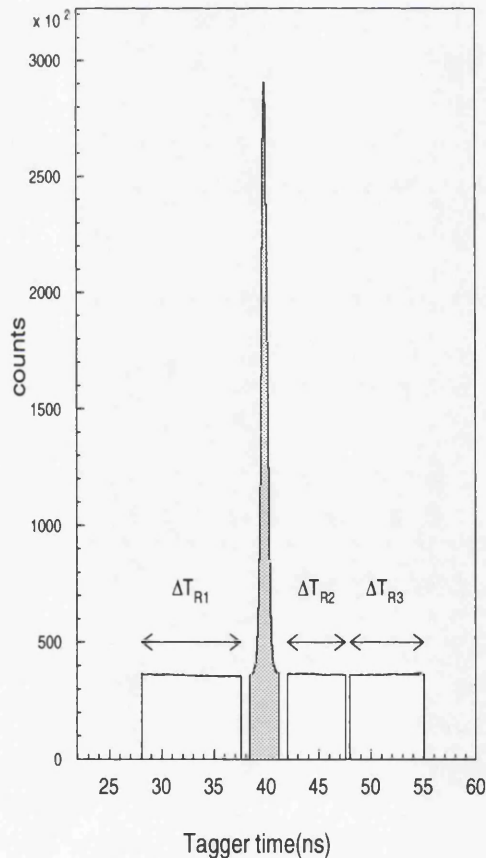


Figure 4.4: *Tagger randoms subtraction*

## 4.5.2 TOF randoms subtraction for uncharged events

- $(\gamma, 2N)$

A flat continuous random background is also present in the uncharged  $TDC_{mean}$  spectra for each TOF bar. The chosen prompt and random regions for the uncharged events are shown on Fig 4.2.

The sample of TOF randoms cannot be directly scaled and subtracted in a fashion similar to the Tagger case. This is as the maximum attainable width of the random region is always smaller than that of the prompt. Scaling the random samples and subtracting from the prompt would result in ‘graininess’ in the resultant spectra.

To avoid this a different approach is employed than described previously. Each event which occurs in a random region is subtracted in multiple with appropriate offsets to effectively create a random sample of comparable width to the prompt. This is achieved by firstly taking the measured  $TDC_{mean}$  of the observed random event and applying an offset to calculate what the value of the  $TDC_{mean}$  would be if the start of the random and prompt regions were coincident. ie. The left hand edge of the random region was coincident with the left hand edge of the prompt region. A series of pseudo events are then created with each successive  $TDC_{mean}$  being offset by a factor equal to the random region width, until the  $TDC_{mean}$  extends beyond the prompt region. Each of these pseudo events are analysed separately with a weight factor of  $-1/2$  to accommodate the fact that the process will be repeated for a second random region.

- $(\gamma, 3N)$

The above method of random subtraction is only employed for uncharged TOF events in the  $(\gamma, 2N)$  analysis. For the  $(\gamma, 3N)$  analysis no TOF

random subtraction is made. The total random contribution to the yield for each final charge state in the  $(\gamma, 3N)$  measurement is discussed in section 4.10.

### 4.5.3 TOF randoms subtraction for charged events

- $(\gamma, 2N)$

The contribution of randoms in the charged TOF channel is significantly smaller than the uncharged channel. This is due to both the higher detection efficiency for charged particles and the  $\Delta E_{TOF}$  hit requirement. The level of the contribution to the final yield can be estimated from the random region on figure 4.3. By sampling the events beyond the deuteron locus the random contribution is estimated to be  $\sim 1\%$  of the total proton yield and is therefore neglected.

- $(\gamma, 3N)$

Charged events in the  $(\gamma, 3N)$  analysis are also expected to have a small random contribution. The total random contribution to the yield for each final charge state is discussed in section 4.10.

## 4.6 Detector efficiencies

### 4.6.1 Tagging Efficiency

Tagging efficiency has been described previously in section 2.3.2. Figure 4.5 shows a plot of the measured tagging efficiency as a function of photon energy [61]. A slight energy dependence is observed due to the fact that the divergence of the photon beam decreases with increasing energy, allowing a larger portion of the flux to pass through the collimator.

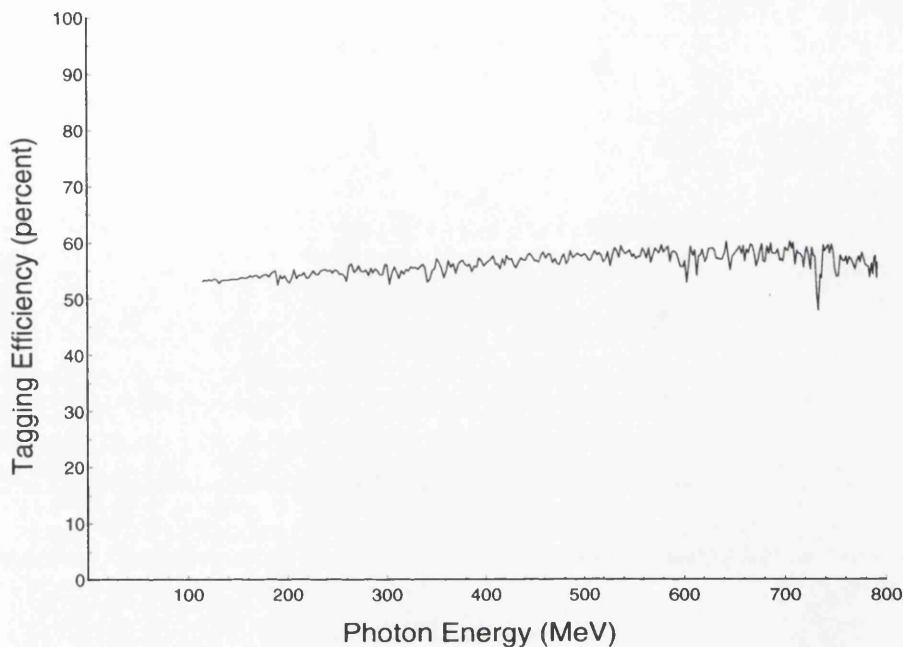


Figure 4.5: *Tagging Efficiency as a function of Photon energy*

### 4.6.2 Proton efficiency in PiP

The proton selection method, described in section 2.3.2, removes events which have undergone inelastic reactions in the scintillator. The remaining yield must therefore be weighted to account for the lost events. The weights are extracted from a GEANT [62] simulation of protons incident on the PiP detector. Figure 4.6 shows a plot of the obtained proton detection efficiency,  $\epsilon_{eff}^p$ , as a function of the incident proton energy.

Each PiP proton event is therefore given a weight:

$$\omega_{eff}^p = \frac{1}{\epsilon_{eff}^p} \quad (4.5)$$

### 4.6.3 Neutron efficiency

The detection of neutrons in TOF relies on neutron scattering reactions which produce charged particles in the final state. It is these charged particles, mainly

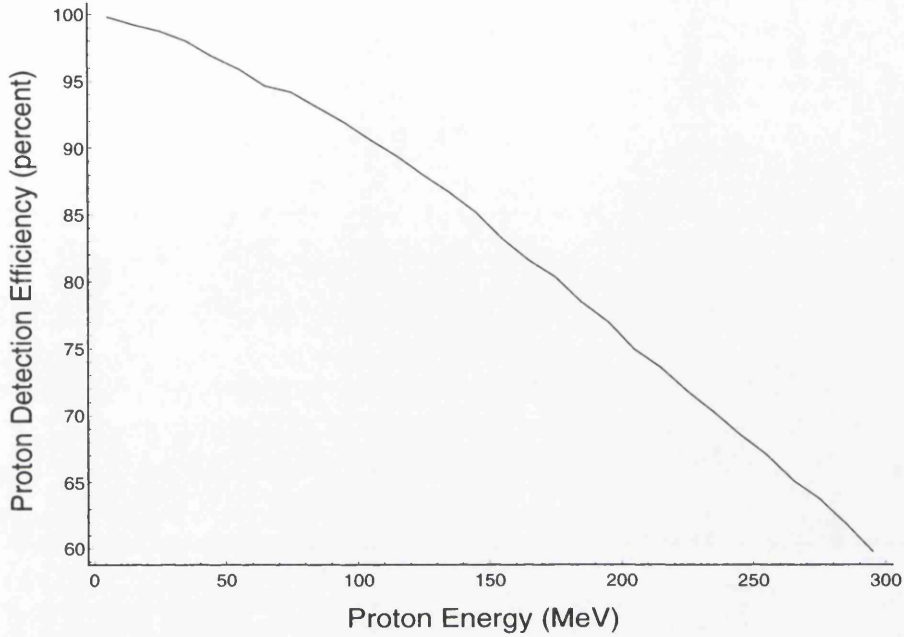


Figure 4.6: Proton efficiency as a function of proton energy, calculated using a GEANT [62] simulation

protons, that create the molecular excitations necessary to produce light. The TOF event is analysed if the value of the resultant  $QDC_{mean}$  exceeds the applied pulse height threshold, equivalent to  $9 \text{ MeV}_{ee}$ .

The neutron detection efficiency is determined using the STANTON [63] Monte Carlo code. This models the different possible neutron scattering reactions in the scintillator and predicts the resultant light produced. The predicted efficiency as a function of energy for neutrons incident perpendicular to a single 50mm thick TOF bar with a pulse height threshold of  $9 \text{ MeV}_{ee}$  is shown as Fig 4.7.

The effective thickness of a TOF bar however, is dependent on the neutrons angle of approach. The efficiency must therefore be modified to account for variations of path length in the scintillator, which gives  $\epsilon'_{bar}$

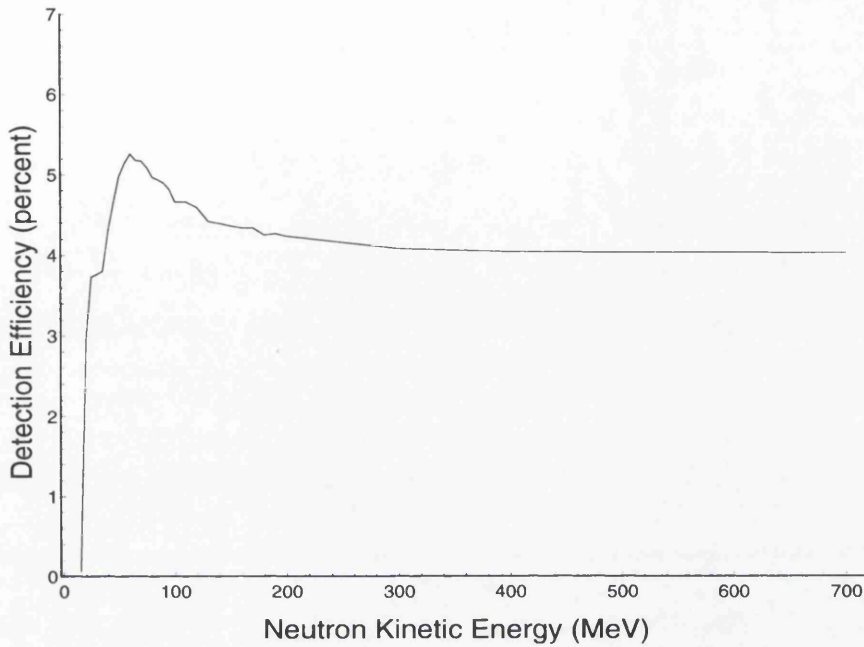


Figure 4.7: Neutron Efficiency as a function of Neutron energy for pulse height threshold of  $9 \text{ MeV}_{ee}$

$$\epsilon'_{bar} = \frac{\epsilon_{bar}}{\sin(\phi)} \quad (4.6)$$

Where  $\phi$  is the azimuthal angle of approach of the neutron.

The TOF detectors in the experiment consist of two layers of scintillator. The corrected efficiency of one bar must therefore be modified to predict the total efficiency for a detector two bars deep ( $\epsilon_{total}$ ) according to the relation:

$$\epsilon_{total} = \epsilon'_{bar} + \epsilon'_{bar}(1 - \epsilon'_{bar}) \quad (4.7)$$

This takes into account the fact that the neutrons detected in the first layer will be removed from the flux incident on the second layer.

Each neutron hit in TOF is therefore weighted by a factor  $\omega_{eff}^n$  where:

$$\omega_{eff}^n = \frac{1}{\epsilon_{total}} \quad (4.8)$$

## 4.7 Multiple Hits

Multiple hits can occur in any of the elements in the PiP-TOF-Tagger system. The multiple hits are analysed as subevents in the data analysis, with each subevent analysed separately in exactly the same way as a single hit event. The total number of subevents is given by the product of the multiplicities in each detector ie.

$$N_{subevent} = N_{PiP} \cdot N_{TOF} \cdot N_{Tagger} \quad (4.9)$$

- **Tagger subevents**

For each PiP trigger the tagger focal plane will usually contain more than one hit. Each of these is treated as a separate subevent with its appropriate energy and weight. For each hit a weight,  $\omega^{Tagger}$ , is calculated.

$$\omega^{tagger} = \frac{1}{x} \cdot \frac{1}{N_e(i)} \cdot \frac{1}{\epsilon_{tag}(i)} \cdot \omega_{region}^{\gamma} \quad (4.10)$$

$N_e(i)$  is the total number of electrons detected in the tagger channel (i). This factor unfolds the effect of the inherent bremsstrahlung distribution of the photon energies. The electron hits are related to the number of photons which reach the target by the tagging efficiency  $\epsilon_{tag}(i)$ . The number of tagger channels in the chosen photon energy range is given by  $x$  and is also divided out. Finally the weight  $\omega_{region}^{\gamma}$  is applied to the event to account for whether the tagger hit is in a prompt or a random region.

- **TOF subevents -  $(\gamma, 2N)$  analysis**

All uncharged hits in TOF are weighted to compensate for the neutron detection efficiency,  $\omega_{eff}^n$ . A minimum neutron energy threshold of 19 MeV

is applied to each uncharged event to avoid regions where the neutron efficiency  $\rightarrow 0$  (see figure 4.7). Different weights also apply according to whether the uncharged event originates from a prompt or random region of the  $TDC_{mean}$  spectrum. The weights applied to subevents in TOF are therefore:

$$\omega^{TOF} = \omega_{eff}^n \cdot \omega_{region}^n \quad UNCHARGED \quad (4.11)$$

$$\omega^{TOF} = 1.0 \quad CHARGED \quad (4.12)$$

Charged events in TOF are all given weight values of 1.

- **TOF subevents - ( $\gamma, 3N$ ) analysis**

As the ratio of three particle to two particle hits in TOF was found to be  $\leq 5\%$  for all channels the contribution of these subevents was neglected to simplify the analysis. These events were analysed using the two most forward angled TOF hits, which make the required final charge state, and neglecting the third. The effect of this approximation to the final yield is included in the quoted systematic error.

As no TOF random subtraction is made for the ( $\gamma, 3N$ ) analysis each neutron is weighted only for the detection efficiency (ie.  $\omega_{region}^n = 1$  for all events). As in the ( $\gamma, 2N$ ) analysis the minimum neutron energy requirement of 19 MeV is applied to each uncharged event.

- **PiP subevents**

Only single hit events are analysed in PiP. This is as the detector is not highly segmented which leads to difficulties when attempting to analyse

multiple hits. Each single proton hit is weighted in the analysis to account for the reduction in yield due to hadronic reaction losses in the scintillator.

$$\omega^{PiP} = \omega_{eff}^p \quad (4.13)$$

The total combined weight applied to each subevent is given by:

$$\omega^{subevent} = \omega^{Tagger} \cdot \omega^{TOF} \cdot \omega^{PiP} \quad (4.14)$$

## 4.8 Background Subtractions

A proportion of the recorded events will not come from photon absorption in the target but from reactions with the nuclei in the surrounding air. This contribution can be evaluated using data from runs where the target is removed. The target out data is analysed in exactly the same way as that with the target present. The resultant spectra can then be subtracted directly from the target in spectra.

The average contribution of background events to the yield was found to be  $\sim 4.5\%$ .

## 4.9 Derivation Of The Cross Section

The observed yield from any particular reaction channel, after correction by the weighting factors described previously, is simply related to the cross section  $\sigma$ .

$$Yield = n_{target} \sigma \quad (4.15)$$

Where  $n_{target}$  is number of target nuclei per unit area.

$$n_{target} = N_A \cdot \rho_n / A \quad (4.16)$$

with  $\rho_n$  being the target mass per unit area normal to the photon beam,  $N_A$  is Avagadro's number and  $A$  is the atomic number of the target nucleus.

As the target is placed at a known angle,  $\theta$ , to the photon beam  $\rho_n$  can be related to the measured density,  $\rho$ , by:

$$\rho_n = \frac{\rho}{\sin\theta} \quad (4.17)$$

## 4.10 Statistical Uncertainties

The calculation of the statistical errors of any histogrammed result must take into account the weight analysis used to obtain it. For each histogram bin the total contents,  $W$ , is the sum of the weights for all the events not the number of events themselves.

$$W = \sum_{i=1}^N \omega_i^{subevent} \quad (4.18)$$

Where  $\omega_i^{subevent}$  represents the weight of each subevent and  $N$  is the total number of subevents. The associated statistical error,  $\sigma_W$ , is given by:

$$\sigma_W = \sqrt{\sum_{i=1}^N (\omega_i^{subevent})^2} \quad (4.19)$$

For the case where all weights are equal to one the statistical error can be seen to reduce to the more familiar  $\sqrt{N}$  relation.

## 4.11 Systematic Uncertainties

The sources of systematic error present in the measurement of the  $(\gamma, 2N)$  and  $(\gamma, 3N)$  cross sections are each discussed below.

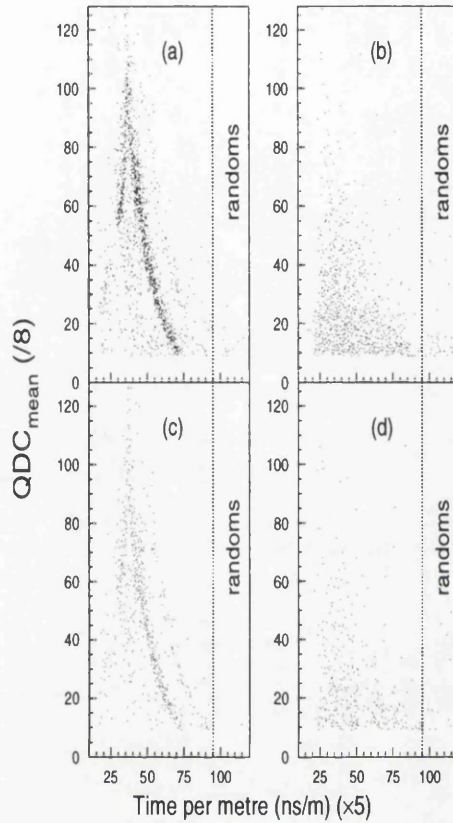


Figure 4.8: *Sail plots illustrating the level of TOF random contamination in the  $(\gamma, 3N)$  yield. The proton and neutron spectra for the  $(\gamma, ppn)$  yield are separated and shown in (a) and (b) respectively. The proton/neutron yields from the  $(\gamma, ppp)/(\gamma, pnn)$  channels are shown in figures (c) and (d).*

- **Tagging Efficiency** - Uncertainties in the tagging efficiency measurement arise from the statistical fluctuations in the value obtained for each tagger channel. The average uncertainty over the range of photon energies used in the experiment was found to be  $\sim 1.5\%$ .
- **Proton Efficiency** - Systematic errors in the proton efficiency occur due to the uncertainties in the removal of the hadronic loss events. Separating the hadronic loss events from the proton events introduces an estimated

systematic uncertainty of  $\sim 2.5\%$ .

- **Neutron Efficiency** - The authors of the STANTON Monte Carlo code quote an uncertainty of  $\sim 5\%$  in the predicted neutron efficiency.
- **TOF Particle Selection** - A systematic uncertainty occurs due to some contamination of charged events in the neutron channel. This uncertainty is estimated to be  $\leq \sim 5\%$ . The contamination of neutrons in the proton channel is negligible due to the low efficiency for the detection of neutrons. This can be seen in figure 4.3 where little strength is observed below the proton locus.
- **Target Density** - Systematic errors occur in the weighing and measuring of the graphite target as well as in the determination of the target angle with respect to the beam. The uncertainty in the target angle is reduced by employing a computer controlled stepping motor. All these contributions are estimated to contribute to the uncertainty at a  $\leq 1\%$  level.
- **TOF randoms for  $(\gamma, 3N)$**  - No TOF random subtraction was made for the  $(\gamma, 3N)$  data due to the more complicated  $3N$  final state. Although this means the analysis is less detailed the random contamination can be estimated from the yield occurring in the 'sail plot' spectra beyond the prompt particle region for each particle detected in TOF. Conditions are applied as for the final cross section except the maximum time per metre cuts have been removed to allow random events to be observed in the spectra. For protons this requires the removal of the proton/deuteron cut (figure 4.3) and for neutrons removing the 19 MeV minimum energy requirement.

A sail plot for events comprising the three final charge states are shown on figure 4.8 for  $E_\gamma = 150-700$  MeV. Figures 4.8a and 4.8b show the sail

plot spectra from the  $^{12}\text{C}(\gamma, ppn)$  yield, for the (TOF detected) proton and neutron respectively. The random contribution to the proton channel can be seen to be small accounting for  $\sim \leq 1\%$  of the prompt region. The neutron channel, as expected, shows larger contamination from randoms at the  $\sim \leq 10\%$  level. This relatively low level of contamination is achieved due to the application of the  $QDC_{mean}$  threshold, which reduced the contribution of randoms to the neutron channel by a factor of  $\sim 4$ .

Figure 4.8c shows the sail plot spectra for the protons comprising the  $^{12}\text{C}(\gamma, ppp)$  yield illustrating the low random contamination of  $\sim 2\%$ . As expected the  $^{12}\text{C}(\gamma, pnn)$  channel (figure 4.8d) shows the largest influence from random events, although the  $QDC_{mean}$  threshold reduces their contribution by a factor of  $\sim 5$  to  $\sim 14\%$ .

- **Rejection of  $(\gamma, 4N)$  events** - For the  $(\gamma, 3N)$  analysis the small percentage of 4N events ( $\leq 5\%$ ) were analysed as 3N events, by taking the two most forward angled TOF particles which gave an event with the required final charge state. This will create an uncertainty in the yield for all the  $(\gamma, 3N)$  channels of  $\leq \sim 10\%$  due to the two possible subevents removed from the analysis.

The systematic uncertainties in the  $(\gamma, pp)$  and  $(\gamma, pn)$  measurements are therefore estimated to be  $\sim 4\%$  and  $\sim 8\%$  respectively. The  $(\gamma, ppp)$ ,  $(\gamma, ppn)$  and  $(\gamma, pnn)$  cross sections are estimated to have higher uncertainties of  $\sim 11\%$ ,  $\sim 17\%$  and  $\sim 20\%$  respectively.

# **Chapter 5**

## **Results and Discussion**

The experimental results are presented in the form of ‘visible’ cross sections ( $\sigma^{vis}$ ) defined simply as the portion of the cross section which is visible in the PiP/TOF detectors, covering solid angles of  $\sim 1.1$  sr and  $\sim 0.79$  sr respectively. A direct comparison of the data with theoretical models can be made by filtering the results of the calculations through a simulation of the detector setup, which includes the angular acceptances and thresholds of each detector. Although the visible cross section does not give a measure of the total cross section it avoids the need for model dependent extrapolations into regions of phase space not covered by the detectors.

The measured  $(\gamma, 2N)$  and  $(\gamma, 3N)$  visible cross sections are presented after separation into their different final charge states. Experimentally a proton must be detected in PiP to make the trigger so this allows the  $(\gamma, pn)$ ,  $(\gamma, pp)$ ,  $(\gamma, ppn)$ ,  $(\gamma, ppp)$  and  $(\gamma, pnn)$  reactions to be studied independently and compared with theoretical predictions.

## 5.1 The $(\gamma, 2N)$ Reactions

The data obtained for the  $(\gamma, 2N)$  reactions are separated into two kinematic regions according to the polar angle of the TOF particle ( $\theta_{TOF}$ ). The first region  $\theta_{TOF} = 36.7^\circ - 71^\circ$  (corresponding to stands C-F on figure 2.7), covers a region of the phase space which includes ‘quasi-deuteron kinematics’ ie. those TOF angles corresponding in two body kinematics to proton angles covered by PiP. This is referred to as the ‘quasi-deuteron’ region (QD). The second region, covering  $\theta_{TOF} = 78^\circ - 142^\circ$ , samples phase space away from QD kinematics and is referred to as the ‘NON Quasi-Deuteron’ region (NQD).

The  $(\gamma, 2N)$  cross sections are presented as a function of variables which might be expected to show sensitivity to different underlying reaction mechanisms. The

excitation of the residual system after the interaction is indicated by the missing energy ( $E_m$ )

$$E_m = E_\gamma - T_{N1}^{PiP} - T_{N2}^{TOF} - T_{rec} \quad (5.1)$$

where  $E_\gamma$  is the incident photon energy and  $T_{N1}^{PiP}$  and  $T_{N2}^{TOF}$  are the energies of the two detected nucleons.  $T_{rec}$  is the energy the recoiling ( $A-2$ ) system must have to balance the (measured) photon and nucleon momenta. This is calculated from the momentum balance of the reaction (see equation 5.3 below). Due to the large mass of the recoil it corresponds to (typically) small kinetic energies. ie. a few MeV or less.

The missing energy describes the amount of energy which is not measured or accounted for by the known final state. For a direct 2N emission reaction the missing energy will be determined by the separation energy of the 2 nucleons ( $S_{NN}$ ) plus any excitation of the residual nucleus ( $E_x$ ):

$$E_m = S_{NN} + E_x \quad (5.2)$$

Processes which involve more than two nucleons or FSI processes will generally populate regions of high  $E_m$ .

The missing momentum ( $\mathbf{P}_m$ ) is calculated simply from the momentum of the photon and the two detected nucleons.

$$\mathbf{P}_m = \mathbf{P}_\gamma - \mathbf{P}_{N1} - \mathbf{P}_{N2} \quad (5.3)$$

For a direct 2N emission process the obtained missing momentum gives a direct measurement of the momentum of the recoiling nucleus. Assuming the residual nucleus is a spectator to the reaction its momentum can be related to the initial momentum ( $\mathbf{P}$ ) of the nucleon pair ( $-\mathbf{P}_m = \mathbf{P}$ ). Any FSI or additional particles

involved in the reaction will generally result in more momenta being given to the recoiling system with consequently larger values of  $P_m$ .

The direction that the recoiling system must have to balance the photon and nucleon momenta is also derived ( $\theta_{rec}$ ). As the beam is unpolarised the  $\phi_{rec}$  variable is not expected to give any information about the physics of the reaction. For a direct 2N emission process  $\theta_{rec}$  reflects the direction of the nucleon pair ( $\theta_{pair}$ ) at the time of the interaction. ( $-\theta_{rec} = \theta_{pair}$ ) and is expected to have an isotropic distribution. Processes which involve more than two particles or FSI will alter the distribution of  $\theta_{rec}$ .

## 5.2 Comparisons with the Valencia model

The Valencia model (VM) developed by Carrasco, Oset *et al.* [40] gives a comprehensive comparison with the data as it predicts the contributions of all the main reaction mechanisms which contribute to the  $(\gamma, 2N)$  cross section. Taking advantage of the Monte Carlo structure of the VM its predictions are easily separated into components according to the different initial photon interaction mechanism and whether the interacting particle(s) undergo FSI with the residual system. Each component is presented using the colour coding defined in figure 5.1.

As the Valencia model uses a nuclear matter approximation the predicted nucleon energies do not respect the reaction Q values of real nuclei. The missing energies obtained for each process thus start at 0 MeV. To compare directly with the data 8 MeV is subtracted from the predicted energy of each emitted nucleon before any observables are calculated. This value was found to give the correct average binding energy for direct 2N emission [29]. Previous comparisons [65] have also shown that this simple correction gives agreement with the data for a

Colour Coding for VM Predictions

	2N
	2N+FSI
	3N
	3N+FSI
	$N\pi$ +ABS
	$N\pi$ ( $\pi$ emitted)
	$NN\pi$ +ABS
	$NN\pi$ ( $\pi$ emitted)

Figure 5.1: Colour coding used to present the different initial photon interaction and FSI components of the Valencia model predictions.

range of photonuclear reactions and is as good as more complex formulae.

The measured missing energy distributions for the  $(\gamma, pn)$  and  $(\gamma, pp)$  reactions in the QD/NQD kinematics are compared with the Valencia model in figures 5.2 to 5.5. The data are presented for 8 photon energy bins covering the energy range  $E_\gamma = 150 - 700$  MeV. Data points are plotted beyond the high  $E_m$  threshold, which is imposed by the energy acceptances of the PiP and TOF detectors. In this region the visible cross section is necessarily zero and the data points do not represent actual experimental measurements.

### 5.2.1 The $(\gamma, pn)$ reaction

For the  $(\gamma, pn)$  reaction in QD kinematics (figure 5.2) the data shows the characteristic peak, near to the reaction threshold energy, corresponding to the residual nucleus being left in or near its ground state after the reaction. This is attributed to the detection of the two nucleons ejected after a direct 2N absorption of the photon on a proton neutron pair (quasi-deuteron). The direct 2N process becomes less important as  $E_\gamma$  increases with contributions from other more complex

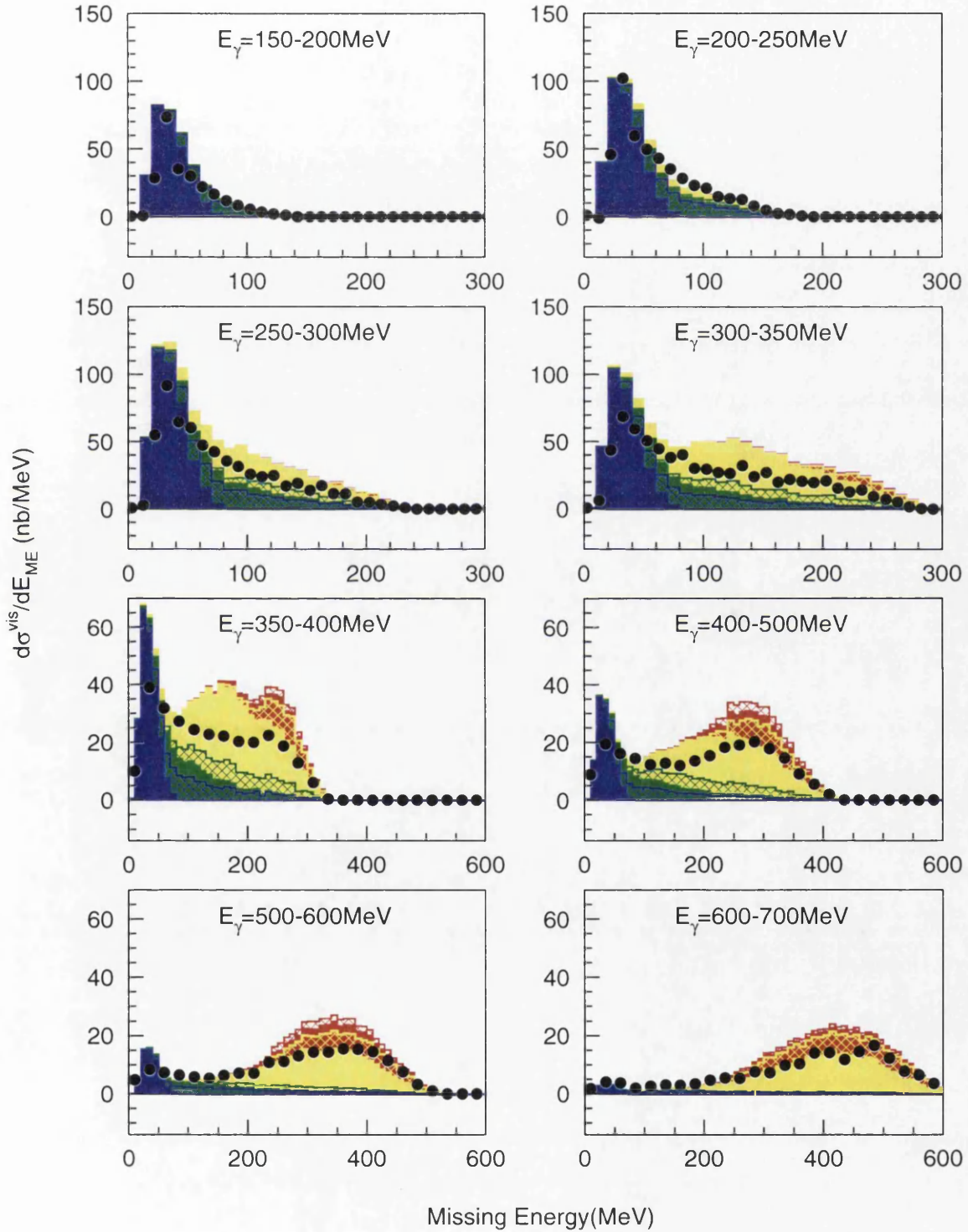
$^{12}\text{C}(\gamma, pn)\text{-QD KINEMATICS}$ 

Figure 5.2: Missing energy distributions for the  $^{12}\text{C}(\gamma, pn)$  reaction in QD kinematics compared with the predictions of the Valencia model.

## $^{12}\text{C}(\gamma, pn)\text{-NQD KINEMATICS}$

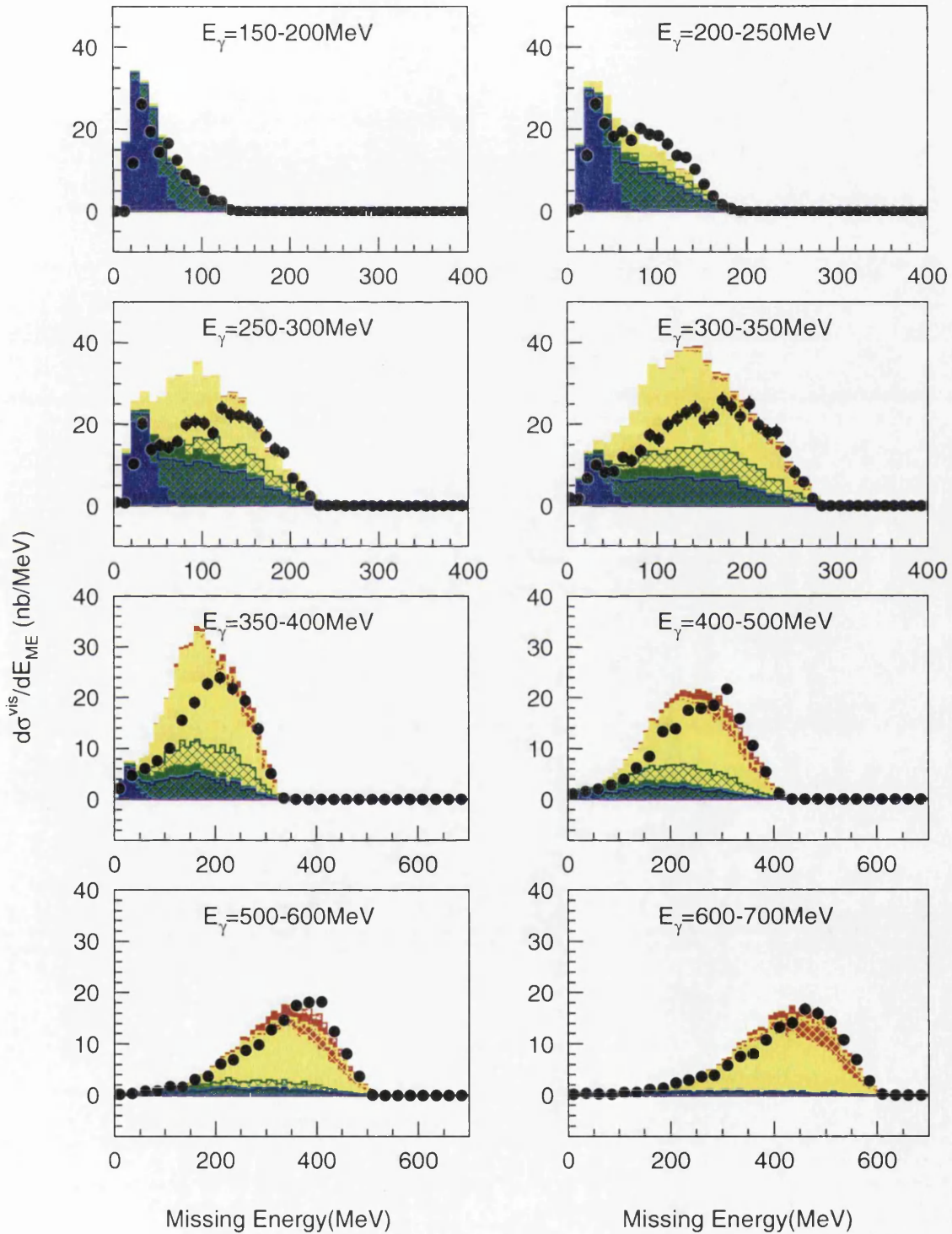


Figure 5.3: Missing energy distributions for the  $^{12}\text{C}(\gamma, pn)$  reaction in NQD kinematics compared with the predictions of the Valencia model.

processes giving large amounts of strength in regions of higher  $E_m$ . The contribution from low  $E_m$  events at the higher photon energies is however influenced by the upper detection thresholds of the detectors.

The Valencia model predictions describe the data well for photon energies below  $\sim 250$  MeV. As expected for these low photon energies the  $E_m \leq 70$  MeV region is shown to be dominated by direct 2N absorption with higher missing energies being populated by final state interactions of the outgoing nucleons, with lesser contributions from the  $3N_{direct}(+FSI)$  channels.

As the photon energy increases into the region of the  $\Delta$  resonance the  $N\pi$  with subsequent  $\pi$  absorption ( $N\pi+ABS$ ) contribution is predicted to become increasingly important to the overall cross section. The model starts to overestimate the experimental data in this region. The predicted bump in the cross section due to opening of the  $\pi$  emitted channels (predominantly from initial  $N\pi$  with the pion emitted after scattering) is evident in the data for  $E_\gamma = 350-400$  MeV. For higher photon energies the only major contribution originates from initial  $\pi$  production channels. The  $E_\gamma \geq 500$  MeV data is however already overestimated by the Valencia model without the inclusion of the  $2\pi$  processes discussed in section 1.4.1.

Data from the NQD kinematics (Fig 5.3) in the  $E_m \leq 70$  MeV region show a marked reduction in the contribution of the direct 2N process, with the peak a factor of  $\sim 2$  less for the lowest  $E_\gamma$  range and rapidly decreasing to a factor of  $\sim 10$  less for  $E_\gamma \sim 300$  MeV. The magnitude of the 2N process diminishes with photon energy at a faster rate than in the QD region due to the momentum of the initial pair in the nucleus being restricted to successively larger values when the particles are viewed in the more extreme kinematics. The cross section has little low  $E_m$  contribution above  $E_\gamma \sim 500$  MeV, although again this will be influenced by the experimental detection thresholds. The kinematic restriction of 2N processes in

these kinematics thus amplifies the relative importance of other channels to the observed yield.

The Valencia model can be seen to reproduce the main features of the data, even in the more unusual kinematics, but gets the strength wrong in some  $E_m$  regions. The predicted reduction in the magnitude of the (low  $E_m$ ) 2N process is in good agreement with the data for all photon energies. The more backward angle TOF coverage shows increased sensitivity to 2N+FSI contributions which is relevant to the more detailed investigations of direct 2N processes examined in the next section.

A greater sensitivity to the  $3N_{direct}(+FSI)$  processes is also observed in the NQD region although the strength of the  $N\pi+ABS$  channel means the  $3N_{direct}(+FSI)$  process is not predicted to dominate for any  $E_m$  region. For photon energies through the  $\Delta$  resonance the  $N\pi+ABS$  process is again predicted to become increasingly important to the cross section. The overestimation of the data observed in the corresponding QD region is also observed here. Above 500 MeV, where some excess may be expected to be observed in the data due to  $2\pi$  production, the model gives good agreement.

Previous comparisons [64, 29] with the Valencia model have given better agreement for the strength of the  $(\gamma, pn)$  channel than this work, although the previous comparisons were averaged over much larger photon energy bins. These measurements were also taken with the PiP detector covering the more central proton angles ( $50^\circ - 130^\circ$ ) and so this may indicate that the angular distributions of some of the processes included in the theory do not reflect the experimental results.

### 5.2.2 The $(\gamma, pp)$ reaction

The data obtained for the  $(\gamma, pp)$  channel in the QD region are shown in Fig 5.4. The  $E_m \leq 70$  MeV yield is seen to be an order of magnitude down on the

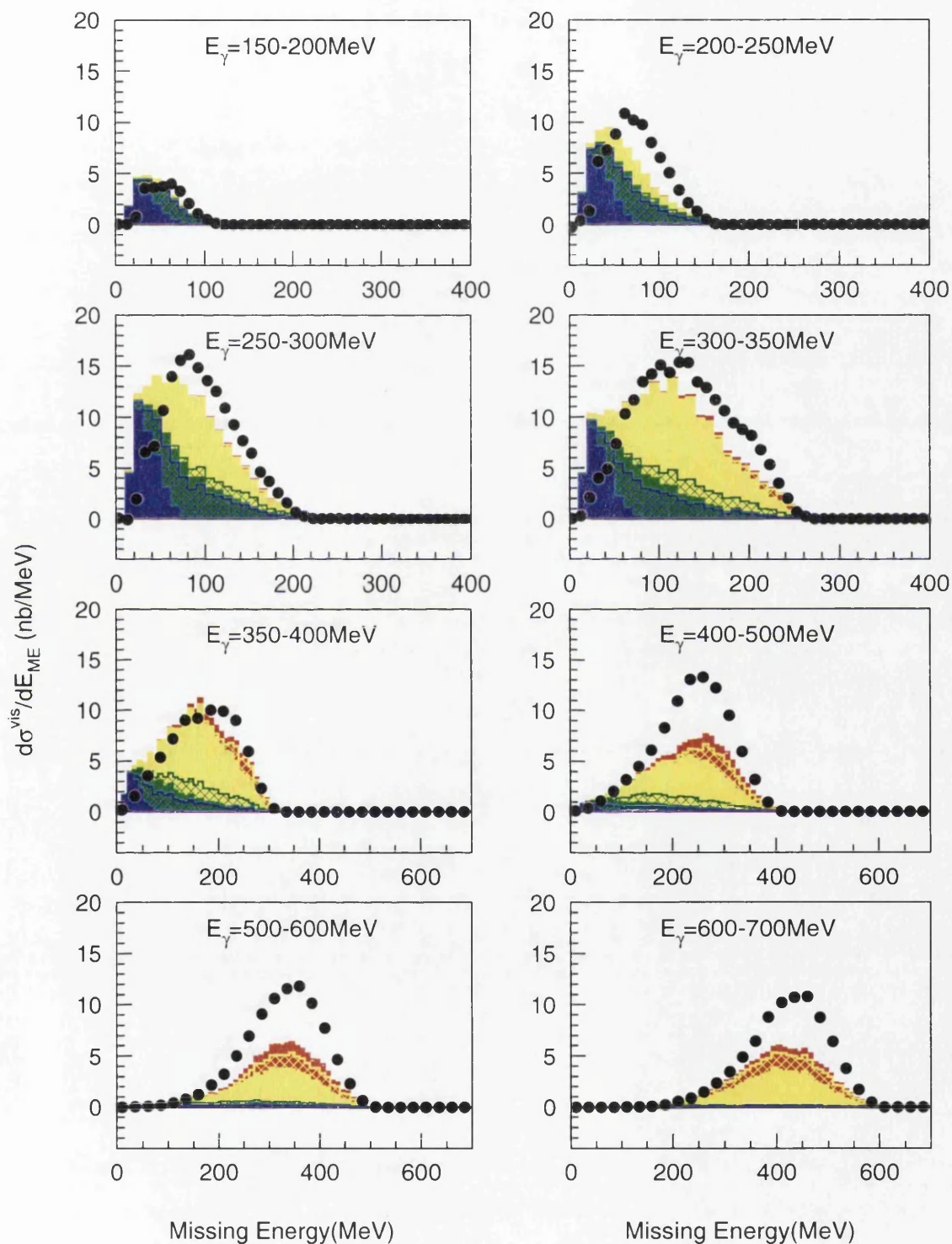
$^{12}\text{C}(\gamma, pp)\text{-QD KINEMATICS}$ 

Figure 5.4: Missing energy distributions for the  $^{12}\text{C}(\gamma, pp)$  reaction in QD kinematics compared with the predictions of the Valencia model. The VM predictions have been divided by a factor 3.5.

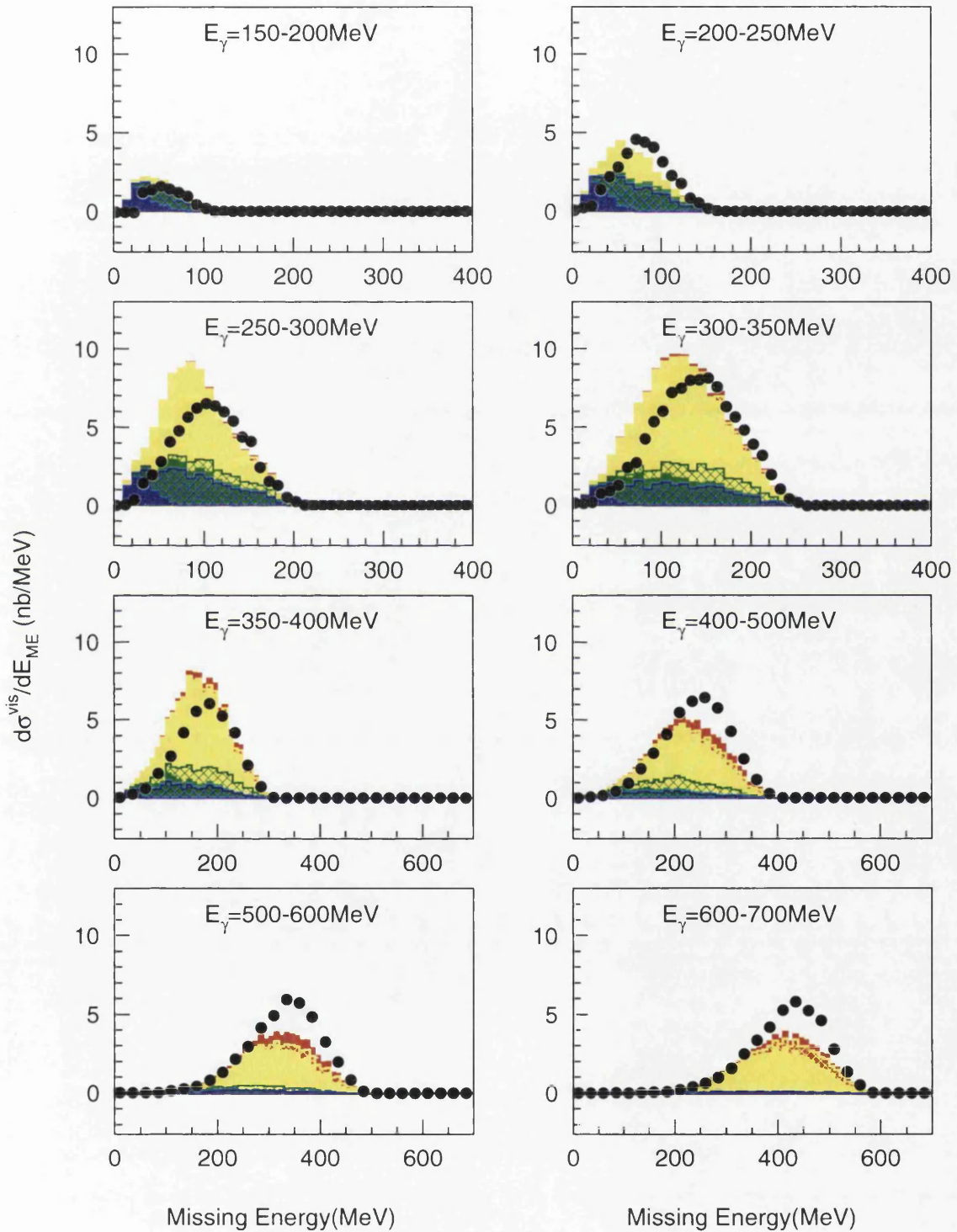
$^{12}\text{C}(\gamma, pp)\text{-NQD KINEMATICS}$ 

Figure 5.5: Missing energy distributions for the  $^{12}\text{C}(\gamma, pp)$  reaction in NQD kinematics compared with the predictions of the Valencia model. The VM predictions have been divided by a factor 3.5.

corresponding  $(\gamma, pn)$  yield, due primarily to the reduction of the 2N contribution caused by the suppression of meson exchange currents for the  $T=1$  pp pair. The low  $E_m$  yield is observed to diminish rapidly and to essentially disappear when the photon energy reaches  $\sim 500$  MeV. The  $(\gamma, pp)$  data will however show a greater influence from detector thresholds than  $(\gamma, pn)$  due to the maximum energy of  $\sim 230$  MeV at which TOF can be used for proton detection due to the proton/pion separation cut (figure 4.3). The resulting depression of the low  $E_m$  yield means that a larger fraction of the visible cross section originates from high  $E_m$  components than in the corresponding  $(\gamma, pn)$  channel.

The predictions of the Valencia model shown on the figure have been reduced by a factor of 3.5 in order to reduce the discrepancy between it and the data. A similar factor was found necessary to compare with the previous  $(\gamma, pp)$  experimental measurements at Mainz [29, 64, 65] and Saskatchewan [66]. The importance of the 2N+FSI channel to the predicted  $(\gamma, pp)$  yield (originating primarily from initial  $(\gamma, pn)$  with a charge exchange FSI) is evident for lower photon energies. The  $N\pi$ +ABS channel, however, again becomes the dominant process as the photon energies pass through the  $\Delta$  resonance. Above  $E_\gamma=400$ MeV the scaling factor of 3.5 no longer produces agreement with the data, implying that the overestimation of the data by the model is photon energy dependent. This observation is consistent with ref. [64, 29, 65].

The experimental results for the  $(\gamma, pp)$  channel in the NQD kinematics are shown in figure 5.5. The cross section for the low  $E_m$  region can be seen to be a factor of  $\sim 5$  down on the corresponding QD data due to kinematic restrictions on the initial (2N) pair momenta. The relative contribution of high  $E_m$  components decreases by a smaller factor ( $\sim 2$ ) due to the wider angular distribution of these processes. Above 500 MeV the measured cross section is seen to originate entirely from the higher  $E_m$  components.

The predictions of the Valencia model in the NQD region shown in figure 5.5 have been reduced by the same factor of 3.5 as applied to the QD region results. The relative reduction in the contribution of direct 2N absorption in going from the QD to the NQD kinematics is reasonably well described by the Valencia model with the 2N process predicted to make up only a small part of the cross section for photon energies around the  $\Delta$  resonance. The relative proportion of the 2N+FSI process is similar for both kinematic regions although the strength is distributed over a wider range of  $E_m$  for the NQD case. This indicates that a lot of the strength comes from an initial 2N absorption, originating nearer to the QD kinematics, followed by a hard final state interaction which gives a lot of energy to the residual nucleus therefore smearing the  $E_m$  over a wider range.

The overestimation of the  $(\gamma, pp)$  data by the VM is somewhat greater for the NQD kinematics than for the QD kinematics therefore indicating the discrepancy is angle dependent. The photon energy dependence of these discrepancies look similar in both kinematic regions.

### 5.3 Comparisons of the low $E_m$ regions with the 2N model

The contribution of direct 2N mechanisms are calculated in the Valencia model from an initial Fermi gas distribution of nucleon energies, which therefore does not take into account the shell structure of a real nucleus. Although this approximation allows an estimate of the overall strength of the 2N process it does not permit a detailed interpretation of the distribution of other kinematic variables in this region.

For these regions of low excitation of the residual nucleus a comparison with the previously described 2N [16] model is used. The low  $E_m$  data are again

compared with the model for the two regions of QD and NQD kinematics, with the QD region data also used to determine the spectrum of excitation energies and normalise the strength of the 2N model as described below. The data are separated into the two missing energy regions  $E_m \leq 40$  MeV and  $E_m = 40-70$  MeV, to select regions where photon absorption on  $(1p)^2$  or  $(1s)(1p)$  nucleon pairs dominates. No attempt was made to look specifically for  $(1s)^2$  strength as the contribution is expected to be weak and spread over a wide range of  $E_m$  [16].

The excitation distribution of the residual nucleus (into  $4\pi$ ) used in the model is obtained from the data by an iteration procedure. The excitation distribution is chosen so that the predicted shape of the missing energy visible in the detectors matches that of the data. This procedure is undertaken in the QD kinematic region where the measured missing energy will have less contamination from non 2N events. The model is then used to predict the  $E_m$  distribution in the NQD region and other kinematic variables in both regions.

The magnitude of the 2N model prediction is also normalised to the QD region data, for both the chosen missing energy regions. The same normalisation factors are applied to the model predictions for the NQD kinematics, allowing predictions of both the shape and magnitude of variables to be made in this region.

Predictions from the ‘phase space model’ are also presented, where the photon momentum is distributed between the 2 nucleons and the recoiling system according to the available phase space. Comparisons between the 2N and phase space predictions show the sensitivity of kinematic variables to correlations between the participating nucleons.

### 5.3.1 The $(\gamma, pn)$ reaction

- Missing Energy Distributions

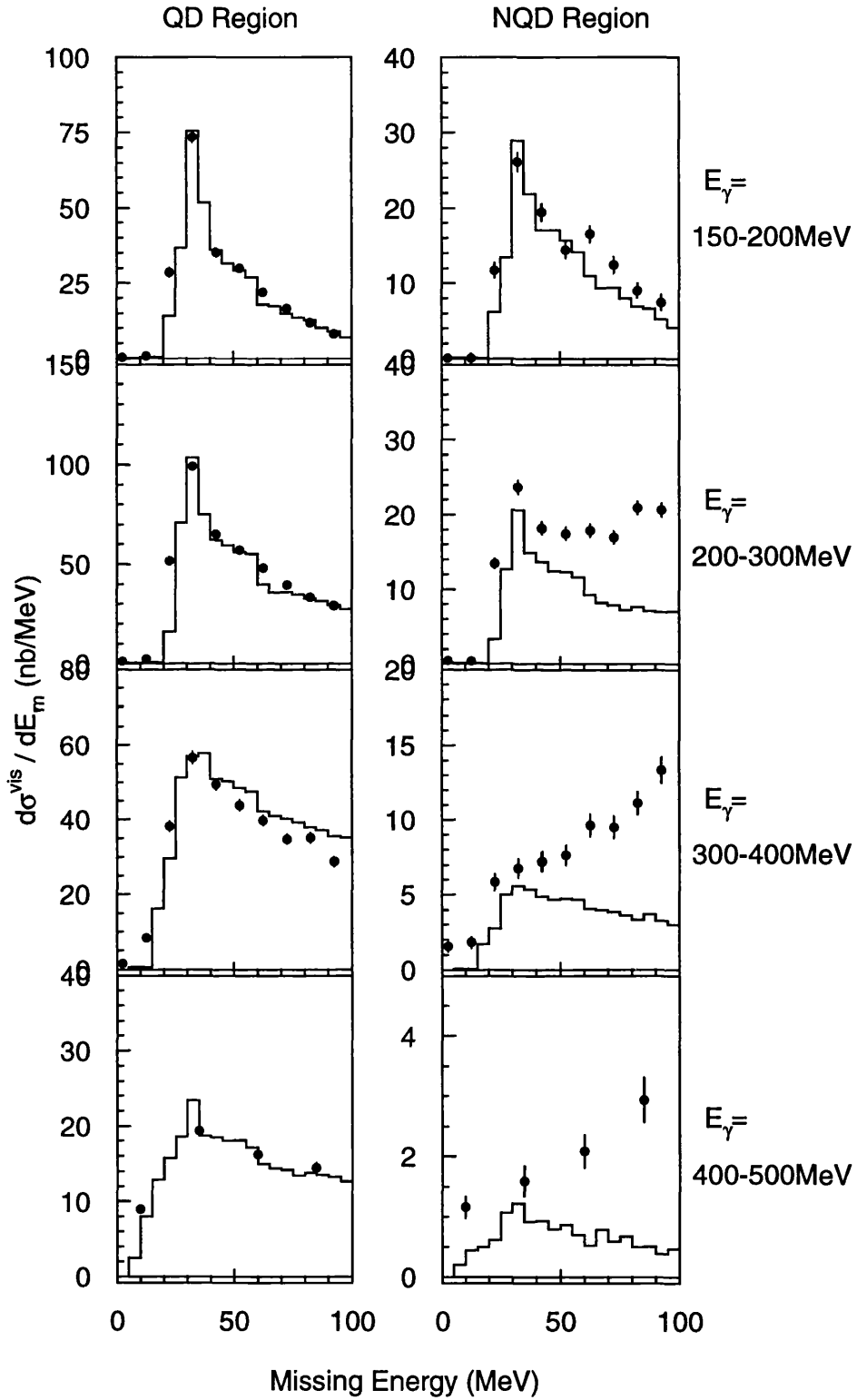
$^{12}\text{C}(\gamma, pn)$  – Missing Energy Distributions

Figure 5.6:  $^{12}\text{C}(\gamma, pn)$  missing energy distributions in QD/NQD kinematics compared with the  $2N$  model predictions. The fits in the QD region reflect the  $2N$  model calibration only.

The measured missing energy distributions (for  $E_m \leq 100$  MeV) in the QD/NQD regions are compared with the 2N model in figure 5.6. A large difference in the cross section magnitude is observed between the two regions, a difference which increases with  $E_\gamma$ .

The comparison with the 2N model in the QD region essentially shows the model calibration, with the shape of the missing energy distribution reflecting the accuracy of the iteration procedure used to determine the  $4\pi$  excitation distributions. The predictions in the NQD region (using the same excitation distributions and normalisation factors as the QD case) give an indication as to how much of the observed  $E_m$  strength can be attributed to the direct 2N process. The relative contribution of the 2N process is seen to decrease with increasing  $E_\gamma$ , with the excess generally concentrated in the  $E_m \geq 40$  MeV region, and at higher  $E_\gamma$  the excess increases with  $E_m$ . Below  $E_m = 40$  MeV the drop in magnitude and changes in the shape of the data in the NQD kinematics are reasonably well described by the dynamics of a 2N model.

### • Missing Momentum Distributions

The missing momentum distributions are an important variable in understanding the contribution of different mechanisms to the measured cross section. For a direct photon absorption on a 2N pair in a spectating nucleus (no subsequent FSI) the missing momentum reflects the initial momentum of the nucleon pair. Figure 5.7 shows the missing momentum distributions for the  $(\gamma, pn)$  reaction in the QD kinematics, separated into the two missing energy regions corresponding to expected absorption on either  $(1p)^2$  or  $(1s)(1p)$  pairs.

The similarity of the shape of the data at all  $E_\gamma$  for both regions is consistent with expectations of a dominant direct 2N mechanism. The phase space calculations (dashed line) extend to much higher  $P_m$  values than the data and therefore

indicate that the measured distributions are not simply determined by detector threshold effects (the fluctuations observed in the phase space predictions are statistical only).

The solid line shown on the figure illustrates the (normalised) predictions of the 2N model. No predictions were possible for  $E_\gamma \geq 600$  MeV due to the restricted photon energy range of the parameterisations employed in the model. For the low  $E_m$  region the 2N model is normalised to the data over the entire range of  $P_m$ . The higher  $E_m$  region is normalised up to  $P_m = 260$  MeV/c, as there is some evidence of a tail at higher  $P_m$  values which would otherwise distort the normalisation.

For  $E_m \leq 40$  MeV the predicted shape of the missing momentum distributions from the 2N model give an excellent description of the data for photon energies up to 600 MeV. This indicates that in this region the reaction must proceed predominantly through photon absorption on  $(1p)^2$  pairs. No significant strength is observed above the prediction of the 2N model implying that in this region the contribution of processes other than direct 2N emission are negligibly small. Any FSI processes do not significantly distort the shape of the distribution and so must either constitute a small effect or remove events to higher  $E_m$  or outside the QD detector acceptance from all  $P_m$  regions with a similar probability. The phase space predictions are well removed from the 2N model predictions, especially at higher photon energies, showing the sensitivity of the comparison to the correlations between the participating nucleons. Although no 2N model comparisons could be made for  $E_\gamma = 600-700$  MeV the data show similar characteristics to that observed for lower photon energies and are well removed from the phase space prediction. This behaviour would not be observed if either FSI or multiparticle processes made a significant contribution.

The extended  $E_\gamma$  range and improved statistical accuracy over previous exper-

iments [19] enables the contribution of the direct 2N emission process at  $E_\gamma \geq 400$  MeV to be established for the first time. The 2N process is interesting at these high photon energies as the photon must necessarily couple to shorter ranged structures and so may be sensitive to different microscopic mechanisms.

The data in the  $E_m=40-70$ MeV region are also well described by the 2N model, indicating that in this region the reaction can be well described by photon absorption on (1s)(1p) pairs. Some measured strength is evident at  $P_m$  values above the 2N model prediction but the events constitute a small fraction of the observed yield. For the lowest photon energy bin the phase space is constrained, due to the increased influence of the detector low energy thresholds with the imposition of the higher missing energy requirement. For higher photon energies however there is a clearer separation between the 2N and phase space predictions. For  $E_\gamma \geq 600$  MeV, although no comparison is made with the 2N model, the data can again be seen to show characteristics which are not consistent with the strong influence of FSI/multiparticle processes.

The corresponding  $P_m$  distributions in the NQD region are shown as figure 5.8. The measurement of the 2N process in the more extreme NQD kinematics can be seen to sample regions of higher initial pair momenta. The data shifts to higher  $P_m$  with increasing  $E_\gamma$  as the initial pair progressively requires larger initial momenta to kinematically allow the proton and neutron to hit the more backward angle TOF detectors.

The separation of the available phase space from the data is more apparent than in the QD kinematics. This gives improved confidence in the interpretation, especially at lower photon energies. The cross sections in the NQD kinematics, as discussed for the  $E_m$  variable, possess less strength than the corresponding data from the QD region. The reduction in strength is more marked for the higher photon energies. This is due to the diminishing probability of finding

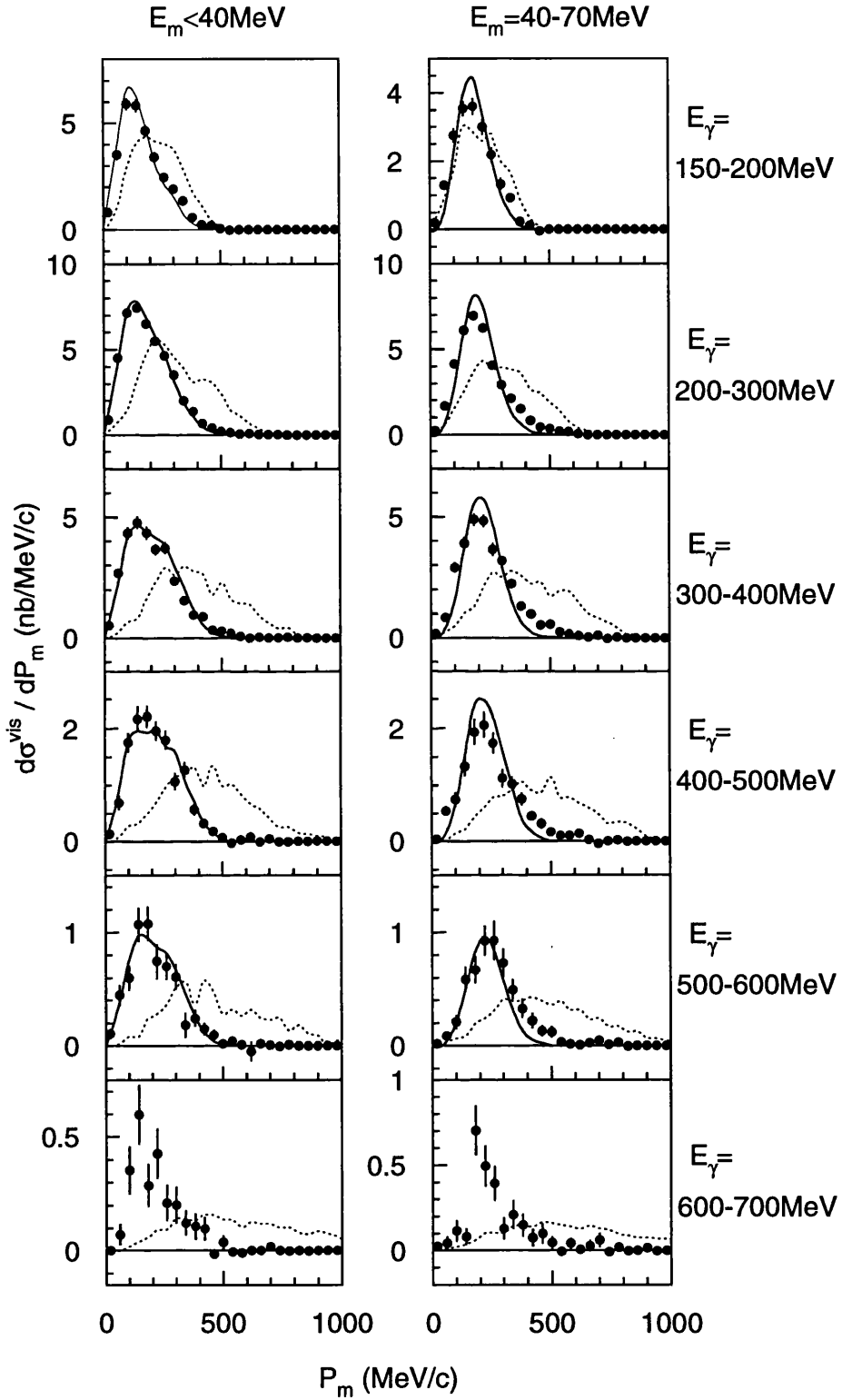
$^{12}\text{C}(\gamma, pn)$  – QD KINEMATICS

Figure 5.7:  $^{12}\text{C}(\gamma, pn)$  missing momentum distributions compared with the  $2N$  model (solid line) for  $E_\gamma \leq 600 \text{ MeV}$  (see text) and phase space predictions (dashed line) for two missing energy regions in the QD kinematics.

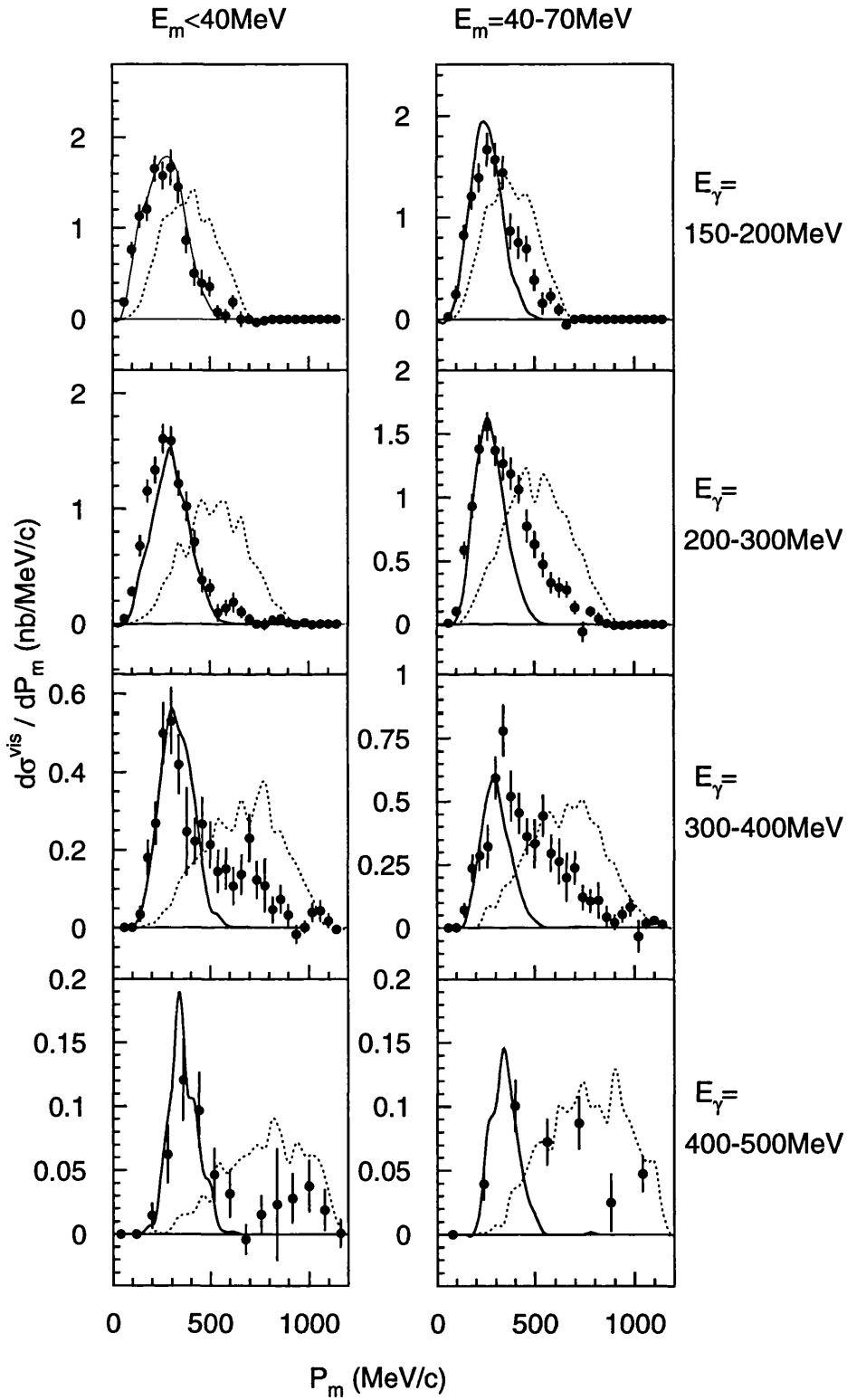
$^{12}\text{C}(\gamma, pn) - \text{NQD KINEMATICS}$ 

Figure 5.8:  $^{12}\text{C}(\gamma, pn)$  missing momentum distributions compared with the  $2N$  model (solid line) and phase space predictions (dashed line) for two missing energy regions in the NQD kinematics.

nucleon pairs with sufficient momentum to oppose that of the photon and allow the particles to be observed in the detectors.

The 2N model predictions (solid line) are obtained with the same normalisation factors and excitation distributions used for the QD region (Fig 5.7). In the  $E_m \leq 40$  MeV region the 2N model gives a good description of the data for  $E_\gamma \leq 300$  MeV, with the shape and magnitude of the recoil momenta in good agreement with that predicted from absorption on  $(1p)^2$  nucleon pairs. Little strength is observed above the model prediction implying that other processes and/or final state interactions give a relatively small contribution to the yield. For photon energies above 300 MeV a significant tail is observed with  $P_m \geq \sim 600$  MeV/c. Nevertheless the strength of this tail is  $\leq \sim 3\%$  of the 2N strength estimated in both the QD and NQD regions. These results therefore show the dominance of the direct 2N emission process for the  $E_m \leq 40$  MeV region, even with a phase space coverage which included regions away from the more usual back-to-back kinematics. This reinforces the findings of previous works [16, 19, 20, 47] by showing that the observed 2N dominance at low  $E_m$  was not simply due to the positioning of the detectors in suitable kinematics.

Detailed analysis shows that events populating the observed high  $P_m$  tail are characterised by comparatively lower proton energies and higher neutron energies which allow the recoil momentum to be large whilst still having a missing energy less than the required 40 MeV. The corresponding Valencia predictions for the low  $E_m$  region predict the only competing mechanisms are the 2N+FSI,  $3N_{direct}$ (+FSI) and  $N\pi$ +ABS processes. The 2N model accounts for almost all of the  $P_m \leq 300$  MeV/c strength in the data making it unlikely that these events could come from a 2N+FSI reaction in the NQD kinematics. This does not rule out 2N+FSI contributions from regions outwith these kinematics, although the photon energy dependence of the tail is more consistent with that of processes

involving intermediate  $\Delta$  or  $\pi$  production.

For the higher missing energy region,  $E_m=40-70$  MeV, the cross sections show additional strength at higher  $P_m$  values, the relative contribution of which increases with photon energy. The phase space predictions again show greater separation from the data than in the corresponding QD region. This is especially important for the lowest photon energy bin where all previous measurements showed little separation from the phase space prediction for this  $E_m$  region and therefore allowed only limited interpretation.

The 2N model (solid line) predicts the strength for  $P_m \leq 300$  MeV/c with reasonable accuracy, indicating that a significant mechanism is still direct absorption on a (1s)(1p) pair. Although the NQD region data shows a large proportion of events with  $P_m$  greater than the 2N prediction, especially for higher  $E_\gamma$ , the excess only constitutes a maximum of  $\sim 10\%$  of the total (QD+NQD)  $E_m=40-70$  MeV yield and only  $\sim 5\%$  of the total yield for  $E_m \leq 70$  MeV.

#### • Recoil Theta Distributions

A further test of the 2N absorption model can be made by a comparison of the predicted recoil theta ( $\theta_{rec}$ ) distributions with the data. For a direct 2N emission process  $\theta_{rec}$  reflects the (kinematically sampled) initial momentum direction of the nucleon pair. The normalisation factors applied to the 2N model  $\theta_{rec}$  predictions are the same as those used for the corresponding  $P_m$ .

The  $\theta_{rec}$  distributions obtained in the QD kinematics are shown in figure 5.9, again separated into the two  $E_m$  regions corresponding to photon absorption on (1p)<sup>2</sup> and (1s)(1p) pairs. The QD region data can be seen to populate the entire 0°-180° range of  $\theta_{rec}$ , as expected from an isotropic direction of the initial pair, although with a bias towards forward angles. This is due to the influence of the positions and thresholds of the detectors. As the photon energy is increased the

$\theta_{rec}$  distribution is pushed more forward as the momentum of the nucleon pair must necessarily oppose more the increasing photon momentum to allow the particles to be observed in the detectors. The corresponding phase space predictions show a more extreme forward peaked distribution as the photon momentum is split between the 2 nucleons and the recoil nucleus which must necessarily go more forward to conserve momentum.

The 2N model is seen to describe the  $E_\gamma \leq 600$  MeV data in the QD region well, for both  $E_m$  regions, providing further strong evidence for the dominance of direct 2N emission at low  $E_m$ . For  $E_\gamma \geq 600$  MeV the data again show distributions similar to that observed at lower photon energies and exhibit a large separation from the phase space prediction, behaviour which does not indicate the strong influence of FSI/multiparticle processes.

The data from the NQD region (figure 5.10) shows an extreme forward bias in the  $\theta_{rec}$  distributions, with events only populating regions of  $\theta_{rec} \leq 80^\circ$ . The data for all  $P_m$  values are shown as solid circles. The triangular data points show the distributions obtained after applying cuts on the corresponding  $P_m$  distributions to select regions near to the direct 2N prediction.

For the  $E_m \leq 40$  MeV region the 2N model predicts the shape and magnitude of the data well, with the data cut on the 2N region of  $P_m$  (triangles) giving improved agreement with the predicted distribution. The difference between the full and cut data shows that the tail of events above the 2N predictions in the  $P_m$  distributions tends to populate all accessible regions of  $\theta_{rec}$ .

For  $E_m = 40-70$  MeV the 2N predictions are also in good agreement with the data cut on the 2N region of  $P_m$ , although it should be noted that the cuts will necessarily remove some direct 2N strength as well as including a proportion of other events present. Nevertheless the agreement obtained gives a strong indication of direct (1s)(1p) photon absorption in this region. The excess strength

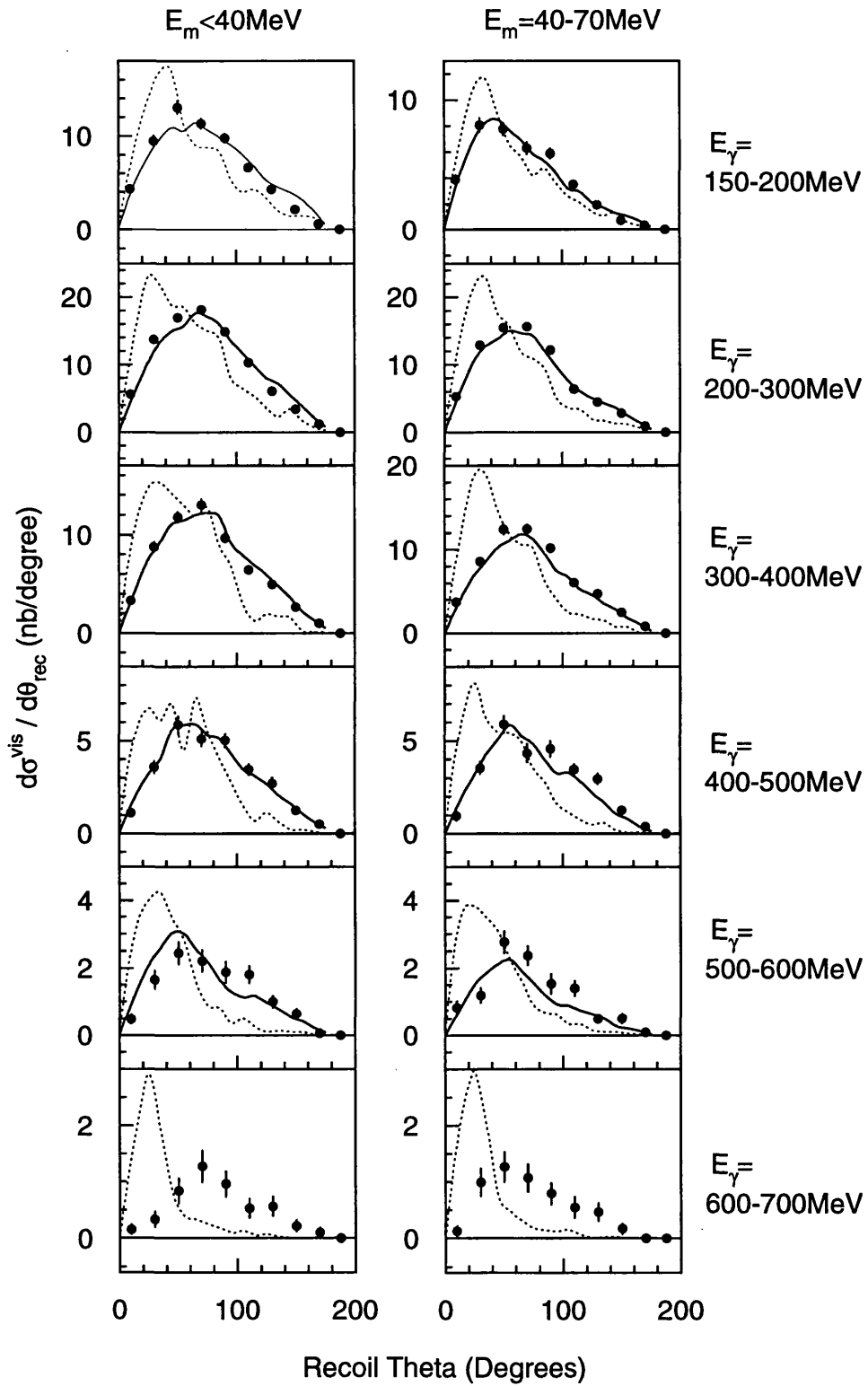
$^{12}\text{C}(\gamma, pn) - \text{QD KINEMATICS}$ 

Figure 5.9:  $^{12}\text{C}(\gamma, pn)$   $\theta_{\text{rec}}$  distributions compared with the 2N model (solid line) for  $E_\gamma \leq 600\text{ MeV}$  (see text) and phase space predictions (dashed line) for two missing energy regions in the QD kinematics.

$^{12}\text{C}(\gamma, pn) - \text{NQD KINEMATICS}$

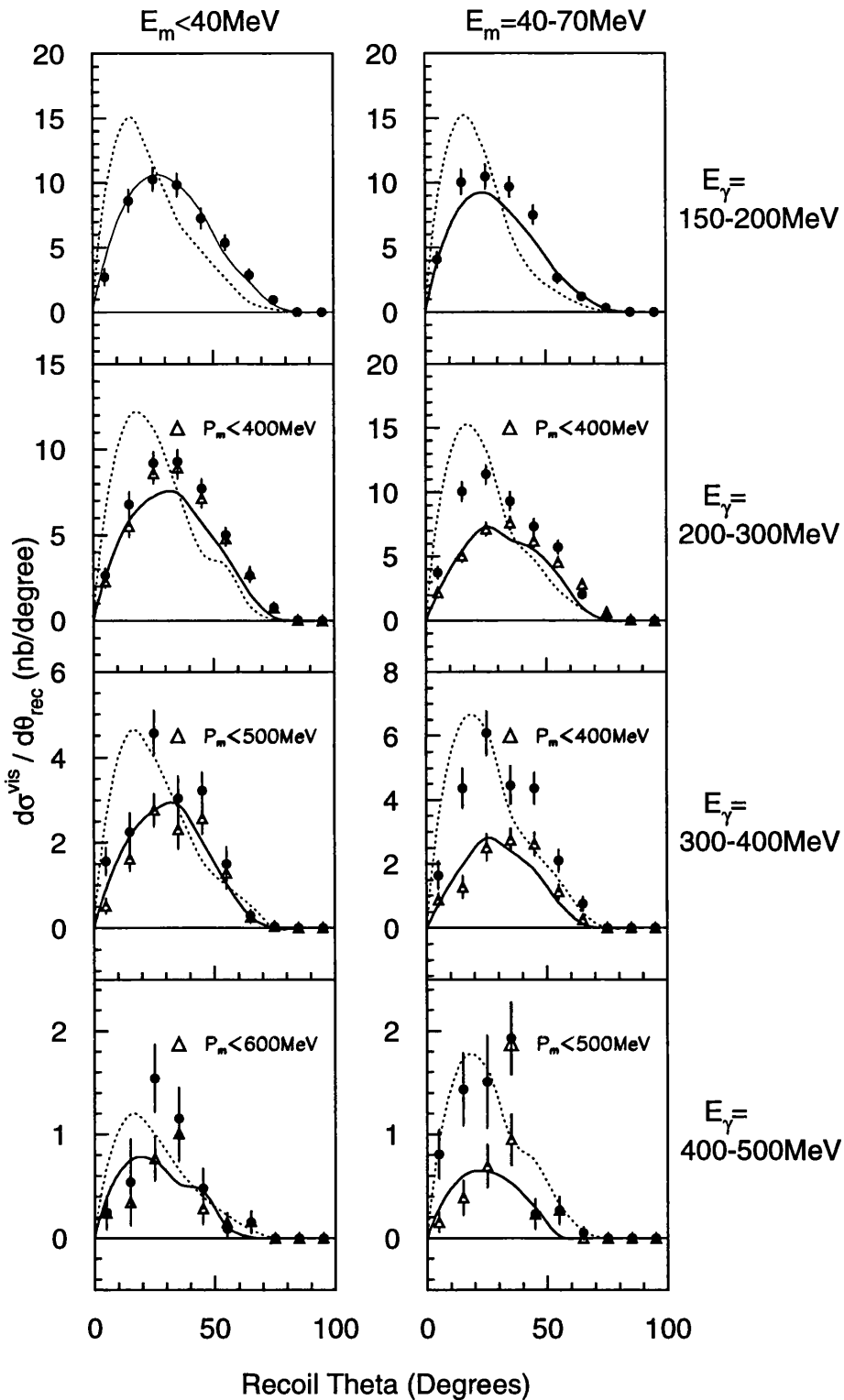


Figure 5.10:  $^{12}\text{C}(\gamma, pn) \theta_{\text{rec}}$  distributions compared with the  $2N$  model (solid line) and phase space predictions (dashed line) for two missing energy regions in the NQD kinematics. The data shown as solid circles is for all  $P_m$  while the triangular points represent the distributions obtained after selecting the  $2N$  region of the data from the corresponding  $P_m$  distributions.

above the 2N prediction forms a peaked distribution centred around  $\sim 25^\circ$ , similar in shape to the predicted phase space. This is consistent with the involvement of FSI or multiparticle processes which will smear out any correlations between the two detected particles.

### 5.3.2 The $(\gamma, pp)$ reaction

- **Missing Energy Distributions**

Figure 5.11 shows the measured missing energy distributions ( $E_m \leq 100$  MeV) for the  $(\gamma, pp)$  reaction in the QD and NQD regions compared with the results of the 2N model. A large difference in strength is observed between the data from the two regions. As seen in the  $(\gamma, pn)$  data this difference increases with  $E_\gamma$ .

The 2N model predictions in the QD region simply illustrate the model calibration and quality of the iteration procedure used to obtain the excitation distributions. The proportion of the total  $E_m$  strength which can be accounted for by the 2N prediction in the NQD kinematics is seen to decrease rapidly with photon energy, as observed for the  $(\gamma, pn)$  reaction. The predicted shape and magnitude for  $E_m \leq 40$  MeV are however in reasonable agreement with the data. It is significant that for this  $E_m$  region the drop in the magnitude of the NQD cross section relative to the QD can be described by a model based on 2N kinematics.

- **Missing Momentum Distributions**

The missing momentum distributions obtained for the  $(\gamma, pp)$  reaction in the QD kinematics are shown in figure 5.12. The corresponding phase space distributions show good separation from the data for higher photon energies, but the lowest  $E_\gamma$  bin shows the data is constrained in both  $E_m$  regions by the detector thresholds. This effect, which also restricted the interpretation of previous measurements, is

$^{12}\text{C}(\gamma,pp)$  – Missing Energy Distributions

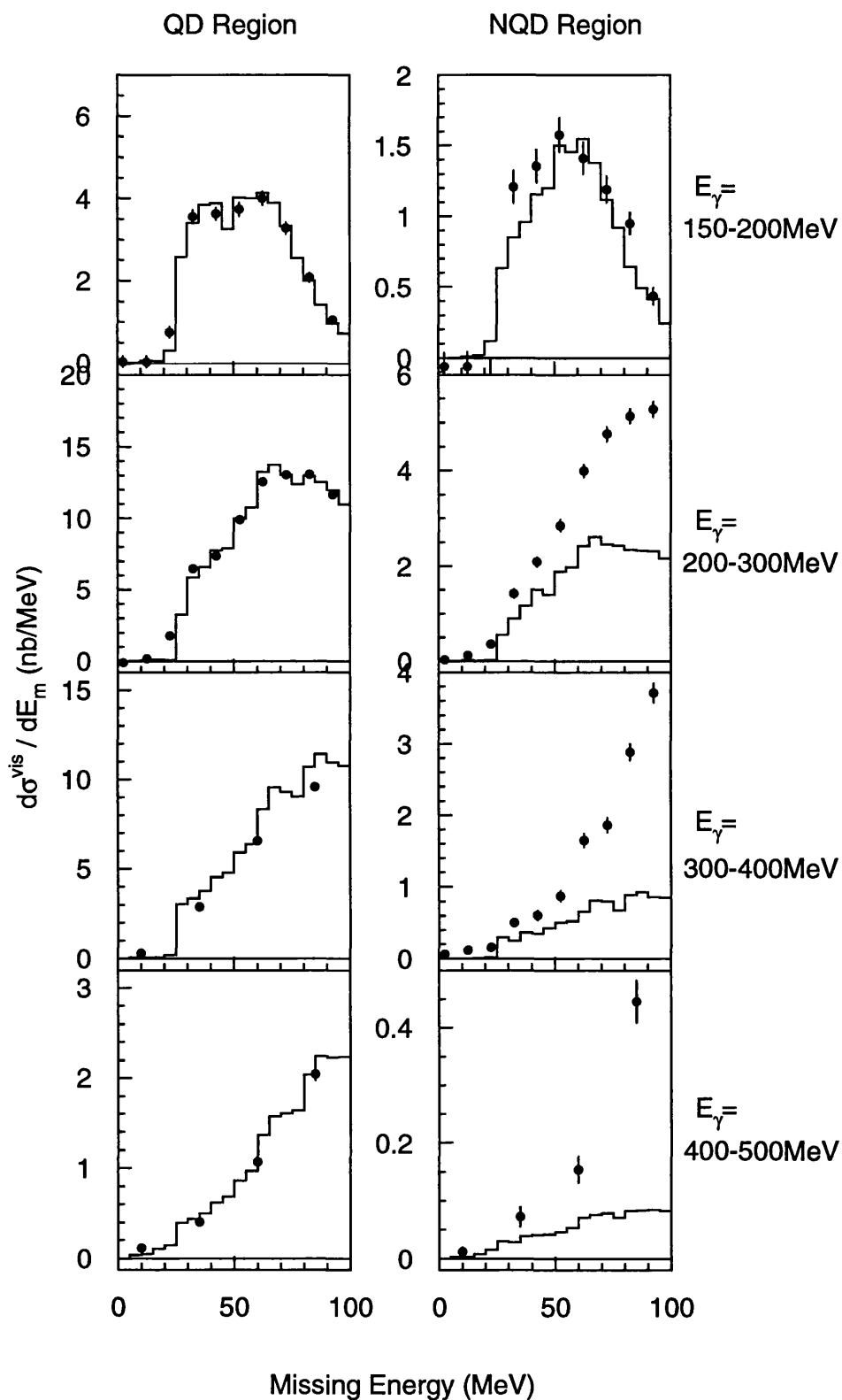


Figure 5.11:  $^{12}\text{C}(\gamma,pp)$  missing energy distributions in QD/NQD kinematics compared with the 2N model predictions. The fits in the QD region reflect the 2N model calibration only.

$^{12}\text{C}(\gamma, pp)\text{-QD KINEMATICS}$

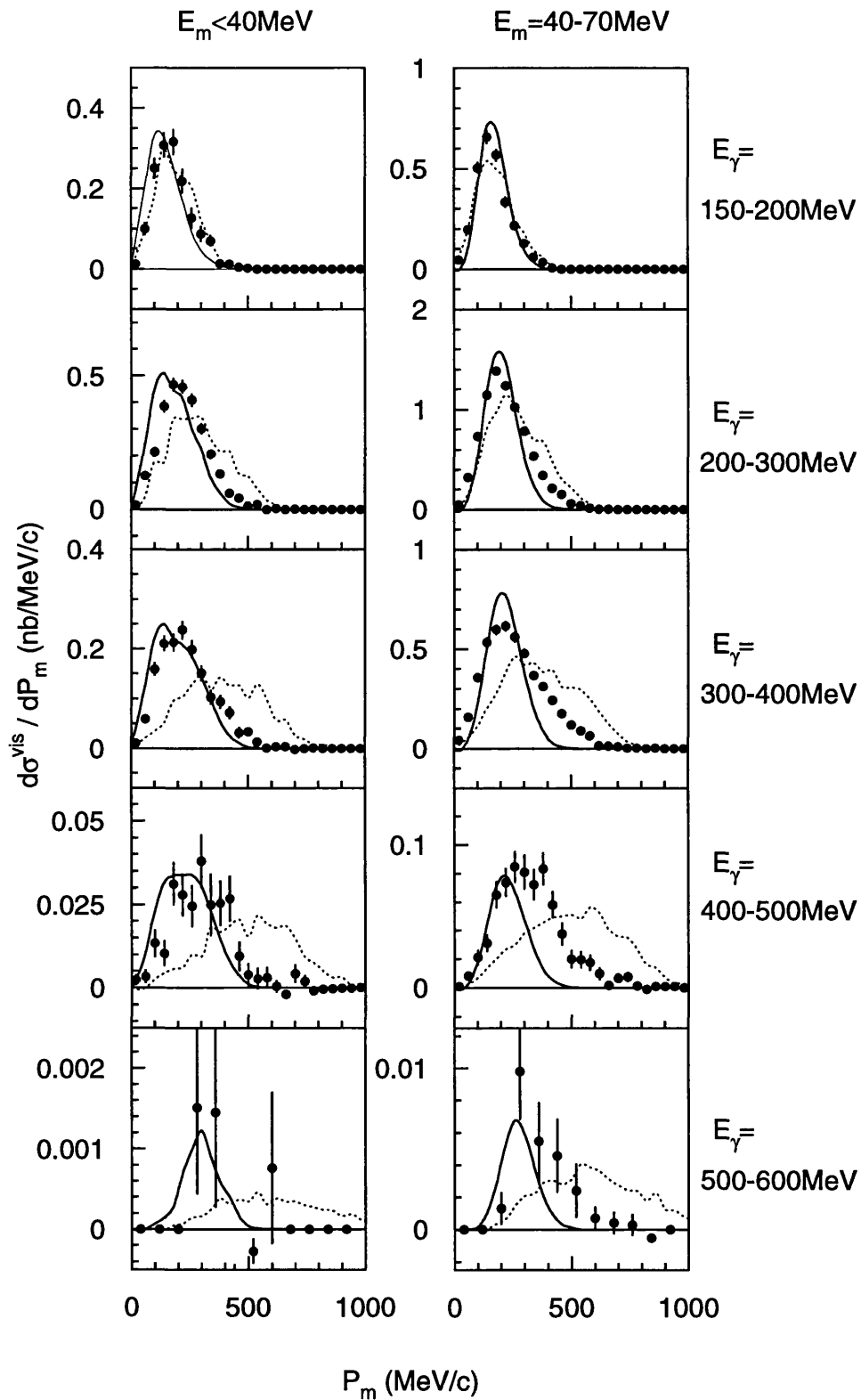


Figure 5.12:  $^{12}\text{C}(\gamma, pp)$  missing momentum distributions compared with the  $2N$  model (solid line) and phase space predictions (dashed line) for two missing energy regions in the QD kinematics.

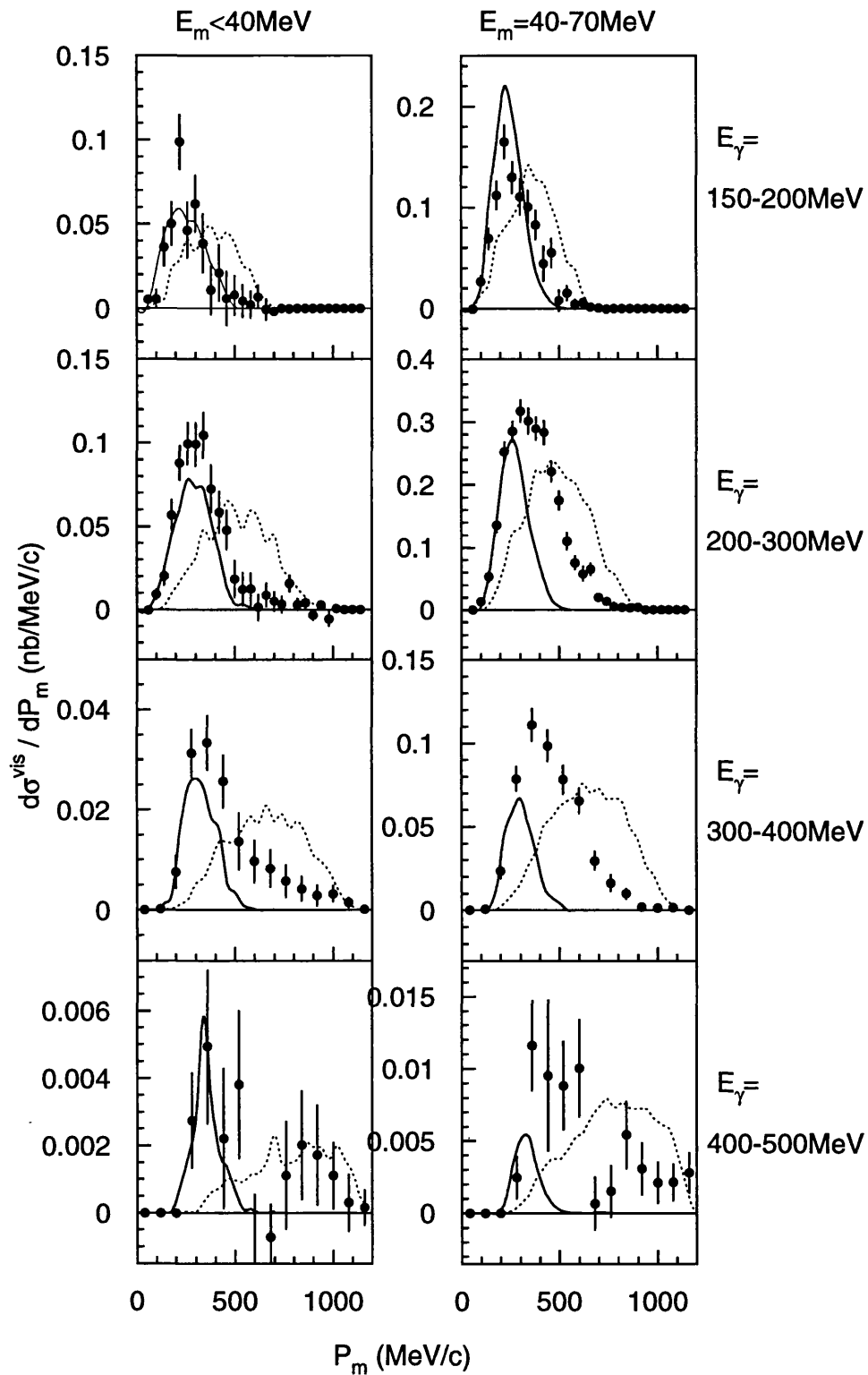
$^{12}\text{C}(\gamma, pp) - \text{NQD KINEMATICS}$ 

Figure 5.13:  $^{12}\text{C}(\gamma, pp)$  missing momentum distributions compared with the 2N model (solid line) and phase space predictions (dashed line) for two missing energy regions in the NQD kinematics.

more acute for the  $(\gamma, pp)$  case than the  $(\gamma, pn)$  due to the higher ( $\sim 40$  MeV) threshold for the detection of a proton in TOF. The solid line in the figure shows the (normalised) predictions of the 2N model. The low  $E_m$  region is normalised over the entire range of the data while the higher region, where more contribution from non-2N events is expected, is normalised over the range 0–260 MeV/c.

For  $E_m \leq 40$  MeV the 2N model describes the shape of the  $P_m$  distributions reasonably well, although the agreement is not as good as that observed for the  $(\gamma, pn)$  reaction. The model predictions are however much closer to the data than the phase space prediction (dashed line) for  $E_\gamma \geq 200$  MeV. This indicates that some form of 2N interaction may underly this channel, although the process does not appear to be as straightforward as the  $(\gamma, pn)$  case. The model predicts low  $P_m$  strength which is not visible in the data; a small but consistent effect also evident in previous comparisons [16, 19] under different kinematic conditions.

For the  $E_m=40-70$  MeV region the 2N model gives a reasonable description of the shape of the low  $P_m$  ( $\leq 300$  MeV/c) region. For higher  $P_m$  a significant excess above the 2N model prediction is evident in the data. These events populate regions roughly half way between the 2N and phase space predictions, indicating a strong contribution from FSI/multiparticle processes to the yield. The relative proportion of the excess events rises from  $\sim 15\%$  of the 2N for  $E_\gamma=200-300$  MeV to  $\sim 50\%$  of the 2N for  $E_\gamma=400-500$  MeV. This behaviour is in contrast to that of the  $(\gamma, pn)$  reaction where the observed excess was small and showed little photon energy dependence.

For the NQD kinematics (Fig 5.13) the data again illustrate the sampling of the 2N process in regions of high initial pair momenta. The more extreme kinematics show much improved separation of the data and phase space predictions indicating the measured distributions are not simply reflecting detector threshold effects.

The 2N model predictions give a better description of the shape of the data on the low  $P_m$  side of the distribution than the QD kinematics, although there is a slight tendency to underestimate the magnitude of the cross section. The tail of events observed in the corresponding  $(\gamma, pn)$  distributions for  $E_\gamma \geq \sim 300$  MeV is also present in this channel. These events only represent  $\leq \sim 4\%$  of the total (QD+NQD)  $E_m \leq 40$  MeV yield, indicating the small contribution of non-2N processes for the  $(\gamma, pp)$  reaction in this missing energy region.

For the  $E_m=40-70$  MeV region the 2N model gives a reasonable prediction of the shape of the low missing momentum ( $\leq 300$  MeV/c) data, although an excess of events above the 2N model predictions are evident in the data for higher  $P_m$ . As observed for the QD region data the relative contribution of the excess shows a strong photon energy dependence and dominates the yield for higher  $E_\gamma$ . Although the results show that most of the yield for  $E_\gamma \geq 200$  MeV cannot be described by direct 2N emission, the low  $P_m$  region is consistent with the predictions of photon absorption by  $(1s)(1p)$  pairs.

### • Recoil Theta Distributions

The recoil theta distributions for the  $(\gamma, pp)$  reaction in QD kinematics are shown in figure 5.14. The  $E_m \leq 40$  MeV data show a forward peaked distribution, similar to that observed in the  $(\gamma, pn)$  case, and show reasonable separation from the phase space model (dashed line) prediction for the higher photon energies. The data from the  $E_m=40-70$  MeV region show a more forward peaked  $\theta_{rec}$  distribution which is closer to the phase space prediction.

For  $E_m \leq 40$  MeV the 2N model predictions (solid line) give reasonable agreement with the shape of the data. The model predictions do however show a small relative shift to more backward  $\theta_{rec}$  compared with the data for  $E_\gamma=200-400$  MeV. The  $E_\gamma=400-500$  MeV data show a hint of some excess strength above the 2N

prediction for  $\theta_{rec} \sim 70^\circ$ .

In the  $E_m = 40-70$  MeV region a considerable excess strength above the predictions of the 2N model is evident in the data for  $E_\gamma \geq 200$  MeV, as observed in the corresponding  $P_m$  distributions. The similarity of the distribution of the excess events to the phase space prediction shows that the detected protons have little correlation. This characteristic might be expected due to the influence of FSI or multiparticle processes. The hint of excess strength around  $\sim 70^\circ$  is also observed in this  $E_m$  region for  $E_\gamma = 400-500$  MeV.

The measured distributions for the NQD kinematics (figure 5.15) again show a more extreme forward peaked distribution, with the data only populating regions of  $\theta_{rec} \leq 70^\circ$ . The data for all  $P_m$  are shown as the solid circles. The triangular data points show the distributions obtained after applying cuts on  $P_m$  to select regions near to the direct 2N prediction.

For  $E_m \leq 40$  MeV the shape of the data is reasonably well described by the 2N model although, as observed for the  $P_m$  comparison, the magnitude of the cross section is underestimated. The 2N model gives slightly improved agreement with the data cut on the 2N region of  $P_m$  (triangles). For  $E_\gamma = 300-400$  MeV, the tail of events observed in the  $P_m$  distribution (removed by the  $P_m$  cut) can be seen to add strength for all  $\theta_{rec}$  although with a tendency to populate more forward angles. As the data for  $E_\gamma = 400-500$  MeV have large statistical errors it is hard to draw any conclusions from the comparison in this region.

The  $E_m = 40-70$  distributions (circles) are fitted well by the model at the lowest  $E_\gamma$  range but an excess above the 2N model prediction becomes increasingly dominant as the photon energy is increased. For the higher photon energies the model does however give good agreement with the data cut on the 2N region of  $P_m$  (triangles). This gives more evidence of the existence of direct photon absorption on (1s)(1p) proton pairs in this region. The excess strength above the 2N

$^{12}\text{C}(\gamma,pp) - \text{QD KINEMATICS}$

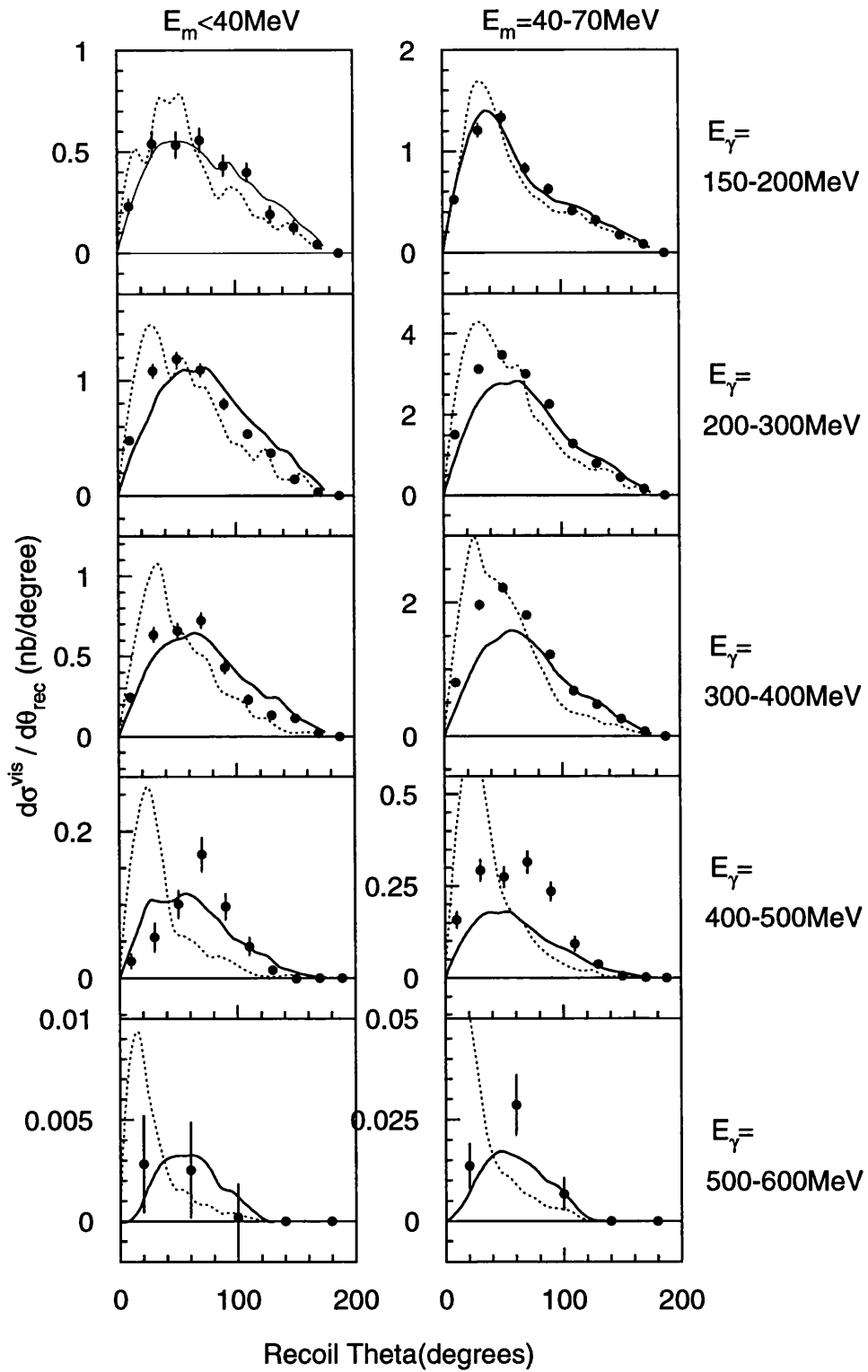


Figure 5.14:  $^{12}\text{C}(\gamma,pp) \theta_{\text{rec}}$  distributions compared with the 2N model (solid line) and phase space predictions (dashed line) for two missing energy regions in the QD kinematics.

$^{12}\text{C}(\gamma, pp) - \text{NQD KINEMATICS}$

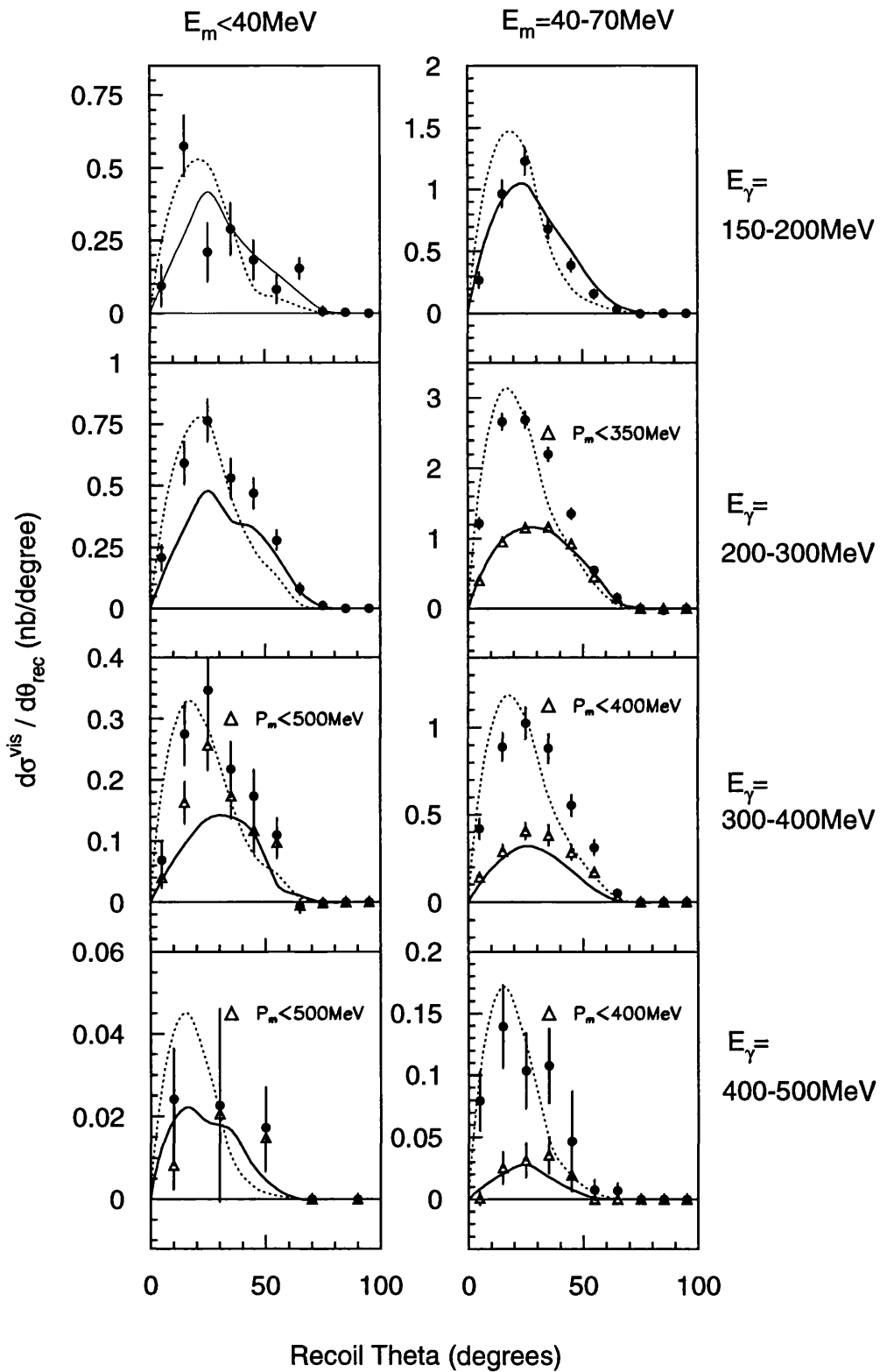


Figure 5.15:  $^{12}\text{C}(\gamma, pp) \theta_{\text{rec}}$  distributions compared with the 2N model (solid line) and phase space predictions (dashed line) for two  $E_m$  regions in the NQD kinematics. The data shown as solid circles is for all  $P_m$  while the triangular points represent the distributions obtained after selecting the 2N region of  $P_m$ .

prediction shows a distribution similar to the predicted phase space, suggesting the involvement of FSI or multiparticle processes.

## 5.4 The $(\gamma, 3N)$ reactions

The bulk of the higher missing energy component of the  $(\gamma, 2N)$  cross section for photon energies around and above the  $\Delta$  resonance is predicted to come from reactions involving 3 or more particles and therefore a measurement of the  $(\gamma, 3N)$  reactions gives a more stringent test of our understanding of such mechanisms. The wide phase space coverage obtained for this experiment is well suited to the study of these events.

To examine the level of excitation in the residual system following the emission of the 3 detected particles the 3 body missing energy is constructed, ( $E_m^{3N}$ ):

$$E_m^{3N} = E_\gamma - T_p^{PiP} - T_{N1}^{TOF} - T_{N2}^{TOF} - T_{recoil} \quad (5.4)$$

where  $T_p^{PiP}$  is the energy of the proton detected in PiP and  $T_{N1}^{TOF}$ ,  $T_{N2}^{TOF}$  are the energies of the two particles detected in the TOF array.  $T_{recoil}$  is the calculated energy passed to the recoiling system, calculated from the (measured) momenta of the photon and the 3 detected particles.

The extraction of  $(\gamma, 3N)$  data is limited by the method of charge determination, and is governed by the width of the elements in the  $\Delta E_{TOF}$  rings. Although most of the TOF bars are only fed through one  $\Delta E_{TOF}$  element some of the TOF bars lie across or near the joins of these elements and so have more than one relevant  $\Delta E_{TOF}$  element for charge determination. The angular coverage of the elements ranges from  $20^\circ - 30^\circ$  enforcing a minimum opening angle cut between the TOF side particles of  $60^\circ$  for clean identification of the ppn and ppp final charge states. For consistency this cut was applied to the data and model

predictions for all the  $(\gamma, 3N)$  reactions.

As the  $(\gamma, 3N)$  reactions have small visible cross sections the photon energy bins for the 3N analysis are broad to improve the statistical accuracy of the results. The two ranges presented cover  $E_\gamma=150-400\text{MeV}$  and  $E_\gamma=400-700\text{MeV}$ . As discussed in section 5.2, data points plotted beyond the high  $E_m$  threshold are necessarily zero and do not represent actual experimental measurements in this region.

## 5.5 Comparisons with the Valencia model

To compare the Valencia model directly with the  $(\gamma, 3N)$  data 12 MeV is subtracted from the predicted energies of each nucleon before any observables are calculated. The magnitude of the subtraction is larger than the 8 MeV employed for the 2N case, to take some account of the greater average nucleon separation energies in the  $(\gamma, 3N)$  reactions.

As for the  $(\gamma, 2N)$  the VM predictions are separated according to the initial photon absorption mechanism, with each component colour coded as described in figure 5.1.

### 5.5.1 The $(\gamma, ppn)$ reaction

The missing energy and particle kinetic energy distributions for the  $(\gamma, ppn)$  channel are shown as figures 5.16 and 5.17, corresponding to photon energy regions 150-400 MeV and 400-700 MeV respectively.

The data from the lower photon energy region possesses a significant strength near threshold ( $Q(ppn)=34\text{ MeV}$ ), indicating a considerable cross section for the three nucleons being emitted with the residual system left near its ground state. The higher  $E_m^{3N}$  strength decreases rapidly and disappears above  $\sim 250\text{MeV}$ . The

$^{12}\text{C}(\gamma,ppn) E_\gamma=150-400 \text{ MeV}$

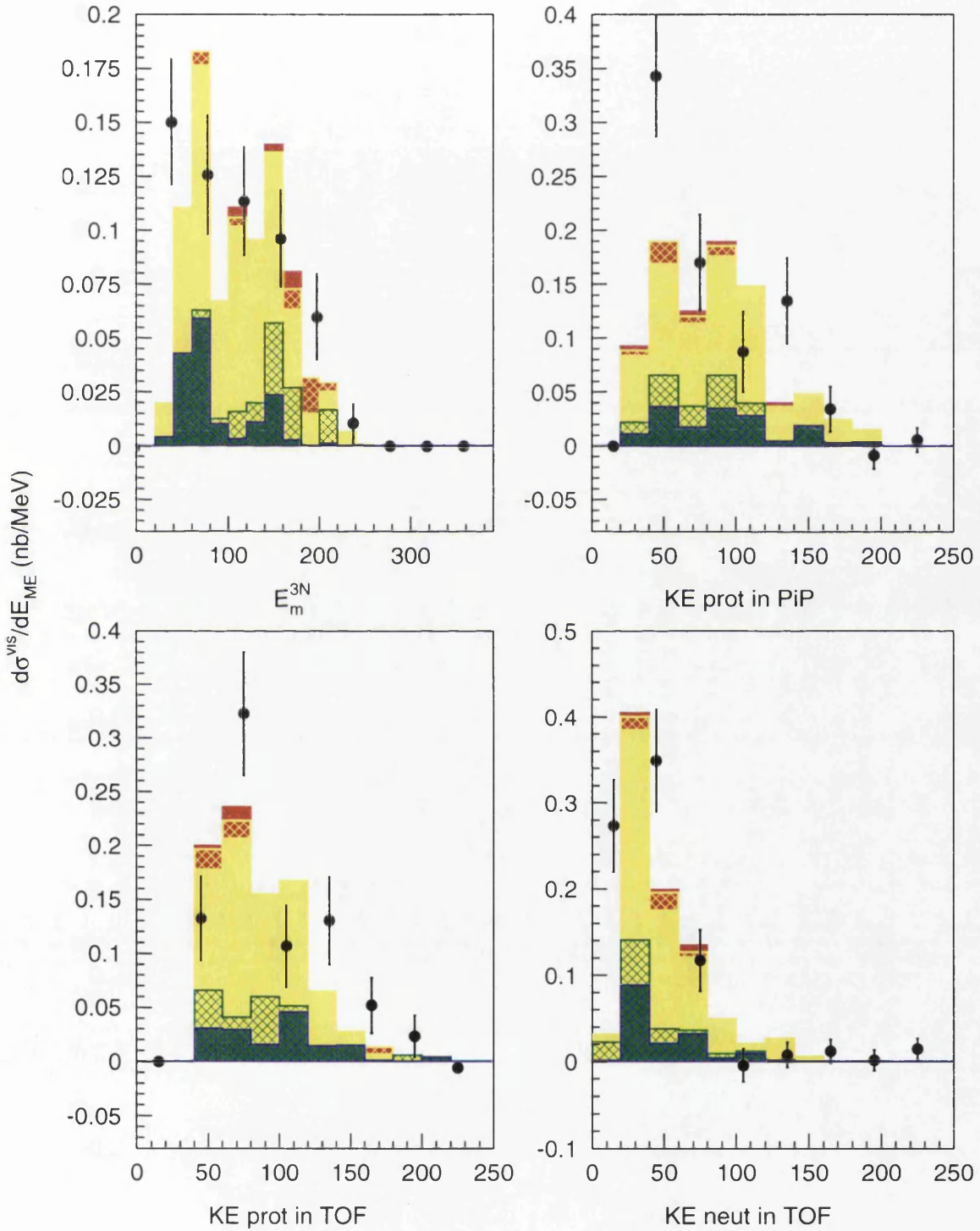


Figure 5.16:  $^{12}\text{C}(\gamma,ppn)$  missing energy (3 body) and particle energy distributions for  $E_\gamma=150-400 \text{ MeV}$  compared with the predictions of the Valencia model.

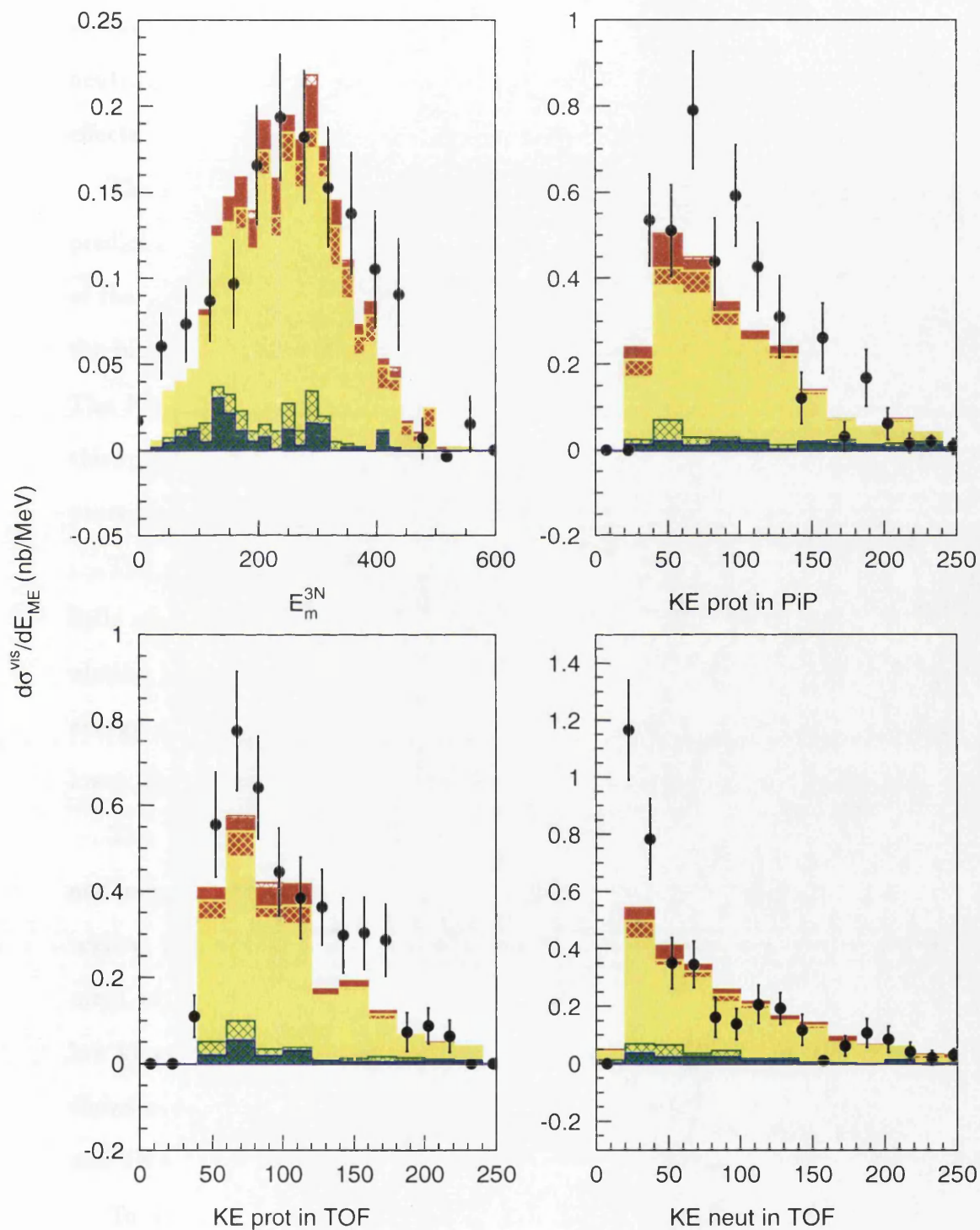
$^{12}\text{C}(\gamma, \text{ppn})$   $E_\gamma=400-700$  MeV

Figure 5.17:  $^{12}\text{C}(\gamma, \text{ppn})$  missing energy (3 body) and particle energy distributions for  $E_\gamma=400-700$  MeV compared with the predictions of the Valencia model.

particle kinetic energy distributions show a tendency for the detected protons to have higher energies than the neutron. As the upper detection threshold for neutrons is higher than protons this does not simply reflect detector threshold effects and is a definite feature of the data.

The shape and magnitude of the  $E_m^{3N}$  distribution is well described by the VM predictions within the modest statistics. The differences in the range and shape of the particle kinetic energy distributions are also well described. In particular the bias towards lower neutron energies observed in the data is well reproduced. The  $N\pi$ +ABS process is predicted to be the dominant reaction mechanism for this region although a significant contribution from the  $2N$ +FSI and  $3N_{direct}$ +FSI processes is also observed.

The data from the higher photon energy region (figure 5.17) show relatively little strength near to threshold with the bulk of the observed cross section populating higher  $E_m^{3N}$  regions. As in the lower photon energy region similar kinetic energy distributions are obtained for both detected protons with a bias towards lower kinetic energies observed in the neutron distribution.

The VM predictions give a good description of the changes in both the shape and magnitude of the  $E_m^{3N}$  cross section in going to the higher photon energy region. The predicted shape of the kinetic energy distributions are in good agreement with the proton data although the model does not reproduce the observed low kinetic energy strength for the detected neutron. The  $N\pi$ +ABS mechanism shows even more dominance for this photon energy region with the  $3N_{direct}$ +FSI and  $2N$ +FSI processes predicted to contribute little to the cross section.

To understand the origin of the  $N\pi$ +ABS process in more detail, and to allow more detailed comparison with the other  $(\gamma, 3N)$  channels, the  $N\pi$ +ABS prediction was separated according to the initial  $\pi$  production process. This is shown in table 5.1 where the relative contribution of each of the four initial pion

production processes are shown as a percentage of the total  $N\pi+ABS$  yield.

initial process	$E_\gamma=150-400\text{MeV}$	$E_\gamma=400-700\text{MeV}$
$p\pi^0$	20.0%	23.0%
$p\pi^-$	2.8%	10.2%
$n\pi^+$	45.5%	28.1%
$n\pi^0$	34.2%	38.9%

Table 5.1: *The Valencia model predictions of the initial mechanisms contributing to the  $N\pi+ABS$  process in the  $^{12}\text{C}(\gamma,ppn)$  reaction.*

The most important initial mechanism for the low photon energy region is predicted to be initial  $\pi^+$  production on a proton ( $n\pi^+$ ), which accounts for almost half the yield for the observed  $ppn$  final state. This dominance can be understood as arising from the higher probability of pion absorption on  $pn$  pairs and the lower detection threshold for neutrons (19 MeV) compared to protons ( $\sim 40$  MeV) in TOF.

The higher photon energy region shows a different characteristic with an increased proportion of initial  $p\pi^-$  production and a significant decrease in the  $n\pi^+$ . The VM has been shown to underestimate (by  $\sim 10-20\%$ ) the total  $n\pi^+$  cross section on the free proton for  $E_\gamma=350-500$  MeV [40], and so this effect may in part be due to this.

### 5.5.2 The $(\gamma,ppp)$ reaction

The missing energy and kinetic energy distributions for the  $(\gamma,ppp)$  reaction are shown as Figures 5.18 and 5.19. For this reaction the particles detected in TOF are not distinguishable and so they are separated according to angle. Proton1 is taken as the most forward angle TOF proton with proton2 the TOF proton detected at more backward angles.

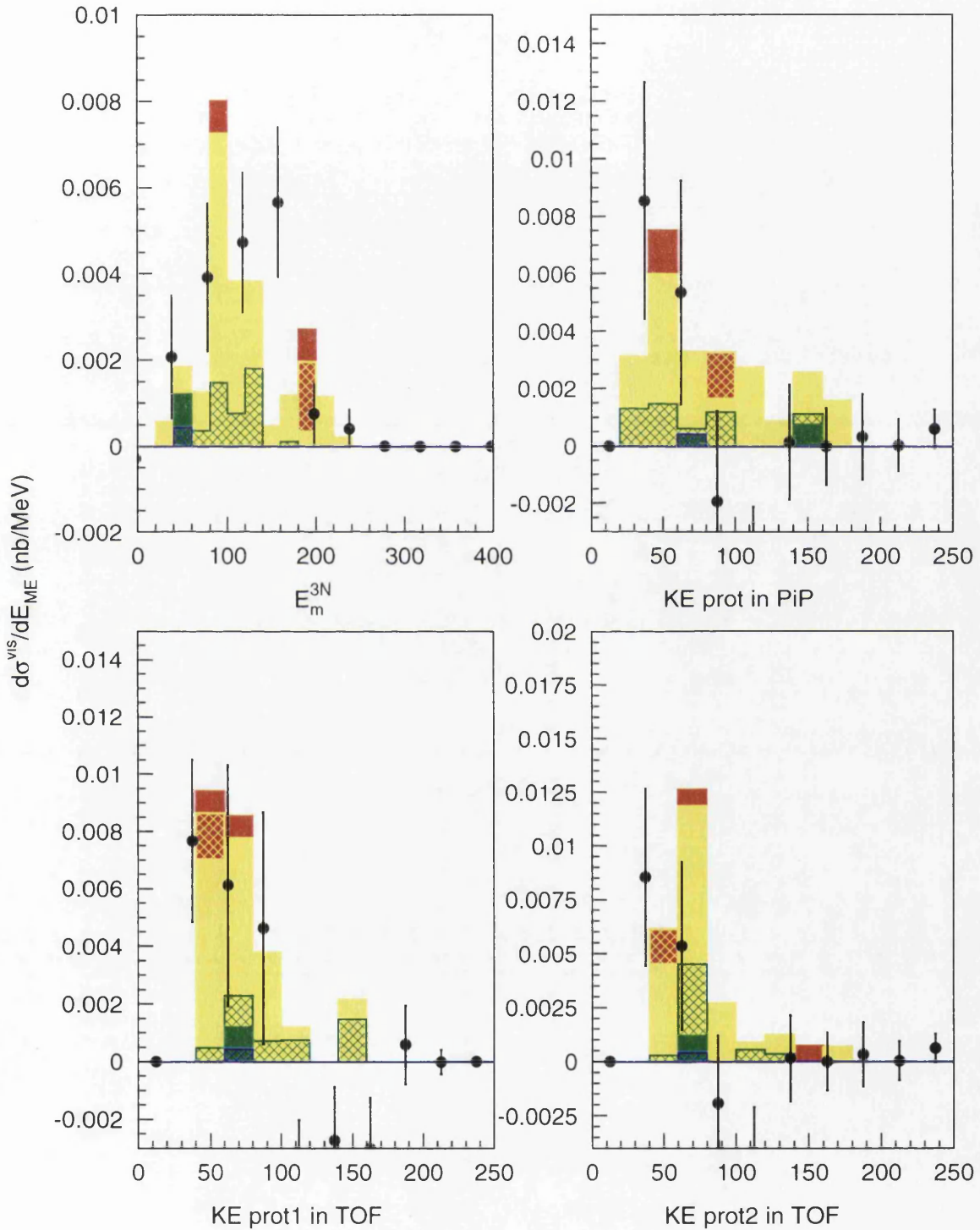
$^{12}\text{C}(\gamma, ppp) E_\gamma=150-400 \text{ MeV}$ 

Figure 5.18:  $^{12}\text{C}(\gamma, ppp)$  missing energy (3 body) and particle energy distributions for  $E_\gamma = 150-400 \text{ MeV}$  compared with the predictions of the Valencia model. The model predictions have been reduced by a factor 6.

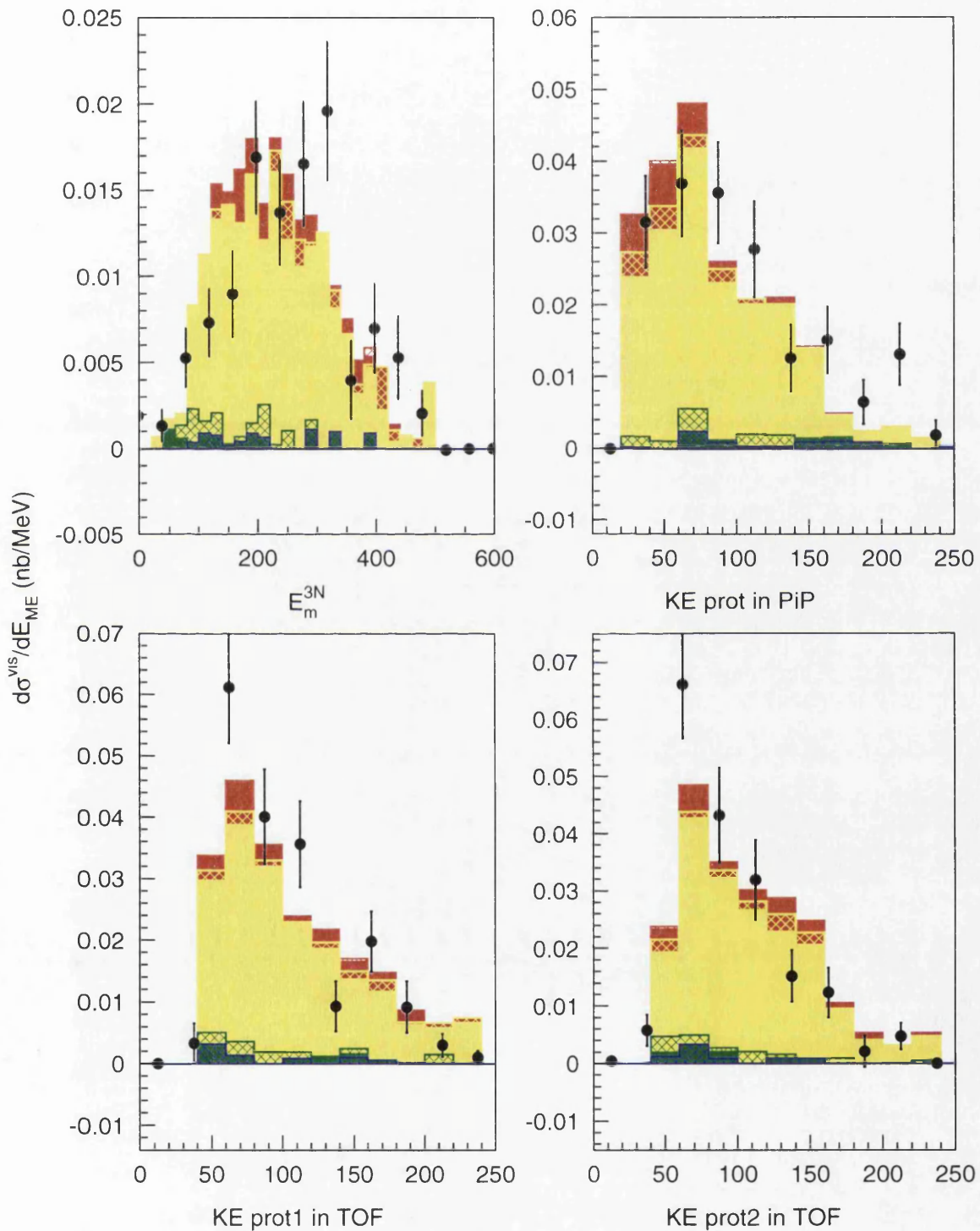
$^{12}\text{C}(\gamma, ppp) E_\gamma=400-700 \text{ MeV}$ 

Figure 5.19:  $^{12}\text{C}(\gamma, ppp)$  missing energy (3 body) and particle energy distributions for  $E_\gamma=400-700 \text{ MeV}$  compared with the predictions of the Valencia model. The model predictions have been reduced by a factor 4.

The low photon energy data (figure 5.18) has modest statistical accuracy due to the extremely low cross section for the  $(\gamma, ppp)$  reaction. The cross section obtained is seen to be  $\sim 3\%$  of the corresponding  $(\gamma, ppn)$ , although this figure will be influenced by the higher energy threshold for the detection of two protons compared to a proton and a neutron in TOF.

The VM predictions shown in the figure have been divided by a factor of 6 to match the data. A detailed interpretation of the contributions in this region is restricted due to the poor statistics, both in the data and the model. The model however can be seen to give predictions which lie in the  $E_m^{3N}$  and kinetic energy regions of the data and indicate a large  $N\pi + \text{ABS}$  contribution.

The data for the higher photon energy region allow for a more detailed interpretation of the results. The cross section in this  $E_\gamma$  range is  $\sim 8\%$  of the corresponding  $(\gamma, ppn)$ . The  $E_m^{3N}$  distribution exhibits a similar shape to that of the  $(\gamma, ppn)$  reaction although with a smaller relative contribution of low missing energy events near to the threshold ( $Q(\text{ppp})=46.8$  MeV). The particle kinetic energies for all the detected protons show similar shapes.

The predictions of the VM for this higher photon energy region have been reduced by a factor of 4 to match the data. Despite the overestimation the model predicts the shape of the  $E_m^{3N}$  and particle kinetic energy distributions well. For the higher photon energy region, as in the  $(\gamma, ppn)$  channel, the cross section is predicted to be dominated by  $N\pi + \text{ABS}$  processes with other mechanisms giving only small contributions.

The  $N\pi + \text{ABS}$  contribution to the  $(\gamma, ppp)$  channel is particularly informative as to first order (without charge exchange FSI) it can only be fed from  $\pi^0$  absorption on a pp pair, ie.

$$\gamma + p \rightarrow p + \pi^0 \quad , \quad \pi^0 + p + p \rightarrow p + p \quad (5.5)$$

A more detailed separation of the VM predictions of the  $N\pi+ABS$  process to the  $(\gamma, ppp)$  reaction is shown in table 5.2. The lower photon energy region is

initial process	$E_\gamma=150-400\text{MeV}$	$E_\gamma=400-700\text{MeV}$
$p\pi^0$	34.3%	46.8%
$p\pi^-$	9.1%	12.4%
$n\pi^+$	49.6%	30.4%
$n\pi^0$	7.0%	11.4%

Table 5.2: *The Valencia model predictions of the initial mechanisms contributing to the  $N\pi+ABS$  process in the  $^{12}\text{C}(\gamma, ppp)$  reaction.*

predicted to be predominantly fed from  $N\pi+ABS$  reactions which rely on charge exchange FSI (CEFSI) processes to produce the ppp final state with only  $\sim 1/3$  of the yield originating from the  $p\pi^0$  reaction discussed above. It should be noted that this non charge exchange FSI channel on its own is stronger than the data. However as most of the yield comes from other initial processes, either these or CEFSI processes are also too large.

The overestimation of the contribution of CEFSI processes could arise from either a simple overestimation of the strength or from an angular distribution of the scattered particles which results in too many events making the TOF opening angle cut. The second argument is supported by the previously described results for the  $(\gamma, pp)$  channel where the overestimation of the VM was found to be angular dependent, with the overestimation increasing as the TOF detected proton occurred at more backward angles.

For the higher photon energy region the  $p\pi^0$  contribution increases and accounts for roughly half the predicted yield. As the  $(\pi^0, pp)$  reaction also gives a sizeable contribution to the well predicted  $(\gamma, pppn)$  channel this indicates that the  $\pi^0$  absorption probability is reasonably well described. The VM has been shown

to give excellent agreement with the available data for the total  $\pi^0$  production cross sections on single protons for  $E_\gamma$  up to 400 MeV and to give a reasonable prediction of the angular distribution data for a photon energy of 320 MeV [40]. It seems unlikely that the VM prediction will drastically overestimate the  $p\pi^0$  process at  $E_\gamma \geq 400$  MeV while still giving a reasonable description of the dominant  $n\pi^0$  process for  $(\gamma, ppn)$ . It seems more likely that the origin of the factor of 4 discrepancy in the predicted magnitude of the cross section lies in some error in the modelling of the probability or angular distribution of the CEFSI process.

### 5.5.3 The $(\gamma, pnn)$ reaction

The missing energy and kinetic energy distributions for the  $(\gamma, pnn)$  reaction are shown as Figures 5.20 and 5.21. For the low photon energy the magnitude of the cross section can be seen to be comparable with that observed for the  $(\gamma, ppn)$  channel. The kinetic energy distributions illustrate a tendency for the forward angle TOF neutrons to possess larger energies than those detected at more backward angles.

The VM predictions give a reasonable description of the magnitude of the  $E_m^{3N}$  distribution within the statistics of the data. The asymmetry in the TOF neutron kinetic energy spectra is not however well produced by the model with both neutrons predicted to have similar distributions.

For the higher photon energy region the  $E_m^{3N}$  distribution is again reminiscent of that of the corresponding  $(\gamma, ppn)$ , exhibiting little strength near threshold with most of the cross section at higher missing energies. The neutron kinetic energy spectra show similar shapes for both the forward and backward angles, in contrast to the asymmetry observed for the lower  $E_\gamma$  region.

The VM predictions give a good description of both the shape and magnitude of the data in this region although the predicted low energy enhancement of the

backward neutron energy spectrum is not seen in the data.

The  $N\pi+ABS$  contributions, for both  $E_\gamma$  regions, are separated according to the initial photon interaction in table 5.3. In the lower photon energy region

initial process	$E_\gamma=150-400\text{MeV}$	$E_\gamma=400-700\text{MeV}$
$p\pi^0$	18.4%	20.7%
$p\pi^-$	18.5%	25.6%
$n\pi^+$	20.0%	11.7%
$n\pi^0$	43.2%	42.0%

Table 5.3: *The Valencia model predictions of the initial mechanisms contributing to the  $N\pi+ABS$  process in the  $^{12}\text{C}(\gamma, pnn)$  reaction.*

much of the predicted yield originates from initial  $n\pi^0$  production. This can be understood due to the higher probability of  $\pi$  absorption on pn pairs. The lower probability for events from the  $p\pi^-$  reaction, which can also produce a pnn final state after absorption on a pn pair, can be understood to result from the PiP detector threshold. As this is higher than the TOF neutron threshold fewer of the low energy protons from the  $p\pi^0$  process will be detected.

For the higher photon energy region a similar dominance is observed for events originating from initial  $n\pi^0$  production as for lower  $E_\gamma$ . The influence of the  $p\pi^-$  process is seen to increase and this may be due to more energy being available for the detected proton.

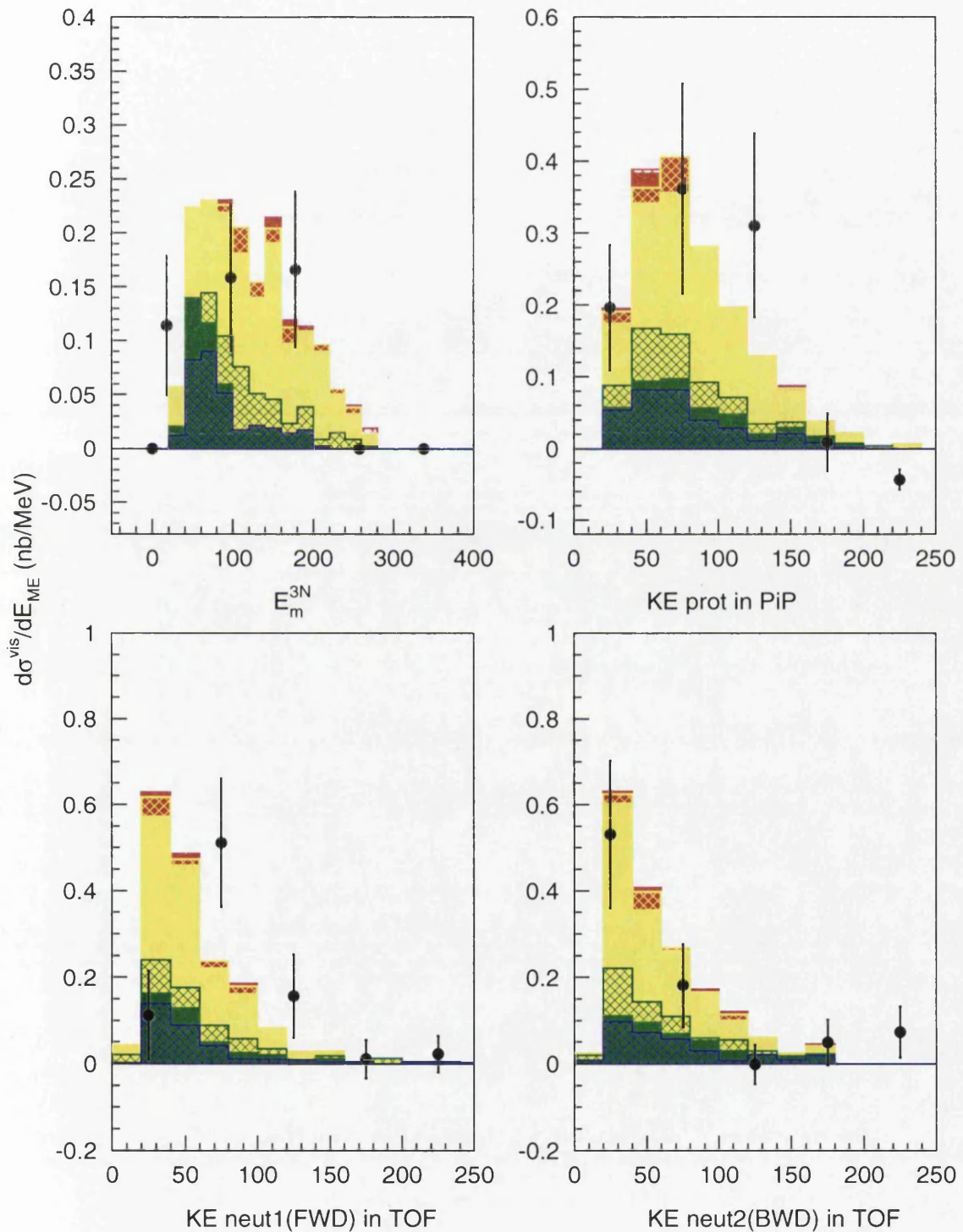
$^{12}\text{C}(\gamma, \text{pnn})$   $E_\gamma=150\text{-}400$  MeV

Figure 5.20:  $^{12}\text{C}(\gamma, \text{pnn})$  missing energy (3 body) and particle energy distributions for  $E_\gamma=150\text{-}400$  MeV compared with the predictions of the Valencia model.

$^{12}\text{C}(\gamma, pnn) E_\gamma=400-700 \text{ MeV}$

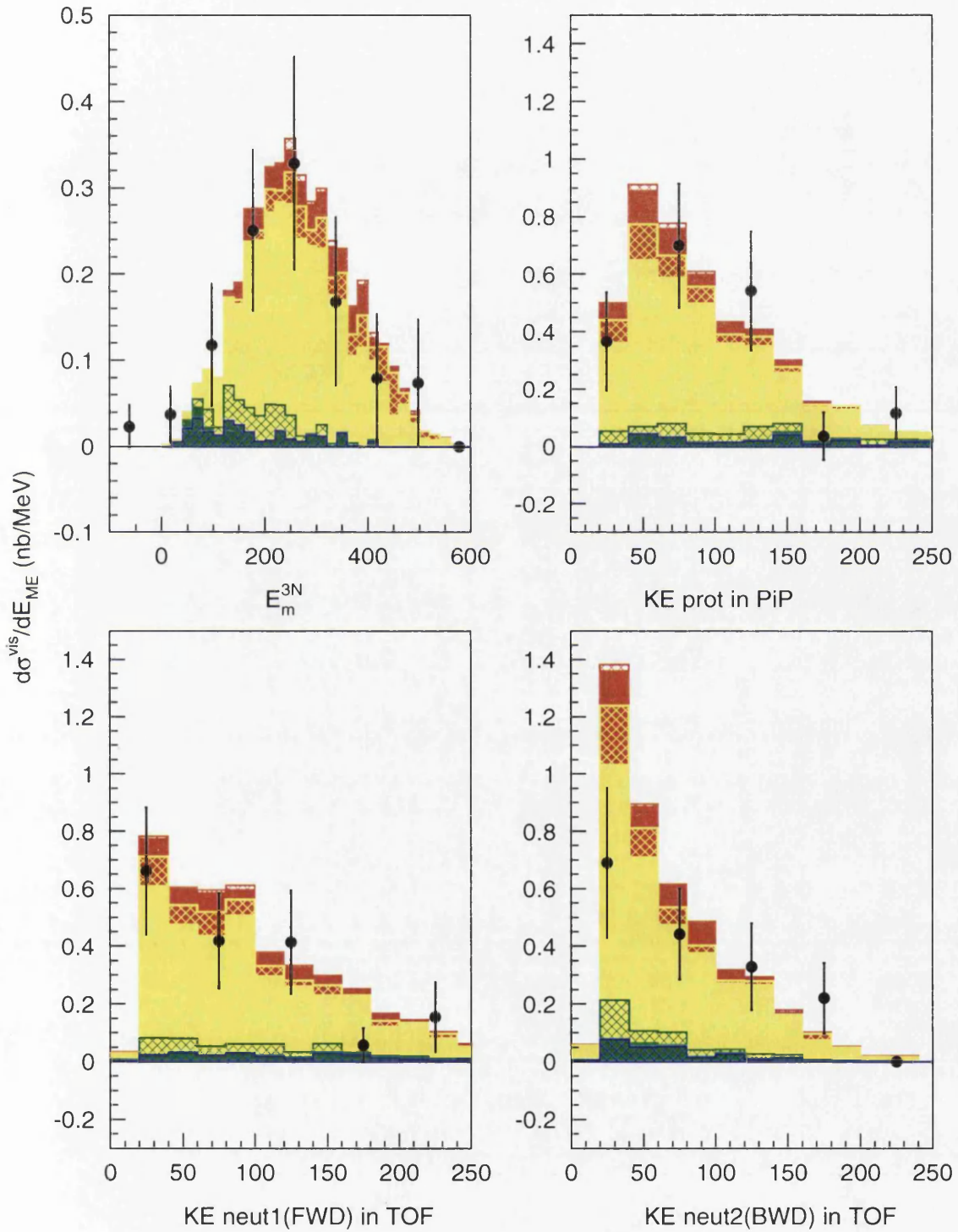


Figure 5.21:  $^{12}\text{C}(\gamma, pnn)$  missing energy (3 body) and particle energy distributions for  $E_\gamma=400-700 \text{ MeV}$  compared with the predictions of the Valencia model.

## **Chapter 6**

# **Summary, Conclusions and Outlook**

## 6.1 Summary and Conclusions

This thesis described a study of both the  $^{12}\text{C}(\gamma, 2N)$  and  $^{12}\text{C}(\gamma, 3N)$  reactions for  $E_\gamma=150\text{-}700$  MeV with a detector acceptance which included regions away from the usual back-to-back kinematics. This work extended both the 2N opening angle coverage and the photon energy range of previous experiments. The  $^{12}\text{C}(\gamma, 2N)$  reaction was measured for pn and pp final charge states. The  $^{12}\text{C}(\gamma, 3N)$  reaction was measured for ppn, ppp and pnn final charge states.

The  $^{12}\text{C}(\gamma, 2N)$  data was separated into two regions of phase space. The first region (QD) corresponded to TOF polar angles near to that of two body kinematics ( $\theta_{\text{TOF}}=36.7^\circ\text{-}71^\circ$ ). The second region (NQD) for  $\theta_{\text{TOF}}=78.0^\circ\text{-}142.0^\circ$ , covered more extreme kinematics not studied in detail in any previous measurements.

The results were compared with a model developed by the Valencia group, which accounts for all the main photon absorption processes and gives predictions of the cross section in all missing energy ( $E_m$ ) regions. Separate comparisons with the data for each kinematic region allowed the contributing processes for both 2N kinematics (QD) and the more unusual NQD kinematics to be compared, providing a more detailed test of the model than previously available.

The  $^{12}\text{C}(\gamma, pn)$   $E_m$  distributions were reasonably well reproduced by the VM, which predicts the general shape of the data in both kinematic regions for all photon energies. Some overestimation of the cross section strength was however observed in both the QD and NQD kinematics for photon energies around the  $\Delta$  resonance. The agreement with the VM was not as good as for previous measurements of this reaction, taken with different detector geometries, implying that the angular distributions of some of the processes in the VM contributing to the pn final state may not be accurate. The VM predictions for the  $^{12}\text{C}(\gamma, pp)$  reaction in QD kinematics, although giving a reasonable description of the shape of the

$E_m$  distributions, overestimated the data by a factor of  $\sim 3.5$ . This factor did not provide agreement for all photon energy bins indicating an energy dependence in the overestimation. Applying the same scaling factor to the VM predictions in the NQD region resulted in an overestimation of the data, implying the correction factor for the pp channel is both angular and energy dependent.

The VM does not permit a detailed comparison with the direct 2 nucleon emission process at low  $E_m$ . This is due to the nuclear matter approximation employed in the model which neglects the shell structure of the real nucleus. To study the low  $E_m$  regions in more detail the data were compared to a 2N model which predicted the distributions of kinematic variables assuming direct 2N emission from a spectating residual nucleus. The model does not predict the low  $E_m$  cross section magnitude although a direct prediction of the relative yield in the NQD kinematics was made by normalising the model to the QD data and then employing this normalisation for both regions. The low  $E_m$  data were separated into two missing energy regions corresponding to that expected from photon absorption on  $(1p)^2$  nucleon pairs ( $E_m \leq 40$  MeV) and  $(1s)(1p)$  pairs ( $E_m = 40-70$  MeV)

For the  $^{12}\text{C}(\gamma, pn)$  reaction comparisons of the measured missing momentum ( $P_m$ ) and recoil theta ( $\theta_{rec}$ ) distributions with the 2N model confirmed that for  $E_m \leq 40$  MeV the direct emission of  $(1p)^2$  pairs is the dominant process, even in the NQD kinematics. FSI/multiparticle processes were shown to constitute  $\leq 3\%$  of the total (QD+NQD) observed yield in this region. For  $E_m = 40-70$  MeV the data from the QD kinematics were well described by direct emission of  $(1s)(1p)$  pairs. The NQD data showed a larger influence from non-2N events although these constituted  $\leq \sim 10\%$  of the combined (QD+NQD)  $E_m = 40-70$  MeV yield and  $\leq \sim 5\%$  of the combined  $E_m \leq 70$  MeV yield.

The results therefore show the dominance of direct 2N emission in the  $^{12}\text{C}(\gamma, pn)$

reaction for  $E_m \leq 70$  MeV and photon energies up to 600 MeV, even in the case where the detectors were positioned to be sensitive to more complex mechanisms. This indicates the previously observed 2N dominance was not simply due to the positioning of the detectors in earlier measurements. This work also extends the findings of previous measurements by giving the first evidence for the existence of direct emission of proton-neutron pairs at  $E_\gamma \geq 400$  MeV and shows the feasibility of studying the 2N mechanism in  $(\gamma, pn)$  reactions up to photon energies well beyond the  $\Delta$  resonance.

The  $^{12}\text{C}(\gamma, pp)$  reaction, for  $E_\gamma=150-500$  MeV, was shown to be reasonably well described by absorption on a  $(1p)^2$  proton pair for  $E_m \leq 40$  MeV. The agreement between the data and model was however not as good as the  $^{12}\text{C}(\gamma, pn)$  case, indicating the mechanism for this reaction may not be as straightforward. FSI/multiparticle processes were again shown to give a small contribution in this  $E_m$  region, comprising ( $\leq 4\%$ ) of the observed (QD+NQD) yield. Evidence for absorption on  $(1s)(1p)$  pairs was found in the  $E_m=40-70$  MeV data for photon energies up to 500 MeV. The contribution of FSI/multiparticle processes in this region was however seen to be considerable for photon energies around and above the  $\Delta$  resonance. Little yield was observed for photon energies above 500 MeV due to the more restrictive upper particle detection thresholds for this reaction.

The first measurement of the  $^{12}\text{C}(\gamma, ppn)$  and  $^{12}\text{C}(\gamma, pnn)$  reactions, along with that of  $^{12}\text{C}(\gamma, ppp)$ , provides valuable information on multiparticle photon absorption mechanisms. For  $E_\gamma=150-400$  MeV the ppn and pnn final states were seen to have cross sections of comparable magnitude and to show significant strength in the 3 body missing energy ( $E_m^{3N}$ ) distributions near to threshold. The cross section for the ppp final state was found to be  $\sim 3\%$  of the ppn or pnn, with little strength near to threshold. For the higher photon energy bin of  $E_\gamma=400-700$  MeV much of the observed cross section was found to be at high  $E_m^{3N}$ , with all

the measured final charge states showing a similar shape. The ppn and pnn data were also of comparable magnitude for these higher photon energies. The ppp yield was again seen to be smaller, constituting  $\sim 8\%$  of the ppn or pnn.

The VM gave good descriptions of the shape of the  $E_m^{3N}$  distributions for all the measured final states. The dominant mechanism for all reactions was predicted to be the reabsorption of photoproduced pions by nucleon pairs ( $N\pi$ +ABS), with lesser contributions from  $2N/3N_{direct}$ +FSI processes. The predicted magnitude of the cross section is in good agreement for the ppn and pnn reactions. The ppp cross section was however overestimated by a factor of 4–6. Further investigation of the VM predictions for the dominant  $N\pi$ +ABS contribution showed that 50–75% of ppp yield comes from charge exchange FSI (CEFSI) processes. The well predicted ppn and pnn reactions have smaller contributions from CEFSI and so the ppp overestimation was taken as an indication of errors in the calculation of the magnitude and/or angular distribution of the CEFSI processes. It was however noted that even without contributions involving CEFSI processes the predicted ppp cross section magnitude was larger than the data in both  $E_\gamma$  regions, indicating an overestimation of the non charge exchange FSI contribution as well.

## 6.2 Outlook

The evidence for dominant direct  $2N$  photon absorption mechanisms (with small FSI/multiparticle contributions) for the  $^{12}\text{C}(\gamma, pn)$  reactions up to 700 MeV shows the possibility for more detailed studies of the effect of short range MEC and  $\Delta$  contributions to the 2-body current in the pn pair for photon energies through and beyond the  $\Delta$  resonance. Theoretical calculations [21] for low photon energies have shown the need for detailed measurements of the angular distribution

to extract meaningful information. Particularly interesting are the mechanisms above 500 MeV which extend beyond the  $\Delta$  resonance and may proceed via interesting new mechanisms, perhaps involving the higher nucleon resonances. The higher photon energies may also be expected to show more sensitivity to SRC between the pn pair as they probe shorter distances. Extracting an angular distribution for 2N processes from the present measurement would be limited as the detectors were placed to predominantly sample kinematics outwith that of 2N and therefore the analysis would be limited both in angular range and statistical accuracy.

Direct 2N emission processes in the  $(\gamma, pp)$  channel have also been shown to be open to detailed study. The present  $(\gamma, pp)$  data were restricted at high photon energies due the upper detector thresholds for detecting and identifying a proton in TOF. Furthering our understanding of this channel for high  $E_\gamma$  would require detectors which did not suffer from this problem and would allow the interesting low  $E_m$  region to be extracted where the corresponding proton energies are large.

The  $(\gamma, 3N)$  measurements presented in this work were exploratory in nature. The detector solid angle coverage, although larger than previous measurements, was much less than  $4\pi$  sr and thus the measured yields were small and somewhat biased to 'in-plane' kinematics. A detector system with more complete phase space coverage would be necessary to make more definite conclusions about the total cross sections for multiparticle/FSI processes. One possibility is refurbishing the large solid angle LADS detector [68] or at higher  $E_\gamma$  using the CLAS detector [69] at TJNAF.

As only nucleon final states were measured in this work little information was extracted from the important multiparticle mechanisms involving the emission of pions. An interesting extension of this work could be the measurement of the  $(\gamma, NN\pi)$  final state which may give information on N- $\Delta$  interactions in the

nuclear medium.

# **Appendix A**

## **Corrections For Dead Top Bars**

Four of the TOF bars used in the experiment were faulty and so are removed from the analysis completely. This causes different complications according to whether the dead bar is in a front or back layer and whether the particle is charged or uncharged. The corrections for each event type are discussed below.

- **Charged particles**

If the dead TOF bar is in a back layer the observed yield will be unaffected as the energy of the particle can still be obtained using information from the hit in the front layer.

If the dead bar is in a front layer then a true proton event can either stop in the front layer or continue on to fire one of the bars immediately behind. A solitary hit in the back layer would be discarded by the proton tracking procedure and so would not be included in the yield. Thus a simple correction factor equal to the ratio of live to dead bars in the front layers can be applied to the observed yield.

- **Uncharged particles**

A dead bar in the back layer will simply reduce the yield by a factor equal to the ratio of live to dead bars in the two layers.

If the dead bar is in the front layer then the previous correction factor will be too high as scattered protons from the dead bar cannot be identified, causing them to be included in the yield. The amount of scattering is estimated by looking at the yield in a (nearby) back layer bar with and without the proton tracking procedure imposed. The correction factor ( $f$ ) for a bank of 16 bars with one front layer bar missing is then given by:

$$f = \frac{16}{15 + \delta x/x} \quad (\text{A.1})$$

where  $x + \delta x$  is the number of hits with no proton tracking and  $x$  is the number with the tracking in place.

The correction factors obtained for each TOF stand are shown in table A.1.

TOF STAND	Uncharged	Charged
G	1.0512	1.1483
H	1.0512	—
I	1.1056	1.3333
J	1.1056	—
K	1.0666	—
L	1.0666	—

Table A.1: *Correction factors for dead TOF bars.*

# Bibliography

- [1] L. Lapikas, Nucl. Phys. A553 (1993) 297c.
- [2] M.Q. Barton and J.H. Smith, Phys. Rev. 95 (1954) 573.
- [3] A. Stadler *et al.*, Phys. Rev. C51 (1993) 2896.
- [4] N. Bianchi *et al.*, Phys. Rev. C54 (1996) 1688.
- [5] G. Piller and W. Weise, Phys. Rev. C42 (1990) 1834
- [6] M.Q. Barton and J.H. Smith, Phys. Rev. 110 (1958) 1143.
- [7] J. Garvey *et al.*, Nucl. Phys. 70 (1965) 241.
- [8] I.L. Smith, J. Garvey, J.G. Rutherglen and G.R. Brookes, Nucl. Phys. B1  
(1967) 483.
- [9] P.C. Stein *et al.*, Phys. Rev. 119 (1960) 348.
- [10] J. Arends *et al.*, Z. Phys. A298 (1980) 103.  
J. Arends *et al.*, Z. Phys. A305 (1982) 205.  
J. Arends *et al.*, Nucl. Phys. A526 (1991) 479.
- [11] S. Homma *et al.*, Phys. Rev. Lett. 45 (1980) 706.  
S. Homma *et al.*, Phys. Rev. Lett. 52 (1984) 2026.  
S. Homma *et al.*, Phys. Rev. Lett. 53 (1984) 2536.  
S. Homma *et al.*, Phys. Rev. C 27 (1983) 31.

- [12] M. Kanazawa *et al.*, Phys. Rev. C 35 (1987) 1828.
- [13] K. Baba *et al.*, Nucl. Phys. A415 (1984) 462.
- [14] S.N. Dancer *et al.*, Phys. Rev. Lett. 61 (1988) 1170.
- [15] I.J.D. MacGregor *et al.*, Nucl. Phys. A533 (1991) 269.
- [16] J.C. McGeorge *et al.*, Phys. Rev. C 51 (1995) 1967.
- [17] S.M. Doran *et al.*, Nucl. Phys. A559 (1993) 347.
- [18] S. Klein, Universität Tübingen Ph.D. Thesis (1990).
- [19] P.D. Harty *et al.*, Phys. Lett. B 380 (1996) 247.
- [20] T.H. Yau, University of Glasgow Ph.D. Thesis (1996); T.H. Yau *et al.*, submitted to Z.Phys; I.J.D. MacGregor *et al.*, submitted to Phys. Rev. Lett.;
- [21] M. Vanderhaeghen, L. Machenil, J. Ryckebusch and M. Waroquier, Nucl. Phys. A580 (1994) 551.
- [22] L. Machenil, M. Vanderhaeghen, J. Ryckebusch and M. Waroquier, Phys. Lett. B 316 (1993) 17.
- [23] G. Backenstoss *et al.*, Phys. Rev. Lett. 55 (1985) 2782.; R. Tacik *et al.*, Phys. Rev. C 40 (1989) 256.; D. Mack *et al.*, Nucl. Phys. A527 (1991) 451c.; R.D. Ransome *et al.*, Phys. Rev. C 45 (1992) 509.;
- [24] J.M. Laget, J. Phys. G14 (1988) 1445.
- [25] G. Audit, Phys. Lett. B 227 (1989) 331.
- [26] A.J Sarty *et al.*, Phys. Rev. C 47 (1993) 459.
- [27] T. Emura *et al.*, Phys. Rev. Lett. 73 vol. 3 (1994) 404.

- [28] G. Audit *et al.*, Nucl. Phys. A614 (1997) 461.
- [29] P.D Harty *et al.*, submitted to Phys. Rev. C
- [30] S. Boffi *et al.*, Nucl. Phys. A546 (1993) 473.
- [31] J.S. Levinger *et al.*, Phys. Rev. 84 (1951) 43.
- [32] K. Gottfried, Nucl. Phys. 5 (1958) 557.
- [33] L. Boato and M.M. Giannini, J.Phys.G 15 (1989) 1605.
- [34] S. Boffi and M.M. Giannini, Nucl. Phys. A533 (1991) 441.
- [35] C. Giusti, F.D. Pacati and M. Radici, Nucl. Phys. A546 (1992) 607.
- [36] J. Ryckebusch, L. Machenil, M. Vanderhaeghen, and M. Waroquier, Phys. Lett. B 291 (1992) 213.
- [37] H. de Vries, C. W. de Jager and C. de Vries, Nucl. Data Tables 36 (1987) 495.
- [38] J.M. Laget, Nucl. Phys. A497 (1989) 391.
- [39] A.E. Thorlacius and H. W. Fearing, Phys. Rev. C33 (1986) 1830.
- [40] R.C. Carrasco and E. Oset *et al.*, Nucl. Phys. A536 (1992) 445.; R.C. Carrasco and E. Oset, Nucl. Phys. A570 (1994) 701.
- [41] C. Mahaux, P.F. Bortignon, R.A. Broglia, C.H. Dasso, Phys. Reports. 120 (1985) 1.; P. Fernandez de Cordoba, E. Oset, Phys. Rev. C46 (1992) 1697.
- [42] E. Oset, Y. Futami and H. Toki, Nucl. Phys. A448 (1986) 597.; L.L. Salcedo, E. Oset, M.J. Vicente-Vacas, C. Garcia-Recio, Nucl. Phys. A484 (1988) 557.
- [43] A.Braghieri *et al.*, Phys. Lett. B 363 (1995) 46.

- [44] I. Anthony *et al.*, Nucl. Inst. and Meth. A301 (1991) 230.
- [45] S.J. Hall, G.J. Miller, R. Beck and P. Jennewein, Nucl. Inst. and Meth. A368 (1996) 698.
- [46] S.J. Hall and G.J. Miller, Kelvin Lab Annual Report 1990, pp 35-38.
- [47] I.J.D. MacGregor *et al.*, Nucl. Inst. and Meth. A382 (1996) 470-489
- [48] J.R.M. Annand *et al.*, Nucl. Inst. and Meth. A368 (1996) 385-391
- [49] W. Braunschweig *et al.*, Nucl. Inst. and Meth. 134 (1976) 261.
- [50] G.V. O'Rielly, N.R. Kolb and R.E. Pywell, Nucl. Inst. and Meth. A368 (1996) 745.
- [51] Scintillation materials, NE Technology Catalogue.
- [52] R. Madey, Phys. Rev. 85 (1952) 410.
- [53] G.E. Cross, University of Glasgow, Ph.D. thesis (1994).
- [54] Scintillation materials, NE Technology Catalogue.
- [55] G. Miller. Private Communication.
- [56] T.H. Yau, University of Glasgow, Ph.D. thesis (1996).
- [57] S. McAllister, University of Glasgow, Ph.D. thesis.
- [58] T. Hehl. *et al.*, Nucl. Inst. and Meth. A354 (1995) 505.
- [59] T. Hehl. Private Communication.
- [60] R. Schneider. Private Communication.
- [61] S. Franczuk. Private Communication.

- [62] T. Lamparter. Private Communication.
- [63] R.A. Cecil, B.D. Anderson and R. Madey, Nucl. Inst. and Meth. 161 (1979) 439.
- [64] T. Lamparter *et al.*, Z. Phys. A355 (1996) 1.
- [65] G.E. Cross *et al.*, Nucl. Phys. A593 (1995) 463.
- [66] E.D. Hackett *et al.*, Phys. Rev. C53 (1996) R1047.
- [67] M.J. Vicente Vacas and E. Oset. Nucl. Phys. A568 (1994) 855.
- [68] T. Altholz *et al.* Nucl. Inst. and Meth. A373 (1996) 374. A. Lehmann *et al.*, Phys. Rev. C55 (1997) 2931.
- [69] V.D. Burkert and B.A. Mecking, *Future Detectors for Photonuclear Experiments*, Edinburgh (1991) 225.

